Optical properties of noble metal nanocluster hybrids and their potential for biosensing

Sanader Maršić, Željka

Doctoral thesis / Disertacija

2016

UNIVERSITY OF SPLIT

dabar

DIGITALNI AKADEMSKI ARHIVI I REPOZITORIJI

University of Split
Faculty of Science
Biophysics Doctoral Programme

Željka Sanader

Optical properties of noble metal nanocluster hybrids and their potential for biosensing

Doctoral thesis

Split, 2016

Sveučilište u Splitu
Prirodoslovno-matematički fakultet
Poslijediplomski sveučilišni doktorski studij
Biofizika

Željka Sanader

Optička svojstva nanoklastera plemenitih metala unutar hibridnih sustava i njihova primjena u biosenzorici

Doktorski rad

Split, 2016.

Sveučilište u Splitu, Prirodoslovno-matematički fakultet

Odjel za fiziku, Poslijediplomski sveučilišni doktorski studij Biofizika

"Optička svojstva nanoklastera plemenitih metala unutar hibridnih sustava i njihova primjena u biosenzorici"

Doktorski rad autorice Željke Sanader kao dio obaveza potrebnih da se dobije doktorat znanosti, izrađen pod vodstvom mentora: prof. dr. dr. h. c. Vlasta Bonačić-Koutecký i prof. dr. sc. Paško Županović

Dobiveni akademski naziv i stupanj: doktorica prirodnih znanosti iz polja fizika

Povjerenstvo za ocjenu i obranu doktorskog rada u sastavu:

1. prof. dr. sc. Ante Bilušić, redoviti profesor
2. prof. dr. sc. Franjo Sokolić, redoviti profesor
3. dr. sc. Anita Kriško, viši znanstveni suradnik
4. dr. sc. Mile Ivanda, znanstveni savjetnik (zamjenski član)

1. _____

2. _____

3. _____

Potvrđuje da je disertacija obranjena dana _____

Voditelj studija: prof. dr. sc. Paško Županović

_____

Predsjednik Vijeća studija: prof. dr. dr. h. c. Vlasta Bonačić-Koutecký

_____

BASIC DOCUMENTATION CARD

University of Split
Faculty of Science   Ph.D. thesis

OPTICAL PROPERTIES OF NOBLE METAL NANOCLUSTER HYBRIDS AND THEIR POTENTIAL FOR BIOSENSING

Željka Sanader

Thesis performed at

- University of Split, Faculty of Science
- Center of excellence for science and technology-Integration of Mediterranean region (STIM) at Interdisciplinary center for Advanced science and technology (ICAST), University of Split
- Institut Lumière Matière, UMR CNRS 5306 and Université Claude Bernard Lyon 1, Université de Lyon, France

Abstract:

Linear and nonlinear optical properties of functionalized forms of noble metal nanoclusters are addressed in this thesis. Noble metal nanoclusters belong to nonscalable regime in which each atom counts. They exhibit molecular like electronic transitions, due to quantum confinement effects, which are strongly influenced by structure. These systems have potential for applications in biosensing and bioimaging, based on their unique optical, electronic and structural properties, after being stabilized either by formation of hybrid systems of metal nanoclusters and biomolecules or protecting nanoclusters by ligands. Using density functional theory and its time dependent version interplay between electronic and structural properties in hybrid nanocluster-biomolecules and ligated clusters has been investigated in order to gain insight into origins of their unique optical properties. To understand optical properties of hybrid systems, silver cluster- histidine complexes, as well as nonlinear properties of ligated silver nanoclusters have been investigated theoretically, and compared with experimental results obtained by expert international collaborators. Within this thesis the concept has been worked out allowing to design systems with large two-photon cross sections which can serve for efficient imaging of tissues and cells.

(84 pages, 19 figures, 1 table, 115 references, 2 appendices, original in English)

TEMELJNA DOKUMENTACIJSKA KARTICA

OPTIČKA SVOJSTVA NANOKLASTERA PLEMENTIH METALA UNUTAR HIBRIDNIH SUSTAVA I NJIHOVA PRIMJENA U BIOSENZORICI

Željka Sanader

Rad je izrađen u:

- Prirodoslovno-matematičkom fakultetu, Sveučilište u Splitu, Hrvatska
- Centru izvrsnosti za znanost i tehnologiju-Integracija Mediteranske regije (STIM) pri Interdiscipliarnom centru za naprednu znanost i tehnologiju (ICAST), Sveučilište u Splitu
- Institutu Lumière Matière, UMR CNRS 5306 i Sveučilištu Claude Bernard Lyon 1, Sveučilište u Lyonu, Francuska

Sažetak:

U ovoj tezi su opisana linearna i nelinearna optička svojstva funkcioniziranih oblika nanoklastera plemenitih metala. Nanoklasteri plemenitih metala pripadaju neskalirajućim sustavima u kojima se svaki atom broji. Zbog efekata kvantnog zatočenja, imaju elektronske prijelaze slične onima u molekulama, na koje jako utječe struktura. Zbog svojih jedinstvenih optičkih, elektronskih i strukturnih svojstava, potencijalni su kandidati za primjene u biosenzorici i biooslikavanju, nakon što se stabiliziraju formiranjem hibridnih sustava s biomolekulama ili ih se zaštiti ligandima. U tezi je istraživan je odnos elektronskih i strukturnih svojstava u hibridnim sustavima biomolekula i metalnih klastera kao i u ligandiranim klasterima kako bi se razumio uzrok njihovih jedinstvenih optički svojstava, koristeći teoriju funkcionala gustoće i njenu vremenski ovisnu varijantu. Da bi se razumjela svojstva hibridnih sustava, teorijski su istraživani hibridni sustavi srebrenih klastera i histidina te nelinearna svojstva ligandiranih srebrnih klastera, i uspoređeni s eksperimentalnim rezultatima koje su napravili međunarodni suradnici. Razvijen je koncept koji bi mogao pomoći dizajniranju sustava s jakom dvo-fotonskom apsorpcijom koji bi služili za oslikavanje tkiva i stanica.

ACKNOWLEDGEMENT

ABSTRACT

The focus of present thesis are linear and nonlinear optical properties of functionalized forms of noble metal nanoclusters (NC). In contrast to nanoparticles larger than 5 nm, noble metal nanoclusters belong to nonscalable regime in which each atom counts. Therefore, they exhibit molecular like electronic transitions, due to quantum confinement effects. Based on their unique optical, electronic and structural properties, these systems have potential for applications in biosensing and bioimaging, after being stabilized. The required stabilization can be achieved following two strategies: (i) by formation of hybrid systems of metal NCs and biomolecules; and (ii) protecting nanoclusters by ligands.

In recent decade gold clusters received lots of attention, because of their simple synthesis and fluorescence properties. But, in spite of more difficult synthesis of silver clusters which has been achieved in last decade, silver cluster have advantages due to localized intense excitations and strong absorption and emission at given wavelengths which offers large potential for bioapplications. Their unique properties inspired research presented in this thesis.

Using density functional theory and its time dependent version interplay between electronic and structural properties in hybrid NCs-biomolecules and ligated clusters has been investigated in order to gain insight into origins of their unique optical properties. At the same time, complementary experimental investigations based on mass spectroscopy technique and linear and nonlinear optics allowed to confirm theoretical results and to develop strategy to propose new materials with optimal optical properties.

In attempt to propose new materials for for biosensing with improved sensitivity, first, linear optical properties of hybrid systems of silver nanoclusters and biomolecules have been explored in this thesis. Influence of protons and noble metal cations on optical response of 2,4-dinitrophenylhydrazine (DNPH) has been determined to allow tuning of optical response of structures with aromatic rings through interaction with silver cluster subunit. Since DNPH is attaches to carbonylated proteins it is of a special interest for identifying carbonylation sights of protein in context of biological aging.

Although, it has been already shown that small silver clusters enhance absorption of peptides, origin of this important property that improves sensitivity of detection of peptides needs additional clarification. Therefore, optical properties of cationic and anionic silver cluster- histidine hybrids have been investigated in this thesis to examine the role of the metal-biomolecular interface and its influence on properties of hybrid systems. Understanding of nature of electronic excitations responsible for the absorption and emission allows to design new class of materials for biosensing. Other type of stabilized functionalized nanoclusters are liganded clusters where different ligands are bound to silver atoms forming protecting shell around nanocluster that prevents nanoclusters from aggregation and uncontrolled interaction with environment. Different ligands can be used, but most common ones due to preparative convenience are those containing thiol groups which form strong sulfur-silver bonds. These systems have remarkable linear and nonlinear optical properties, which are considerably better than those of organic dyes, which are presently used for bioimaging. Different sizes ligated nanoclusters are explored both theoretically and experimentally to determine influence of size, including size and the structure of the core, excitation wavelength and class of ligand type on two-photon absorption spectra. Numerous advantages of nonlinear optics include their localized excitation which eliminates photobleaching and photodamage and deeper tissue penetration. Within this thesis the concept has been worked out allowing to design systems with large two-photon cross sections which can serve for efficient imaging of tissues and cells.

PUBLICATIONS

The following publications constitute the main part of the thesis:

1. Ž. Sanader, C. Brunet, M. Broyer, R. Antoine, Ph. Dugourd, R. Mitric, V. Bonačić-Koutecký, "Cation induced electrochromism in 2,4-dinitrophenylhydrazine (DNPH): Tuning optical properties of aromatic rings", *Chemical Physics Letters*, **2013**, 570, 22

2. Ž. Sanader, R. Mitrić, V. Bonačić-Koutecký, B. Bellina, R. Antoine, Ph. Dugourd, "The nature of electronic excitations at the metal–bioorganic interface illustrated on histidine–silver hybrids", *Phys. Chem. Chem. Phys.*, **2014**, 16, 1257

3. I. Russier-Antoine, F. Bertorelle, R. Hamouda, D. Rayane, Ph. Dugourd, Ž. Sanader, V. Bonačić-Koutecký, P.F. Brevet, R. Antoine, "Tuning Ag_{29} nanocluster light emission from red to blue with one and two-photon excitation" , *Nanoscale*, **2016**, 8, 2892

4. Ž. Sanader, M. Krstić, I. Russier-Antoine, F. Bertorelle, Ph. Dugourd, P. F. Brevet, R. Antoine, V. Bonačić-Koutecký, "Two-photon absorption of ligand-protected Ag_{15} nanoclusters. Towards a new class of nonlinear optics nanomaterials", *Physical Chemistry Chemical Physics*, **2016**, 18, 12404

5. I. Russier-Antoine, F. Bertorelle, Ž. Sanader, M. Krstić, C. Comby-Zerbino, Ph. Dugourd, P. F. Brevet, V. Bonačić-Koutecký, R. Antoine, "Ligand-Core NLO-phores: a combined experimental and theoretical approach of the two-photon absorption and two-photon excited emission properties of small ligated silver nanoclusters", *Nanoscale*, **2016**, Submitted

The following publications are included in the appendix:

1. B. Bellina, R. Antoine, M. Broyer, L. Gell, Ž. Sanader, R. Mitrić, V. Bonačić-Koutecký, Ph. Dugourd, "Formation and characterization of thioglycolic acid-silver cluster complexes", *Dalton Trans.*, **2013**, 42, 8328

2. M. Girod, Ž. Sanader, M. Vojković, R. Antoine, L. MacAleese, J. Lemoine, V. Bonačić-Koutecký, Ph. Dugourd, "UV Photo-dissociation of proline-containing peptide ions: Insights from molecular dynamics", *J Am Soc Mass Spectrom.*, **2015**, 26, 432

Contents

INTRODUCTION

1   General concept

Physical and chemical properties of small metallic nanoclusters (NC) with discrete energy levels change dramatically with their size, thus they are within the nonscalable regime in which each atom counts. In contrast, large metallic nanoparticles (NP) (from 10 to 100 nm) where confinement plays role, belong to scalable regime. Both classes of nanoparticles exhibit interesting, but significantly different optical properties. Large NP have delocalized electrons confined within their size, which upon excitation by resonant light exhibits collective oscillations of electrons. This phenomenon is called surface plasmon resonance effect, and for noble metal nanoparticles this resonant frequency has the visible light wavelengths, so these systems show bright colors. In contrast, interaction of light with nanoclusters characterized by molecular like discrete energy levels gives rise to individual transitions between electronic states at given wavelength and intensity, as observed in absorption spectra. Due to spectroscopic interference effects, usually, these systems with delocalized electrons have only few intense transitions and many weak ones. Owning to their unique optical properties including absorption and emission, which can strongly influence biomolecular environment, NC and NP have been recognized as valuable probes in sensing and bioimaging. NP consisting of metals like silver, gold and copper have one relatively wide absorption band in visible region, while NC offer great opportunities for tuning because of their localized, discrete transitions which can be designed at desired wavelengths. This vast potential for tunability, and numerous possibilities in bioapplication motivated research presented in this thesis.

Sensing includes a variety of procedures which use different probes to measure presence or concentration of targeted compound by translating a biochemical interaction between the probe and desired molecule into a quantifiable physical signal. NC can be used as fluorescent probes in sensing application because of their influence on biomolecular environment, such as enhancing absorption and emission intensities of biomolecules. There are reported three classes of sensors: (i) cluster sensors of which the fluorescence quenches in the presence of the analyte; (ii) sensor in which fluorescent clusters are formed only in presence of the analyte; and (iii) sensors that experience shift of the absorption and fluorescence wavelengths depending on their chemical environment.

Bioimaging relates to methods that visualize biological processes, while interfering as little as possible. For these studies, fluorescence-based optical microscopy is the most common method because it is a minimally invasive technique even over extended periods of time; it is exceedingly sensitive and with great image resolution. The key advantage of fluorescence microscopy is identification of particular functional processes by specifically attaching fluorophores to molecule of interest.

So far conventional fluorescent probes include organic dyes and quantum dots which have been widely used in biosensing and imaging. However, their limitations in imaging of dynamic processes on longer time scale, photodestruction of the fluorophore (photobleaching), photodynamic damage to the specimen mediated by the fluorophore (photodamage), photoblinking, problems with autofluorescence from biological tissues which hide wanted fluorescence signal, as well as concern due to toxicity (for quantum dots) have stimulated search for new fluorescent probes. NCs are proving to be excellent candidates for this purpose, their advantages include unique optical properties, such as strong absorption and emission at the given wavelengths, ultrasmall size, large Stokes shift, good photostability. In addition, hybrid systems of NCs biomolecules or ligands retain excellent optical properties and have additional benefits such as stability, low cytotoxicity and good biocompatibility.

On the other hand, NP have demonstrated their potential for biosensing using the surface enhanced Raman spectroscopy (SERS) technique. Materials that reflect light nevertheless absorb small portion of it, which causes their atoms to vibrate and reflected light has different wavelength from the incident light. This phenomenon is the Raman scattering process, and using the vibration of the atoms as its fingerprints it is possible to determine the chemical composition of the material. In comparison to Raman spectroscopy, SERS additionally requires the presence of metal nanostructures as an integral component that enhances Raman's otherwise weak signal. Enhancement factors are strong enough to allow even single molecule detection, making this technique comparable to fluorescence. Molecules adsorbed on metal NP surface interact with electromagnetic field of surface plasmon in NP which leads to enhancement. Typical metals used are gold or silver.

Within this thesis the unique linear and nonlinear optical proprieties of noble metal NC have been functionalized through interactions with biomolecules or ligands in context of possible applications such as biosensing and bioimaging. Two routes have been followed. I. Biomolecules such as amino acids or proteins usually do not exhibit intense absorption transitions although their subunits contain aromatic rings with delocalized electrons in analogy to delocalized metallic electrons in noble metal NCs. Therefore, the concept that attachment of small metal NCs to such biomolecules will enhance their absorption intensity due to mutual interaction of subunits by formation of hybrid systems has been proposed. II. In the case of ligated clusters the role of ligands has been to stabilized nanoclusters and by formation of metallic core to take advantage of its unique optical properties in analogy to bare clusters.

In the Introduction brief overview of current insights in NCs will be given, as well as short summary of main part of this theses, described in details in Chapters 2 - 6. First, structural characteristics of noble metal NCs will be presented, as well as their functionalized forms: cluster-biomolecule hybrid systems and liganded clusters. NCs can have numerous applications exploiting their different properties, from catalysis, cancer therapy, drug delivery to bioapplications. In this theses will be presented optical properties of NCs and their functionalized forms for sensing and imaging bioapplications. Further, density functional theory as well as its time dependent form used for describing these properties will be summarized. At the end of this Introduction, new scientific contributions of this theses will be outlined.

2 Production and characterization of noble metal NC and their hybrids

Metal nanoclusters typically consist from several to few hundreds of atoms, belonging to the size regime smaller than 2 nm in which "each atom counts", since the structural and electronic properties change with size. In the gas phase, they are produced by warming bulk metals till their melting point, when atoms from bulk metal start to evaporate and produce clusters of three or more atoms[1].

Knowing the geometric structure of nanoclusters is important for understanding their optical, electronic and catalytic properties and for this purpose various experimental techniques are used. Mass spectrometry (MS) is method of choice for experimental characterization of size selected gas phase clusters. This technique ionizes specimens so they can be manipulated by electric and magnetic field, accelerates them till they all have the same kinetic energy and sorts the ions by deflection. Different ions are deflected by the magnetic field by different amounts depending on the mass of the ion (lighter ions are deflected more than heavier ones) and the charge on the ion (ions with more charges are deflected more than ones with less charge). As ionization of NCs can lead to fragmentation, electrospray ionization mass spectrometry (ESI-MS)[2] is usually used as it is "soft ionization" technique since it causes just little fragmentation. MS gives information about the masses within a sample, but it does not say anything about the structure. Another usual characterization method is UV-Vis spectroscopy[3]. Absorption spectra of larger noble metal nanoparticles exhibit plasmon resonance bands centered at around 420nm for silver and at 520nm for gold NP. In contrast to them, small NCs exhibit molecular-like optical transitions which are highly sensitive to size and structure which allows the use of UV-Vis spectroscopy for characterization purposes.

Theoretical calculations can complement this information by investigating the structural arrangement of atoms within the clusters (and their hybrids). Using theoretical methods in gas phase the geometries of Ag_n (n = 2-8) neutral, anionic and cationic clusters were optimized to determine the lowest energy isomers for each cluster size, determining that way planar or three-dimensional structures [4][5]. Stable structures of pure Au clusters have also been theoretically explored and known since the beginning of 2000s. Small bare Au clusters form smaller number of bonds and tend to remain planar, in contrast to the structures of Ag clusters which have a larger coordination and tend to become three-dimensional for smaller sizes[6].

Due to their instability and high reactivity, nanoclusters tend to aggregate to form large nanoparticles, so their stabilization is necessary for application, and can be achieved either by ligands, support or matrices. As a result of these different interactions, properties of NC can be changed either to a small or dramatic amount. Nonmetallic subunits such as biomolecules or ligands can have different roles in nanocluster technology. For instance, biomolecules such as amino acids, proteins or DNA form cluster-biomolecule hybrid systems in which mutual interactions can give rise to novel properties that combine both NC and biomolecule properties. Also, there are ligands, molecules containing mainly thiol groups that bind to metal atoms, and form surface of ligated NC that protects nanoclusters from aggregation and build NCs interface with its surrounding.

Organic molecules are quite useful as templates for synthesis of metallic NC. Some of them are used to facilitate synthesis of metal nanoclusters, such as dendrimers, which serve

as templates for NC growth. There are two main paths to nanocluster synthesis: "bottom-up" and "top-down". In former, small building block of zerovalent metal atoms are used to form nanoclusters. In "top-down" approach metal core of large nanoparticle is etched by excessive ligands, allowing synthesis of specific size liganded metal nanoclusters[7][8][9][10]. Great challenge for synthesis presents control over reaction conditions (like temperature, pH value, concentration of reactants) because changing only one can lead to new type of NCs. At the same time this presents great advantage because it promises numerous new NCs with novel properties for new applications. Besides these wet chemistry procedures, gas phase synthesis was developed by combining laser ablation of metals[11] and electrospray ionization methods[12]. The idea is to synthesize ligated or bare metal clusters without stabilization by solution or support. Laser is used to evaporate metal atoms from surface, while different ligands can be electrosprayed to form ligated nanocluters in gas phase[13]. Another method to obtain ligated nanocluters is by electrospraying a metal salt solution. Mass spectrometer is used to characterize obtained species.

One way of functionalization of NCs is binding them to biomolecules, which was introduced by Bonačić-Koutecký group[14][15]. In cluster-biomolecule hybrid systems, biomolecules adjust their structure to new binding arrangement with cluster[16][17]. The resulting conformational changes can affect function of the biomolecule and can reduce its biological activity. So control over this changes can limit influence of the cluster on the biomolecule, thus conserving the functionality after binding and opening new possibilities for applications. In this framework, the gas phase approach offers possibility to experimentally and theoretically study models of well-defined systems without interactions with solvent or substrate and it provides a description of hybrid nanomaterials at the atomic level. On a simple silver cluster-tripeptide $Trp(Ala)_2$ model it was shown that an interaction of the metal cluster can lower mobility of the peptide at the interaction site and also verified influence of silver cluster on absorption of peptides[15], which will be described in detail in Section 3.

For several decades, solid inorganic scaffolds were utilized for stabilization of nanoclusters, such as cryogenic noble gas matrices[18][19], zeolites[20], then another way to protect nanocluster was pioneered in 2002, with synthesis of few silver atoms nanocluster encapsulated in poly(amidoamine) dendrimer hosts[21]. This was a beginning of liganded clusters protected with organic scaffolds and it opened a new route for silver nanocluster application as fluorophore. Liganded NCs usually have metallic atoms in center, while biomolecules are bound to their surface which prevents random binding of NCs to molecules in their vicinity. Since then, numerous organic ligands have been used, such as dendrimers, DNA, proteins, polymers... Dendrimers are tree-like molecules with numerous -OH groups and small cavities in which metal ions bind and form nanoclusters with well defined size, but structure is not well known because these clusters are not stable without dendrimer[22][23]. DNA oligonucleotides are used as templates mostly for silver nanoclusters, so far, rarely for gold. It was shown that different DNA-sequences influence formation of silver nanoclusters[24], where cytosine has higher affinity for silver then other nucleic bases[25]. Another class of liganded clusters are those protected by biomolecules containing sulfur, where ligands form so called "staple" motifs in form sulfur-metal atom-sulfur. Fourier transform infrared (FT-IR)[26] spectroscopy can be used to study bonding of ligands and noble metal atoms over sulfur because binding of sulfur to noble metal atom causes disappearance of vibrational mode of S-H bond which is present in ligands without metal atoms. Size (number of sulfur and metal atoms) in "staple" motifs can vary, as well as presence and number of metal atoms in core.

Structures where core is not present have the same number of sulfur and metal atoms and consist only of mutually connected "staple" motifs. Different biomolecules containing sulfur can be used, most common ones are proteins which offer huge variety of binding sites (such as sulfur in amino acid cysteine), like bovine serum albumin[27], lysozime[28], transferin[29] and many others.

In the early stages of liganded nanocluster syntheses, limitation of synthetic techniques prevented precise liganded NC isolation and structural characterization, but further development of technique revealed that specific number of metal atoms formed more stable liganded NC than other. In attempt to explain this, much attention was given to so called "magic number" superatom nanoclusters complexes. This theory was developed in 1980s in an effort to understand and to anticipate stability and properties of bare metal atom NC. These superatoms were NCs with specific number of metal atoms that behaved like one giant atom, so their stability was explained by a closed electronic shell such as those in noble gases[1][30]. This theory was generalized to include stability of liganded metal NC[31]. Those are structures that have just the right number of valence electrons that behave as free electrons and they fulfill and form closed superatomic orbitals. To calculate correct number of valence electrons in liganded clusters one has to take into account number of metal atoms in core, number of ligands (they can withdraw electrons from the metal core or localize electrons into covalent bonds) and overall charge of the liganded NC. This theory explained well stability of some liganded NC (mostly approximately spherical NC), but it also proposed restricted number of stable clusters with closed superatomic electron shells. But, experimental studies have shown stability of some liganded NC[32] that do not follow superatom theory.

Additional reasons for their stability and shapes deviating from superatom one have yet to be determined. Specific number of atoms and electrons are required for formation of different geometrical shapes such as cubic, tetrahedral or octahedral form. This illustrates the importance of knowing the composition and three dimensional structures of ligated NCs, since the interplay of structural and electronic properties will determine their characteristic optical features. Therefore, it is important to know atomic arrangement within the core as well as binding patterns of ligands in order to understand their role in hybrid systems.

Theoretical determination of structural properties of the hybrid systems of the given size is of crucial importance in particulary in the context of the lack of precise synthesis, which sometimes results in mixture of different sizes of ligated NCs that have to be separated[33]. For example, polyacrylamide gel electrophoresis (PAGE) can be used to separate mixture of nanoclusters with different size distribution which was accomplished for both glutathione protected gold[34] and silver[35] clusters. Finally, the optical properties of ligated clusters obtained from experiment can be compared with theoretical results achieved for the given size and structure allowing to assign the structural properties to experimental findings as well. In this way the design of the ligated clusters with the desired optical properties can be made.

Ligand protected gold NCs are more stable than silver ones, so they are explored much more, and crystal structure has been known for $Au_{102}(pMBA)_{44}$[36], $Au_{25}(SG)_{18}$ [37], since late 2000s. $Au_{102}(pMBA)_{44}$ (pMBA = para-mercaptobenzoic acid) has 79 Au atoms in core in D_{5h} symmetry, surrounded by 44 ligands[36], while $Au_{25}(SG)_{18}$ (SG = glutathione) has 13 atom icosahedra core, and ligands in "staple" motifs formed of sulfur-gold-sulfur-gold-sulfur bonds[37]. In general, formation of these "staple" motifs is not yet clear. In the mean time, more precise synthesis technique has been developed which enabled *one-pot-*

for-one-size synthesis[8] of liganded NCs which eliminated the need for size separation and crystal structures of additional liganded gold clusters have been determined: $Au_{20}(SR)_{16}$ [38], $Au_{24}(SR)_{20}$[39], $Au_{28}(SR)_{20}$[40], $Au_{36}(SG)_{24}$ [41].

In contrast, protected silver clusters are not as stable, their identification by mass spectrometry, or crystallographic methods is still rare, one example being $Ag_{44}(SR)_{30}$ (SR = fluorinated arylthiols)[42], which has Ag_{12} icosahedral core, protected by ligands motifs different from those in Au NCs. It is difficult to experimentally prepare size selected silver nanoclusters. Different groups produced and characterized by similar absorption spectra, but assigned to different sizes: $Ag_{31}(SG)_{19}$[32], $Ag_{35}(SG)_{18}$[43], $Ag_{32}(SG)_{19}$[44]. Another difficulty in characterization are multiple steps needed for their synthesis that can induce changes to structure[42]. Also, structural changes accumulate in time, specially in solution phase where stability of glutathione protected silver clusters was investigated. In general, smaller protected clusters with larger energy gap between the HOMO (highest occupied molecular orbital) and LUMO (lowest unoccupied molecular orbital) are more stable, and larger clusters in time produce the most stable smaller clusters, through interparticle collisions. Presence of Ag^+ ions in solution adds to stability, while pH influences charge state of ligand by ionization of functional groups which leads to different stability at different pH values[45].

Therefore, theoretical studies are valuable source of information that can help to elucidate their structural-electronic property relation. Questions that need to be answered include prediction of stable structures, determination of factors that influence stability, as well as upper size limit of NCs with discrete energy levels. To address these issues, and to compare calculated and measured spectra, further development of theoretical methods is needed, which could calculate optical properties of large clusters, and include full ligand structure, in contrast to so far used simplifications. One direction could be projector augmented wave method which can calculate large structures, but has some accuracy issues[46].

3   Linear optical properties

The first step in interaction of light with matter is absorption of photons that can induce excitation of electrons for the appropriate wavelength. Some of the absorbed energy is lost due to structural changes in excited states and possible interactions with molecular environment. Thus the molecule returns to the ground state by emitting a photon with less energy than it was absorbed, thus giving rise to fluorescence. The emitted photon has longer wavelengths (lower energy), and this is called the Stokes shift. Fluorescence of metal (Au, Ag and Cu) nanoclusters has been recognized as one of their the most important properties, and has been explored both theoretically and experimentally[47].

3.1   Characteristic optical features of NCs and their hybrids

The molecular like discrete electronic states are responsible for unique optical properties of noble metal NC, such as intense transitions in visible or near-infrared spectral region. Position and intensity of these transitions is directly connected with the structure of the cluster. Therefore, adding or removing just one atom can significantly influence their structural and thus optical response. This strong dependence on the cluster size is due to the interplay between structure and electronic properties. For example, increasing size of noble metals

nanoclusters excitation and emission bands are red shifted[22]. Until now, most studies have involved Au and Ag nanoclusters. Because of their different electronic structure, these two noble metal clusters exhibit very different optical properties. Due to the large s–d energy gap in silver atoms, these clusters exhibit only few, intense transitions due to excitation of s electrons in visible region. In contrast, in the case of gold clusters, the relativistic effects responsible for the small s–d gap give rise to excitations of d electrons as well. This leads to optical transitions of similar intensities spread over a large energy interval[48][49].

It was shown that in hybrid systems of biomolecules like amino acids and NCs, metallic NCs influence the optical properties of biomolecules. Mostly, peptides have weak absorption in visible region, but when linked to noble metal NCs biomolecules exhibit enhanced absorption in visible part of spectrum. Interplay of π electrons in aromatic rings and NCs leads to intense electronic transitions, which enables detection of linked biomolecule. Also, study of hybrid systems of NC and biomolecules in gas phase showed that the absorption patterns of bare noble metal clusters can be seen in hybrid systems. For instance, mostly s-electrons within silver subunit are excited and responsible for the localization of enhanced absorption in hybrid systems with amino-acids, while systems with gold NC show lots of low intense transitions[49]. Hybrid systems of amino acid tryptophan with different silver clusters demonstrate these features. Its characteristics include: influence of cluster size on the location of intense transitions; fingerprints of leading transitions of the cluster absorption in absorption of hybrid systems and occurrence of charge transfer between Trp and Ag_n^+ subunits because of resonance between excitations within them[50].

In the case of systems involving small nanoclusters protected by ligands, interplay between cluster core, ligands and possibly solution influences crucially their structural, electronic and therefore optical properties[22][51]. Once the metallic core of these ligated NCs is protected by biomolecule, their optical properties are not strongly influenced by their surrounding. On the other hand, class of protecting ligand influences the stability and optical properties such as absorption and florescence. Using ligands with large electron donating properties increases fluorescence intensity[52]. In another study, it was established that changes in the chemical environment, such as molar ratio of Ag and methacrylic acid or solvent, change the absorption and emission properties of ligated clusters with Ag_2, Ag_3 and Ag_5 silver atoms in core. In mentioned study, shifting of absorption was not related to a change in nanocluster size[53]. In addition to tuning the properties, ligands can induce novel ones, such as chirality. An achiral Au_{25} cluster was protected with a chiral ligand (R/S)-2-amino-3-phenylpropane-1-thiol, which introduced chirality[54].

3.2 Theoretical concepts and experimental verifications

Nanoclusters with few atoms are highly attractive for bioapplications due to their low toxicity due to small size, together with remarkable attribute of enhancing absorption and florescence properties of biomolecule such as peptide. On the other hand, nanoclusters are highly reactive, so studies in the gas phase prove basic concept of enhancing fluorescence but have to be stabilized (on appropriate surface) or protected (by suitable ligand) to be able to offer real application.

One possible application could be metallic clusters at support. The silver clusters at surface might have two folded role: to trap biomolecules (proteins) and to form ordered ensamble and at the same time their strong enhancement of absorption and fluorescence of

biomolecules is suitable for detection.

Gas phase study for silver tripeptide Trp-(Ala)$_2$ hybrid systems demonstrates that binding of positively charged Ag$_3^+$ and Ag$_9^+$ to oxygen and indole ring of tryptophan leads to intense absorption at around 300nm, which originates mainly from excitation within silver subunit. This means that silver clusters influence optical properties of pure tripeptide by enhancing it and shifting to near ultraviolet wavelengths[55]. This gas-phase investigation of structural and optical properties of silver cluster–peptide hybrid systems showed that biomolecules do not serve only as synthesis promoters, but metal silver nanoclusters considerably extend and enhance optical absorption of pure peptides [15][50][55][56]. Theoretical modeling of the optical properties allows the fundamental understanding of the metal-biomolecular interface and its influence on optical properties of hybrids. Usually, organic dyes (organic molecules that show extrinsic fluorescence) that can specifically label biomolecules have been used for detection[57][58]. But, this attractive property of hybrid systems can be interesting for the label-free detection by metallic nanoparticles and can replace dyes and increase the sensitivity of detection, which could improve early diagnostics in health care.

Silver nanoclusters of well-defined sizes can also be formed on surfaces of zeolite cages. Zeolites are crystalline, with the Angstrom size pores that control size of silver clusters. These silver nanoclusters show photostability upon excitations with UV light, which makes them biocompatible labels[59].

Another possibility for biomedical application is the use of liganded NC. Clusters protected by thiolate ligands represent an alternative route for bioapplications, since their surface functionalization by different ligands and tunable optical properties can be used for sensing in living cells[48]. Typical structure of the liganded NC consists of a metal core and an organic ligand shell. Prerequisite to using NC in biological systems is their minimal influence on studied systems, and it is defined by biocompatibility and ability of body to clear them from the system. Biocompatibility is achieved using several atoms of gold and silver to form clusters that are relatively non toxic and stable so they will not fragment, and using ligands like proteins and peptides that ensure solubility of NCs in biological specimens. Especially good candidates for stabilization of nanoclusters are ligands that contain thiol groups (e.g. proteins containing amino acid cysteine), due to strong bonding between sulfur and silver or gold atoms. To avoid long term deposition of nanoclusters inside the biological system it is necessary that they are easily cleared from the system, meaning that they have to be smaller than 5.5 nm which is approximate size limit for filtration by kidney, and they have to be soluble in water which is improved by presence of both positive and negative charges on the surface of liganded NCs [60].

By careful designing (using theoretical models) of the metal core and selecting specific ligand new liganded NCs can be developed for desired biomedical application. For instance, during the synthesis, the different sizes of the metal core, which dominantly determine linear optical properties of the NCs, can be acquired by adjusting different parameters such as the ligand-to-metal ratio, the strength of the reducing agent, reaction temperature, solvent conditions, and reaction time[8][61][62][63]. Similarly, the ligand shell can be varied by using different types of organic ligands that differ in size, surface charge, functional groups (e.g., biomolecules, polymers, and dendrimers). The NCs interacts with its surrounding through it ligand shell, so its targeted binding molecule, as well as biocompatibility, position in cell are directly dependent on the character of shell.

Optical properties of the ligand protected NCs, might be used as optical probes for determining presence of chemicals like heavy metal ions (e.g., Hg^{2+}, Cu^{2+}, Pb^{2+}) and biomolecules (e.g., proteins, nucleic acid, glucose...). Two main strategies to detect presence of targeted substrate are quenching or enhancing of fluorescence. Both silver and gold liganded NC were used for detection of, for instance, Hg^{2+} by luminescence quenching of red-emitting Au NCs protected by bovine serum albumin[64], or oligonucleotide-stabilized Ag NCs[65]. Based on the high stability and strong luminescence of the BSA-protected Au NCs, and the excellent limit of detection, devices such as a paper test strip could be easily developed. In contrast, Pb^{2+} ions generated enhanced fluorescence of pepsin-protected Au NCs[66] demonstrating the possibility to detect molecules by fluorescence enhancing.

Another application of metal NCs include both *in vitro* (e.g. cell imaging) and *in vivo* (e.g. tumor imaging) bioimaging. One example being staining of nucleoli using the preference of Ag ions to bind to argyrophilic proteins located in it[67]. Compared with cellular imaging, *in vivo* imaging has the problem of the poor transmission of visible light through tissues[68], which could be overcome by metal NCs with far-red or near-infrared emission, or using nonlinear optics. Red-emitting BSA-protected Au NCs was used for a whole body real-time *in vivo* imaging, including tumor imaging in mouse. Emission of 710 nm from NC was easily distinguished from the autofluorescence of the body, and NC was cleared by the kidney, so after four weeks mice showed no signs of acute or long term toxic effects. With the help of the enhanced permeability and retention (EPR) effect ligand protected NCs also showed accumulation in tumors which allowed their imaging[69].

All together theoretical design of protected small noble metal nanoclusters with desired optical properties and their experimental verification has very attractive potential for different application areas.

4   Nonlinear optical (NLO) properties

The interaction of light with a matter induces absorption and emission when energies of incident photons are near the resonances of a molecular transitions. When the source of light is sufficiently strong, interaction between light and matter becomes nonlinear, and phenomenon like second harmonic generation (SHG), two or multi photon absorption occur. SHG is process in which photons with the same frequency are absorbed by nonlinear material and then a new photon with double energy is emitted. Two photon absorption (TPA) is process where two photons of identical or different energies are simultaneously absorbed. TPA depends quadratically on the light intensity, because it requires nearly simultaneous interaction of two photons with the molecule, in contrast to one-photon absorption (OPA), which is linear process. The rareness of this process can be depicted in the frequency of one- and two-photon process in rhodamine B dye. In the sunlight rhodamine B absorbs one photon about once a second and a photon pair every 10 million years[70]. This is the reason why TPA can only occur in interaction of mater with intense light.

Two photon absorption phenomenon was originally theoretically predicted by Maria Goeppert-Mayer in 1931[71], and in her honor the unit for molecular two-photon cross-section, which is measure of the probability of two photon absorption, is Goeppert-Mayer (GM), where 1 GM=10^{-50} cm^{4}s/photon. Few years later invention of laser as source of intense light permitted its experimental observation. But, only in the last 20 years, with the

development of sub-picosecond, and femtosecond pulsed lasers exploration of two-photon, and multiphoton processes experienced rapid growth. Today pulsed lasers improve the two-photon absorption rate 100,000 time, compared to continuous-wave laser at the same average power level. The most common laser for bioimaging application (fluorescence microscopy) has become the titanium:Sapphire crystal-based laser[72].

4.1 From basics towards applications

Nonlinear effect are found extremely useful in area of biological imaging in fluorescence microscopy method. This highly noninvasive method is used for high-resolution imaging of tissues, but also in live organisms, and the development of two-photon fluorescence light microscopy [73] revolutionized imaging of cells and tissues by allowing three-dimensional (3D) imaging. Although two-photon fluorescence is usually used, other nonlinear effect can be applied for imaging, like three-photon excited fluorescence[74], multiphoton excited fluorescence and second-harmonic generation[75].

Comparison of linear and nonlinear absorption shows that two-photon absorption has higher spatial resolution, deeper tissue penetration, less photodamage and reduced background signal from biological tissue. However, because of prolonged scanning with high intensity laser light negative photothermal effect can be induced.

Deeper tissue penetration is important advantage of two-photon microscopy over one photon. One limit for use of fluorescent dyes and one-photon imaging is opacity of tissue for visible light wavelengths. One way to solve this would be to use wavelengths for which tissue is transparent, such as ones in infrared region. If the fluorescent probe was a good two photon absorber, then it would be possible to excite it using two photon of lower energy (near infrared region) for which tissue is transparent. This property was used to track calcium 500 μm deep in mouse brain[76].

3D imaging by fluorescence microscopy inside living tissues is limited by light scattering that causes degradation of resolution and contrast, and deeper into the tissue this problem become more sever and high resolution imaging eventually becomes impossible. Confocal microscopy with its focusing lenses tried to overcome these problems, but absorption still occurs inside entire specimen, where large number of photons get scattered. These scattered photons move outside of focus and the information they carried is lost. To compensate for this signal loss, the intensity of light has to be increased which induces photobleaching and photodamage. These problems can be solved by the use of two-photon absorption in laser scanning microscopy. Dependence of the absorption probability on light intensity guarantees that the fluorescence is mostly generated in the vicinity of the geometrical focus where the light intensity is high, and nowhere else. Therefore, scanning can be done in all directions, gathering both scattered and focused fluorescence photon which have useful information on only single section of specimen which is in geometrical focus[75].

This also allows the depth discrimination and 3D imaging. While for one-photon excitation fluorescence signals are generated above and below the focal plane, in two-photon excitation fluorescence signal originates from a region approximately 1 mm thick about the focal point.

Two-photon absorption effects are proven to be strong in nanocluster containing systems, since their two-photon absorption cross sections are much larger then the typical values for organic biomolecules (cross section for Au_{25} in hexane is 427 000 GM[77], or DNA encapsu-

lated silver cluster 50 000 GM[78]).

So far, mechanism that governs these two-photon properties of ligated nanoclusters with few noble metal atoms is not explained, and influence of structural and electronic properties of different subunits of nanoclusters is not yet completely classified. Theoretical investigation of thiolated gold nanoclusters ($[Au_{12}(SG)_9]^{+1}$ and $[Au_{25}(SH)_{18}]^{-1}$) suggested large influence of resonance between OPA and TPA states which is partly responsible for large TPA cross sections[79]. Also, size effects were commented suggesting that larger sized NC have larger cross sections[79].

Due to the different selection rules of one-photon and two-photon excitations, different excited states can be reached by absorbing either one or two-photons, which means that the same molecule can have different emission properties depending on linear or nonlinear excitation type. This is specially pronounced in symmetrical molecules, where one-photon states are forbidden for two-photon excitations, therefore there is obvious difference in their OPA and TPA spectra[80]. It was also shown that oligonucleotide-encapsulated silver clusters have two-photon excited fluorescence (TPEF) spectra blue-shifted in comparisons to the corresponding one-photon excited fluorescence (OPEF)[78].

As far as the practical applications, advantages of two-photon excitation with near-infrared light were already used for two-photon cellular imaging by Au NCs containing systems. Dextran encapsulated Au NCs were used for two-photon imaging of human mesenchymal stem cells. Upon two-photon excitation with 800 nm, bright luminescence from protected Au NCs was observed in the cells[81]. Also, two-photon fluorescence microscopy was used to detect intracellular gold nanorods in rat basophilic leukaemia cells[82], where balance between high spatial resolution and photothermal effect on cells was investigated. Nice example of 3D-imaging is internalization of the AuNCs by live HeLa cells. AuNCs were protected using zwitterionic functional ligand, D-penicillamine, which assured excellent stability in aqueous solvent and good biocompatibility. 3D-imaging revealed liganded NCs inside the cells as well as attached to membrane[83].

4.2 Design of new NLO-phores

In analogy with investigations of linear apsorption, two-photon absorption was also first explored for organic dyes. However, these dyes had the two-photon cross sections lower than 10 GM, which is not convenient for application. But, with the increasing need for efficient two-photon absorbers in applications such as microscopy[75], three-dimensional data-storage[84], targeted photorelease of active biomolecules[85] and with development of quantum mechanical methods, design of organic dyes started. Since calculations of two-photon absorption are much more computational demanding then one-photon, access to advance computational technology is one of prerequisites for the exploration of new organic NLO-phores.

Because values of TPA cross sections are proportional to transition dipole moments, and reversely proportional to difference in energy of electronic states and incident photons, theoretical calculation suggested different strategies to enhance TPA cross sections. They include following suggestions[86]: (i) Long, π-conjugated systems that lead to high values of dipole moments; (ii) Substitution by donor and acceptor groups at the center and ends of the molecule that increase the potential for charge-transfer and enhance dipole moments; (iii) chromophores that have a strong OPA transition close to the incident two-photons

energy, thus making energy difference in denominator small which contributes to large TPA cross sections. However, if this energy difference is zero, TPA is not observed because of overlap with the OPA. So, there are two main contributions to large TPA cross sections in organic dyes: structure that promotes large transition dipole moments, and the possibility of resonance of OPA state and incident photons energy (when the energy of OPA state is roughly half the energy of the final two-photon state). In this way various push-pull structures were designed that exhibit enhanced TPA transitions, up to several thousand GM[87].

Similar investigations are needed for protected noble metal NCs that would enable strategies to design new metallic NLO-phores. In the end of this Introduction will be summarized one of the first results of investigation of nonlinear properties of protected silver clusters, and more detailed results are presented in Chapter 5 and 6.

5   Theoretical approaches

Properties of small metal clusters can be theoretically explored using quantum mechanics methods, where the main problem is to solve many body Schroedinger's equation which depends on large number of degrees of freedom. Elegant way to avoid this is not to search for wave function that describes the system, but electronic density which depends on only 3 spatial variables. This approach is basis of density functional theory (DFT), which is the most common method so far because of its sufficient accuracy and relatively low computational cost (for systems up to few hundred atoms). Method is based on Hohenberg-Kohn theorems [88] which state that the external potential is a unique functional of the ground-state density. Practical application was started by the Kohn-Sham idea of replacing the real interacting electrons by a noninteracting ones that reproduces the same density[89]. In this formulation of DFT, the exact ground-state density is constructed from the lowest occupied single-particle Kohn–Sham orbitals, which are not meant to reproduce wave function of the fully interacting system, just to produce the ground-state density. Unfortunately, external potential that determines ground state electron density consists of exchange-correlation part which is not known, but at least all the troublesome many-body interactions are inside this one quantity that can be approximated. Over the years distinct classes of functionals were developed based on different approximations, such as the local-density approximation, generalized gradient approximation, hybrid functionals...

When the system is under external perturbation, such as electric or magnetic field, it responds by exhibiting electronic transitions, induced dipoles or ionization, which can not be described by the ground state but excited states properties. Time dependent DFT (TDDFT) is extension of DFT theory developed to solve these problems. It is based on the Runge-Gross theorem [90] which is the time-dependent analog of the Hohenberg-Kohn theorem. It states that there is one-to-one correspondence between time-dependent densities and time-dependent one-body potentials, for a given initial state. Meaning that a given time change of the density can be generated by the time-dependent potential. Also, all the physical observables are essentially functionals of the time dependent density. Based on the van Leeuwen theorem it is possible to develop the time-dependent Kohn-Sham (TDKS) scheme in which time dependent density of an interacting system can be reproduced by a noninteracting system[91]. TDKS procedure basically consists of three steps: (i) Calculate the ground state,

by a static DFT calculation. This gives the initial orbitals (occupied and virtual); (ii) Solve TDKS equations selfconsistently, to obtain the TDKS orbitals which are used to form time dependent density. Used time-dependent exchange-correlation (xc) potential corresponds the static one from the initial DFT calculation; (iii) Calculate the desired properties as functionals of the time dependent density. Some excited state properties are not described well within the TDDFT, such as excitations where the electron is excited into a diffuse orbital (Rydberg states) or where an electron is transferred over a large distance (charge transfer states), conical intersections [92]. But, continuous development of new functionals tries to overcome these problems[93].

In the case when external perturbation is light, it reacts mostly with the valence electrons of the matter which induces electronic polarization of the material and different optical effects, like absorption and emission. Properties of materials can be independent of intensity of light (linear optics) or can change depending on it (non-linear optics). The calculation of NLO properties is computationally very demanding because it requires correct calculation of electron correlation, which is important for accurate predictions of molecular properties, but is crucial for accurate description of NLO properties.

5.1 Structural properties

Ground-state DFT is used to characterize properties of equilibrium state, which means that we want to determine quantities such as total ground-state energies, equilibrium geometries, bond lengths and bond angles, electronic density distributions, dipole moments and static polarizabilities, magnetic moments. But, this first step, finding the equilibrium structure, is not easy at all, because it involves simultaneous motion of both atomic nuclei and all the electrons. Most of the molecular dynamics (MD) methods usually employ Born-Oppenheimer approximation[94] that separates electronic and nuclear degrees of freedom, taking advantage of the large difference between the electronic and nuclear masses. This means that the electrons respond immediately to change of nuclear positions. This way two equations form, one describing electronic and another describing nuclear motion. Solving the Schroedinger's equations for electronic degrees of freedom, where the nuclear positions as fixed, electronic energy is obtained as a function of nuclear coordinates, which is potential energy surface that the nuclei feel. If the derivative of this energy with respect to nuclear coordinates is calculated, classical definition of the force on the nuclei is obtained, and can be used to solve Newton's equations of motion for nuclear movement. One objective of molecular dynamics can be geometry optimization, that is to find structure for which the molecule is the most stable. To be sure that obtained structure is indeed minimum, vibrational analysis is carried out.

Unfortunately, Born-Oppenheimer approximation (also known as the adiabatic approximation) is not universally valid, it breaks in some situations, one common example is when ground and excited electronic surfaces get very near, and the nuclei do not move continuously between connected ground states any more, but can "jump" on a new potential surface. This can not be described by Born-Oppenheimer approximation, and non-adiabatic quantum dynamics is needed for its correct description, where coupled equations with both the electrons and the nuclei are used.

The theoretical descriptions of nonadiabatic problems for molecular systems have different obstacles, from the possibilities to change between the excited states to different relax-

ation pathways, which should be described by quantum mechanics, but such calculations are computationally too demanding. One of the several semiclassical methods developed to investigate excited-state dynamics is the surface hopping approach[95]. Method models transitions between excited states as an instant jumps between two potential surfaces and the nuclei then move along the new adiabatic potential energy surface. The strength of the coupling between the states considered is defined by the "nonadiabatic coupling vector" which defines the hopping probability. This allows the jump to occur anywhere along the trajectory, and not just at localized avoided crossings where the coupling is the strongest.

5.2   Response theory

In many situations of practical interest, only a small perturbation is acting on a system, so they do not deviate strongly from their initial state. In this case, it is not necessary to solve the time-dependent Schroedinger or Kohn-Sham (KS) equations, instead, one can use perturbation theory. Because of the influence of perturbation, the molecular properties are no longer static, but change in time. These changes can be treated using response theory[96]. Each observable has its own response function. They are defined by considering a property (observable) as a function of an external perturbation expanded as a power series with respect to the perturbation strength, and at every order in the expansion there is specific physical property connected. So, response theory is actually perturbation theory that is focused on properties, and not states and energies. The standard response equations are a set of linear equations that determine the response of system. It describes changes of the molecular properties under influence of internal or external perturbations[97].

In the most applications of spectroscopy, when the light or electromagnetic radiation interacts with molecules, the wavelengths of light are longer then the dimensions of molecules, hence the approximation that the electric filed is constant over entire molecule is valid. This induces the electric dipole approximation, because in an expansion of electric field, only the molecular dipole moment will couple to the field, while magnetic interactions will not be included. So, dipole moment expanded as power series of the dipole electric field is connected in the first order with the polarizability, while the second order response gives the hyperpolarizability. To describe one and two photon absorption spectra, it is necessary to use both first order (linear) and second order (quadratic) response theory[98].

(a) Linear response

First step in response formalism is quite restrictive approximation that external perturbation is small, but it allows writing any operator (property) as function linear in perturbation strength. Using Fourier transformation leads to calculations in frequency space, where it can be seen that the system responds to external perturbation at the same frequency as perturbation.

For linear optical properties, linear density response function is of importance because it contains the information about absorption and excitation spectrum (as well as other properties connected with density)[99]. More precisely, oscillator strengths which characterize transitions between the ground state and excited states can be calculated using residues of response functions. In the first order expansion, response of the system will depend only on the properties of the ground state which allows the use of DFT. So benefit of the TDDFT linear response formalism is that only KS ground-state calculation (which is computationally less demanding) has to be done to obtain the density response.

(b) Quadratic response

If we take Fourier coefficients in the expansion of the expectation value of property (operator) in powers of the perturbation, we obtain different response functions. Second order term in this expansion is quadratic response function. Using residues of this function the TPA amplitude may be defined.

TPA cross section is proportional to two-photon absorption probability which is obtained using the two-photon absorption transition matrix[100]. Elements of this matrix can be written using a sum over state expression which includes transition dipole moments from ground state as well as between excited state as described in detail in Chapter 5. These second order transition moments can be identified from the single residue of the quadratic response function. Alternatively, two-photon matrix elements can be formulated within the sum over states (SOS) approach for the case where both photons have the same energy, orientationally averaged expressions for the two-photon matrix elements for linearly polarized photons with parallel polarization. This formulations allows the inclusion of the damping factor Γ which serves to prevent the TPA cross section from blowing up near the one-photon resonances.

6 Limitations and improvements of methods

Although, DFT and TDDFT offer balance between accuracy and efficiency (e.g. calculation cost scales as N^3, while wave function methods of similar accuracy, such as CCSD, CASSCF, scale with N^5) various challenges and problems are still to be solved within DFT and TDDFT.

- The time-dependent nonadiabatic exchange-correlation (xc) functionals need to be developed.

  The xc potential at each point depends on densities at all other points in space and at all previous times, but using adiabatic approximation, xc potential is actually ground states xc potential evaluated at the time-dependent density. For description of double excitations, Rydberg states, conical intersections nonadiabatic xc functionals are needed. Some attempts to solve this include electron-gas based functionals[101]; reduced density-matrix-functional theory[102]; many-body approaches[103].

- TDDFT for open systems which are connected to an environment or whose number of electrons is not conserved.

  Open systems include transport of electron, or energy from reservoir somewhere in the environment to a molecule. Questions to be solved include definition of the edge of system, type of boundary conditions, how to quantify the effect of the environment... The connection to a reservoir can be included in TDDFT in different ways: with a master equation approach[104], using stochastic methods[105], and by mapping the open physical system onto a noninteracting closed system[106].

- Development of xc functionals for strongly correlated systems.

  DFT and TDDFT have a problem in describing strongly correlated systems where electrons are not uniformly distributed, but are localized in orbitals at lattice sites, vastly

different in behavior from an electron gas. For 1D systems there have been some xc potential developed[107], and three-dimensional systems are also being developed[108].

- Extensions of TDDFT to include finite temperatures and relativistic effects.

  Ground-state DFT has been expanded to finite temperatures[109], but such theory is not yet implemented in TDDFT. Such, finite-temperature TDDFT would be able to describe elements of nonequilibrium thermodynamics, thermal ensembles and transport and thermoelectric properties. Relativistic TDDFT has to yet be formally defined, but some implementations have been used for calculating excitation energies[110], and Dirac-Kohn-Sham calculations have been preformed[111].

7 The structure and goals of this thesis

Aim of this thesis is to explore linear and nonlinear optical properties of hybrid systems of small noble metal nanoclusters. As structure (size, morphology, surface...) is vital for the properties of nanoclusters, it is of utmost importance to know precise structure of nanoclusters. So, theoretical simulation have twofold role: (i) they can serve as method of characterization of nanoclusters, and explain origin of optical properties of experimentally observed structures; (ii) they can stimulate experimental synthesis of structures with designed properties.

The present thesis is divided to two parts, exploring linear and nonlinear properties, respectively. In the first part, linear optical properties of aromatic rings and histidine-silver hybrids are explored. In the Chapter 2, influence of charges species on optical properties of 2,4-dinitrophenylhydrazine (DNPH) has been theoretically explored. DNPH consists of aromatic ring, with $-NHNH_2$ and two $-NO_2$ groups bound at para and ortho positions. TDDFT absorption spectra are calculated for neutral DNPH, and two classes of structures with H^+, Ag^+, Ag_3^+ bound to para and ortho $-NO_2$ groups. Both classes of isomers influence significantly spectroscopic patters of neutral DNPH, as described in detail in Chapter 2, but within the structural class, regardless if proton or silver was bound, the leading features of spectra are similar. These similarities are explained by internal Stark effect induced by the charge, and verified by placing point charges in the vicinity of $-NO_2$ groups at para and ortho position. Charges of different intensities induced similar spectroscopic patterns as proton and silver did, meaning shift of the first band towards larger wavelengths in case of ortho isomers and shift of first two bands and avoided crossing in the case of para isomer. These behaviors are result of different interactions of ground- and excited state dipole moments with the charge in para and ortho position. Using this optical features in combination with specific binding of DNPH to carbonylated proteins, offers application of DNPH in probing the charge in the vicinity of protein.

In Chapter 3 optical properties of hybrid systems composed of small silver clusters and histidine amino acid have been explored. Silver cluster have demonstrated their use as optical probes for biomolecular environment[48], stimulating research to understand the electronic excitations responsible for their unique optical properties. Histidine is very important amino acid which is involved in various biological processes, and unbalanced quantity of histidine-tagged proteins can indicate different diseases[112][113]. Therefore it is important to have reliable mechanism of labeling histidine. Comparison of calculated absorption spectra with

experimental photo-fragmentation yield allowed the structural characterization of the measured species revealing that silver preferentially binds to amino and carboxyl groups of amino acid. Three types of electronic excitations were found in protonated histidine and in the silver–histidine hybrids. These are: (i) the pure π–π^* transitions which are located at the imidazole subunit of histidine; (ii) charge transfer from a π-orbital of imidazole to an empty s-orbital of the Ag^+ ion and (iii) the S–P intracluster excitation within the Ag_3-cluster subunit. Bare histidine absorbs up to 230 nm, but presence of silver causes absorption up to 350 nm, and Ag_3 cluster induces increased intensity in the low energy region. This extension and enhancement of absorption can be used to improve detection sensitivity of histidine and histidine-tagged proteins.

Additionally, in Appendix A properties of silver clusters protected by thioglycolic acid ligands are explored in order to understand influence of different number of electrons which are confined within the metal cluster subunit on absorption spectra. Two different fragmentation pathway were investigated, one starting from two thioglycolic acid and three silver atoms, and another with three thioglycolic acids and four silver atoms. Initial structures do not have confined electrons and their absorption spectra are at wavelengths lower then 300 nm and are characterized by excitations from sulfur-silver binding orbitals to unoccupied orbitals within cluster. After fragmentation done in gas phase by collision induced dissociation and loss of specific number of CO_2 and S-CH_2 for each structure, structures with 2 confined electrons are formed. These structures are characterized by two electrons confined to silver subunit, which are responsible for intense transitions in absorption spectra. Structure with three silver atoms has one intense transition, and several weaker ones, while structure with four silver atoms has three intense transitions. All of them correspond to excitations within silver subunit, from S- to P-orbitals. This complementary experimental and theoretical investigations elucidated fragmentation pathways which lead to formation of liganded silver clusters, and their optical features, offering the possibility to produce in controlled way liganded metal clusters with specific number of electrons confined within the cluster core.

UV photodissociation of proline-containing peptide is described in Appendix B. Formation of different fragments depending od excitation wavelength was observed, and some unusual fragment ions were obtained, which are not present in fragmentation of peptides that do not contain proline. A tripeptide consisting of arginine-proline-lysine amino acids was studied both theoretically and experimentally. Calculations of absorption spectra showed that S_2 and S_3 states could be excited at the wavelength corresponding to experimental laser wavelengths, and non-adiabatic molecular dynamic simulation starting from these excited states indicated that excitation of peptide was followed by C-C and C-N bond activation close to the proline residue leading to breaking of these bonds. These findings reveal the mechanism of photofragmenatation of proline containing peptides which start by breaking the bonds close to proline, followed by proton transfers between fragments which leads to formation of unusual fragments.

In the second part of the thesis, nonlinear optical (NLO) properties are investigated. As already mentioned these properties are extraordinarily strong in metallic nanoclusters but the origin is not clear. In order to elucidate source of strong nonlinear properties, ligated Ag_{15} and Ag_{29} clusters were investigated.

In Chapter 4 both linear and nonlinear properties of thiolated Ag_{29} cluster were explored. Silver cluster was protected by ligand dihydrolipoic acid (DHLA). This nanocluster exhibited

highly fluorescent properties, emitting in the red part of the optical spectrum and having a long period stability[114][115]. Theoretical calculation in search for the global minimum were performed on model system with slightly simplified ligands: $Ag_{29}L_{12}$, L=-S-CH$_2$-CH$_2$-CH$_2$-S-, but due to large number of possible structures, have not been completely ascertain. Two classes of structures arise, with the central Ag atom present (the almost symmetric structure, but insufficient number of electrons to maintain it) or without it (other structural classes arise with different number of Ag atoms in core). Calculations of linear optical properties for system showed qualitative agreement with the experiment, and display several sharp transition bands in the UV-visible-NIR range. Experimentally, for excitation at 790 nm the TPA cross-section of 12 930 GM was measured, while two-photon emission is shifted in comparison with their linear one-photon excited fluorescence (OPEF), demonstrating that OPEF and tne-photon excited fluorescence (TPEF) do not obey the same transition rules. This opens new possibilities to tune emission of liganded NCs using either one- or two-photon excitations which could be used for controlled biolabeling and bioimaging.

In order to determine the origin of the parameters that influence TPA cross sections for ligated silver nanoclusters, $Ag_{15}SH_{11}$ nanocluster was thoroughly explored, as shown in the Chapter 5. TDDFT calculations on the $Ag_{15}SH_{11}$ clusters that has four confined electrons in the Ag_8 core, give huge TPA cross sections in the red part of the spectral region, and moderate TPA cross sections in near-IR. These exceptionally high TPA cross sections are dominated by resonance effects, because wavelength of S_1 state of OPA is very close to wavelengths of two incident photons. It was experimentally observed that this structure shows large one photon excited fluorescence[32], and measured TPA cross sections at 750 nm and 800 nm are in acceptable agreement with calculated ones. Considering that single residue quadratic response TDDFT can not accurately describe near resonance cases in TPA spectrum, sum over state (SOS) formula was implemented to overcome this problem.

On the basis of this excellent results for TPA cross section of Ag15SH11, further investigation was done on $Ag_{11}L_7$, $Ag_{15}L_{11}$ and $Ag_{31}L_{19}$ ligated clusters. Successful synthesis by size-focusing separation method allowed studying effects of changing cluster size on linear and nonlinear properties. Changing the size changes the optical band gap which influences resonance effect and charge transfer effects. Comparison of experimental and TDDFT obtained results allowed to describe necessary conditions for new nonlinear materials. OPA, OPEF and TPEF spectra were measured for all systems. OPA spectra are similar for $Ag_{11}L_7$ and $Ag_{15}L_{11}$ with plateau between 400-500 nm, while $Ag_{31}L_{19}$ exhibits large characteristic peak and 490 nm and smaller one at 700 nm[32]. $Ag_{11}L_7$ and $Ag_{15}L_{11}$ exhibit broad emission at 700 nm, while $Ag_{31}L_{19}$ has very weak emission. On the other hand when excited using two photon, $Ag_{31}L_{19}$ exhibits broad emission between 400-500 nm while red-shift in emission is observed for $Ag_{11}L_7$ and $Ag_{15}L_{11}$. This difference in emission spectra depending on one or two photon excitations has been also measured for $Ag_{29}(DHLA)_{12}$, and is caused by different selection rules for OPEF and TPEF. Theoretical calculations were done on systems where glutathione was modeled by SCH$_3$ group because computation of full glutatone ligand is not achievable within the present computational resources which can explain slight difference in experimentally and theoretically obtained results, which are otherwise in very good agreement. Calculations on these three systems revealed factors that play important role in large TPA cross sections: resonance between OPA and TPA states an large transition dipole moments which are favorable in systems with nonuniform distribution of electrons in core. Listed factors are present in $Ag_{15}L_{11}$ and $Ag_{31}L_{19}$ clusters, and absent in $Ag_{11}L_7$ which con-

sequently has small TPA cross sections. These results are first step towards understanding of origins of non-linear optical properties of ligated small clusters which will help proposing novel ligand-core NLO-phore, useful in bioimaging.

Bibliography

[1] Walt A. de Heer. *Rev. Mod. Phys.*, 65:611–676, Jul 1993. 3, 5

[2] Yukatsu Shichibu, Yuichi Negishi, Tatsuya Tsukuda, and Toshiharu Teranishi. *Journal of the American Chemical Society*, 127(39):13464–13465, 2005. 3

[3] T. G. Schaaff, M. N. Shafigullin, J. T. Khoury, I. Vezmar, R. L. Whetten, W. G. Cullen, P. N. First, C. Gutierrez-Wing, J. Ascensio, and M. J. Jose-Yacaman. *The Journal of Physical Chemistry B*, 101(40):7885–7891, 1997. 3

[4] V. Bonacic-Koutecky, L. Cespiva, P. Fantucci, J. Pittner, and J. Koutecky. *The Journal of Chemical Physics*, 100(1), 1994. 3

[5] V. Bonacic-Koutecky, L. Cespiva, P. Fantucci, and J. Koutecky. *The Journal of Chemical Physics*, 98(10), 1993. 3

[6] Vlasta Bonacic-Koutecky, Jaroslav Burda, Roland Mitric, Maofa Ge, Giuseppe Zampella, and Piercarlo Fantucci. *The Journal of Chemical Physics*, 117(7), 2002. 3

[7] Erik C. Dreaden, Alaaldin M. Alkilany, Xiaohua Huang, Catherine J. Murphy, and Mostafa A. El-Sayed. *Chem. Soc. Rev.*, 41:2740–2779, 2012. 4

[8] Rongchao Jin, Huifeng Qian, Zhikun Wu, Yan Zhu, Manzhou Zhu, Ashok Mohanty, and Niti Garg. *The Journal of Physical Chemistry Letters*, 1(19):2903–2910, 2010. 4, 6, 8

[9] Udaya Bhaskara Rao and T. Pradeep. *Angewandte Chemie International Edition*, 49 (23):3925–3929, 2010. 4

[10] Hongwei Duan and Shuming Nie. *Journal of the American Chemical Society*, 129(9): 2412–2413, 2007. 4

[11] T. G. Dietz, M. A. Duncan, D. E. Powers, and R. E. Smalley. *The Journal of Chemical Physics*, 74(11), 1981. 4

[12] Masamichi Yamashita and John B. Fenn. *The Journal of Physical Chemistry*, 88(20): 4451–4459, 1984. 4

[13] Marin Vojkovic, Driss Rayane, Franck Bertorelle, Rodolphe Antoine, Michel Broyer, and Philippe Dugourd. *International Journal of Mass Spectrometry*, 387:45 – 50, 2015. 4

[14] V. Bonačić-Koutecký, R. Mitric, C. Burgel, and J. Petersen. *Tailoring Functionality of Clusters and Their Complexes with Biomolecules by Size, Structures, and Lasers*. Elsevier, December 2010. 4

[15] Thibault Tabarin, Alexander Kulesza, Rodolphe Antoine, Roland Mitric, Michel Broyer, Philippe Dugourd, and Vlasta Bonacic-Koutecky. *Physical Review Letters*, 101:213001, Nov 2008. 4, 8

[16] Shruti R. Saptarshi, Albert Duschl, and Andreas L. Lopata. *Journal of Nanobiotechnology*, 11(1):1–12, 2013. 4

[17] Nishima Wangoo, C. Raman Suri, and G. Shekhawat. *Applied Physics Letters*, 92(13): 133104, 2008. 4

[18] Geoffrey A. Ozin and Helmut Huber. *Inorganic Chemistry*, 17(1):155–163, 1978. 4

[19] L. Konig, I. Rabin, W. Schulze, and G. Ertl. *Science*, 274(5291):1353–1354, 1996. 4

[20] Gert De Cremer, Bert F. Sels, Jun-ichi Hotta, Maarten B. J. Roeffaers, Evelyne Bartholomeeusen, Eduardo Coutiño-Gonzalez, Valentin Valtchev, Dirk E. De Vos, Tom Vosch, and Johan Hofkens. *Advanced Materials*, 22(9):957–960, 2010. 4

[21] Jie Zheng and Robert M. Dickson. *Journal of the American Chemical Society*, 124 (47):13982–13983, 2002. 4

[22] Jie Zheng, Caiwei Zhang, and Robert M. Dickson. *Phys. Rev. Lett.*, 93:077402, Aug 2004. 4, 7

[23] Yu-Chen Jao, Meng-Kai Chen, and Shu-Yi Lin. *Chem. Commun.*, 46:2626–2628, 2010. 4

[24] Chris I. Richards, Sungmoon Choi, Jung-Cheng Hsiang, Yasuko Antoku, Tom Vosch, Angelo Bongiorno, Yih-Ling Tzeng, and Robert M. Dickson. *Journal of the American Chemical Society*, 130(15):5038–5039, 2008. 4

[25] E. G. Gwinn, P. O'Neill, A. J. Guerrero, D. Bouwmeester, and D. K. Fygenson. *Advanced Materials*, 20(2):279–283, 2008. 4

[26] Thumu Udaya B. Rao, Bodappa Nataraju, and Thalappil Pradeep. *Journal of the American Chemical Society*, 132(46):16304–16307, 2010. 4

[27] Jianping Xie, Yuangang Zheng, and Jackie Y. Ying. *Journal of the American Chemical Society*, 131(3):888–889, 2009. 5

[28] Hui Wei, Zidong Wang, Limin Yang, Shiliang Tian, Changjun Hou, and Yi Lu. *Analyst*, 135:1406–1410, 2010. 5

[29] Xavier Le Guevel, Nicole Daum, and Marc Schneider. *Nanotechnology*, 22(27):275103, 2011. 5

[30] W. D. Knight, Keith Clemenger, Walt A. de Heer, Winston A. Saunders, M. Y. Chou, and Marvin L. Cohen. *Phys. Rev. Lett.*, 52:2141–2143, Jun 1984. 5

[31] Michael Walter, Jaakko Akola, Olga Lopez-Acevedo, Pablo D. Jadzinsky, Guillermo Calero, Christopher J. Ackerson, Robert L. Whetten, Henrik Grönbeck, and Hannu Häkkinen. *Proceedings of the National Academy of Sciences*, 105(27):9157–9162, 2008. 5

[32] Franck Bertorelle, Ramzi Hamouda, Driss Rayane, Michel Broyer, Rodolphe Antoine, Philippe Dugourd, Lars Gell, Alexander Kulesza, Roland Mitric, and Vlasta Bonacic-Koutecky. *Nanoscale*, 5:5637–5643, 2013. 5, 6, 18

[33] Wyrwas, R. B., Alvarez, M. M., Khoury, J. T., Price, R. C., Schaaff, T. G., and Whetten, R. L. *Eur. Phys. J. D*, 43(1), 2007. doi: 10.1140/epjd/e2007-00117-6. 5

[34] Yuichi Negishi, Katsuyuki Nobusada, and Tatsuya Tsukuda. *Journal of the American Chemical Society*, 127(14):5261–5270, 2005. 5

[35] Santosh Kumar, Michael D. Bolan, and Terry P. Bigioni. *Journal of the American Chemical Society*, 132(38):13141–13143, 2010. 5

[36] Pablo D. Jadzinsky, Guillermo Calero, Christopher J. Ackerson, David A. Bushnell, and Roger D. Kornberg. *Science*, 318(5849):430–433, 2007. 5

[37] M. Zhu, Ch. M. Aikens, F. J. Hollander, G. C. Schatz, and R. Jin. *Journal of the American Chemical Society*, 130(18):5883–5885, 2008. 5

[38] Chenjie Zeng, Chong Liu, Yuxiang Chen, Nathaniel L. Rosi, and Rongchao Jin. *Journal of the American Chemical Society*, 136(34):11922–11925, 2014. 6

[39] Anindita Das, Tao Li, Gao Li, Katsuyuki Nobusada, Chenjie Zeng, Nathaniel L. Rosi, and Rongchao Jin. *Nanoscale*, 6:6458–6462, 2014. 6

[40] Chenjie Zeng, Tao Li, Anindita Das, Nathaniel L. Rosi, and Rongchao Jin. *Journal of the American Chemical Society*, 135(27):10011–10013, 2013. 6

[41] Chenjie Zeng, Huifeng Qian, Tao Li, Gao Li, Nathaniel L. Rosi, Bokwon Yoon, Robert N. Barnett, Robert L. Whetten, Uzi Landman, and Rongchao Jin. *Angewandte Chemie International Edition*, 51(52):13114–13118, 2012. 6

[42] Huayan Yang, Huaqi Wang, Yuand Huang, Lars Gell, Lauri Lehtovaara, Sami Malola, Hannu Häkkinen, and Nanfeng Zheng. *Nature Communications*, 4:2422, 2013. 6

[43] Megalamane Siddaramappa Bootharaju, Victor M. Burlakov, Tabot M. D. Besong, Chakra P. Joshi, Lina G. AbdulHalim, David M. Black, Robert L. Whetten, Alain Goriely, and Osman M. Bakr. *Chemistry of Materials*, 27(12):4289–4297, 2015. 6

[44] Jingshu Guo, Santosh Kumar, Michael Bolan, Anil Desireddy, Terry P. Bigioni, and Wendell P. Griffith. *Analytical Chemistry*, 84(12):5304–5308, 2012. 6

[45] Anil Desireddy, Santosh Kumar, Jingshu Guo, Michael D. Bolan, Wendell P. Griffith, and Terry P. Bigioni. *Nanoscale*, 5:2036–2044, 2013. 6

[46] P. E. Blochl. *Phys. Rev. B*, 50:17953–17979, Dec 1994. 6

[47] Yizhong Lu and Wei Chen. *Chem. Soc. Rev.*, 41:3594–3623, 2012. 6

[48] Vlasta Bonacic-Koutecky, Alexander Kulesza, Lars Gell, Roland Mitric, Rodolphe Antoine, Franck Bertorelle, Ramzi Hamouda, Driss Rayane, Michel Broyer, Thibault Tabarin, and Philippe Dugourd. *Phys. Chem. Chem. Phys.*, 14:9282–9290, 2012. 7, 8, 16

[49] Alexander Kulesza, Roland Mitrić, and Vlasta Bonačić-Koutecký. *Chemical Physics Letters*, 501(4–6):211 – 214, 2011. 7

[50] Roland Mitric, Jens Petersen, Alexander Kulesza, Vlasta Bonacic-Koutecky, Thibault Tabarin, Isabelle Compagnon, Rodolphe Antoine, Michel Broyer, and Philippe Dugourd. *J. Chem. Phys.*, 127(13):134301, 2007. 7, 8

[51] Jie Zheng, Philip R. Nicovich, and Robert M. Dickson. *Annual Review of Physical Chemistry*, 58(1):409–431, 2007. 7

[52] Zhikun Wu and Rongchao Jin. *Nano Letters*, 10(7):2568–2573, 2010. 7

[53] Isabel Diez, Matti Pusa, Sakari Kulmala, Hua Jiang, Andreas Walther, Anja Goldmann, Axel Muller, Olli Ikkala, and Robin Ras. *Angewandte Chemie International Edition*, 48(12):2122–2125, 2009. 7

[54] Tiantian Cao, Shenshen Jin, Shuxin Wang, Dandan Zhang, Xiangming Meng, and Manzhou Zhu. *Nanoscale*, 5:7589–7595, 2013. 7

[55] Alexander Kulesza, Roland Mitric, and Vlasta Bonacic-Koutecky. *The Journal of Physical Chemistry A*, 113(16):3783–3788, 2009. 8

[56] Alexander Kulesza, Roland Mitric, Vlasta Bonacic-Koutecky, Bruno Bellina, Isabelle Compagnon, Michel Broyer, Rodolphe Antoine, and Philippe Dugourd. *Angewandte Chemie International Edition*, 50(4):878–881, 2011. 8

[57] Achillefs N. Kapanidis and Shimon Weiss. *The Journal of Chemical Physics*, 117(24), 2002. 8

[58] Ryoko Ando, Hideaki Mizuno, and Atsushi Miyawaki. *Science*, 306(5700):1370–1373, 2004. 8

[59] Sungmoon Choi, Robert M. Dickson, and Junhua Yu. *Chem. Soc. Rev.*, 41:1867–1891, 2012. 8

[60] Zhentao Luo, Kaiyuan Zheng, and Jianping Xie. *Chem. Commun.*, 50:5143–5155, 2014. 8

[61] Prasenjit Maity, Songhai Xie, Miho Yamauchi, and Tatsuya Tsukuda. *Nanoscale*, 4:4027–4037, 2012. 8

[62] T. Udayabhaskararao and T. Pradeep. *The Journal of Physical Chemistry Letters*, 4(9):1553–1564, 2013. 8

[63] Yong Yu, Qiaofeng Yao, Zhentao Luo, Xun Yuan, Jim Yang Lee, and Jianping Xie. *Nanoscale*, 5:4606–4620, 2013. 8

[64] Jianping Xie, Yuangang Zheng, and Jackie Y. Ying. *Chem. Commun.*, 46:961–963, 2010. 9

[65] Weiwei Guo, Jipei Yuan, and Erkang Wang. *Chem. Commun.*, pages 3395–3397, 2009. 9

[66] Hideya Kawasaki, Kenji Hamaguchi, Issey Osaka, and Ryuichi Arakawa. *Advanced Functional Materials*, 21(18):3508–3515, 2011. 9

[67] Junhua Yu, Sungmoon Choi, Chris I Richards, Yasuko Antoku, and Robert M Dickson. *Photochemistry and photobiology*, 84:1435–1439, 2008. 9

[68] Jianghong Rao, Anca Dragulescu-Andrasi, and Hequan Yao. *Current Opinion in Biotechnology*, 18(1):17 – 25, 2007. 9

[69] Xu Wu, Xiaoxiao He, Kemin Wang, Can Xie, Bing Zhou, and Zhihe Qing. *Nanoscale*, 2:2244–2249, 2010. 9

[70] W. Denk and K. Svoboda. *Neuron*, 18(3):351–357, 1997. 9

[71] Maria Goeppert Mayer. *Die Naturwissenschaften*, 17:932, 1929. 9

[72] D. E. Spence, P. N. Kean, and W. Sibbett. *Opt. Lett.*, 16(1):42–44, Jan 1991. 10

[73] W Denk, JH Strickler, and WW Webb. *Science*, 248(4):73–76, 1990. 10

[74] R M Williams, J B Shear, W R Zipfel, S Maiti, and W W Webb. *Biophys J*, 76(4951): 1835–1846, 1999. 10

[75] Warren R Zipfel, Rebecca M Williams, and Watt W Webb. *Nature Biotechnology*, 21: 1369–1377, 2003. 10, 11

[76] Andreas Frick, Jeffrey Magee, Helmut J. Koester, Michele Migliore, and Daniel Johnston. *The Journal of Neuroscience*, 23(8):3243–3250, 2003. 10

[77] Isabelle Russier-Antoine, Franck Bertorelle, Marin Vojkovic, Driss Rayane, Estelle Salmon, Christian Jonin, Philippe Dugourd, Rodolphe Antoine, and Pierre-Francois Brevet. *Nanoscale*, 6:13572–13578, 2014. 10

[78] Sandeep A. Patel, Chris I. Richards, Jung-Cheng Hsiang, and Robert M. Dickson. *Journal of the American Chemical Society*, 130(35):11602–11603, 2008. 11

[79] Paul N. Day, Kiet A. Nguyen, and Ruth Pachter. *Journal of Chemical Theory and Computation*, 6(9):2809–2821, 2010. 11

[80] J. I. Steinfeld. *Molecules and Radiation.* Dover edition, 2005. 11

[81] Chien-Liang Liu, Mei-Lin Ho, Yu-Chun Chen, Cheng-Chih Hsieh, Yi-Chih Lin, Yu-Hsiu Wang, Meng-Ju Yang, Hsin-Sheng Duan, Bo-So Chen, Jyh-Fu Lee, Jong-Kai Hsiao, and Pi-Tai Chou. *The Journal of Physical Chemistry C*, 113(50):21082–21089, 2009. 11

[82] Y. Zhou, X. Wu, T. Wang, T. Ming, P.N. Wang, L.W. Zhou, and J.Y. Chen. *Journal of Microscopy*, 237(2):200–207, 2010. 11

[83] Li Shang, Rene M. Dorlich, Stefan Brandholt, Reinhard Schneider, Vanessa Trouillet, Michael Bruns, Dagmar Gerthsen, and G. Ulrich Nienhaus. *Nanoscale*, 3:2009–2014, 2011. 11

[84] Satoshi Kawata, , and Yoshimasa Kawata. *Chemical Reviews*, 100(5):1777–1788, 2000. 11

[85] Graham C R Ellis-Davies. *Nature methods*, 4:619–628, 2007. 11

[86] Milosz Pawlicki, Hazel A. Collins, Robert G. Denning, and Harry L. Anderson. *Angewandte Chemie International Edition*, 48(18):3244–3266, 2009. 11

[87] T. Kogej, D. Beljonne, F. Meyers, J.W. Perry, S.R. Marder, and J.L. Bredas. *Chemical Physics Letters*, 298(1–3):1 – 6, 1998. 12

[88] P. Hohenberg and W. Kohn. *Phys. Rev.*, 136(3B):B864–B871, Nov 1964. 12

[89] W. Kohn and L. J. Sham. *Phys. Rev.*, 140:A1133–A1138, Nov 1965. 12

[90] Erich Runge and E. K. U. Gross. *Phys. Rev. Lett.*, 52:997–1000, Mar 1984. 12

[91] Robert van Leeuwen. *Phys. Rev. Lett.*, 82:3863–3866, May 1999. 12

[92] A. Dreuw and M. Head-Gordon. *Chemical Reviews*, 105(11):4009–4037, 2005. 13

[93] M.A.L. Marques and E.K.U. Gross. *Annual Review of Physical Chemistry*, 55(1): 427–455, 2004. 13

[94] M. Born and R. Oppenheimer. *Annalen der Physik*, 389(20):457–484, 1927. 13

[95] John C. Tully and Richard K. Preston. *The Journal of Chemical Physics*, 55(2), 1971. 14

[96] Jeppe Olsen and Poul Jorgensen. *The Journal of Chemical Physics*, 82(7), 1985. 14

[97] Pawel Salek, Olav Vahtras, Trygve Helgaker, and Hans Agren. *The Journal of Chemical Physics*, 117(21), 2002. 14

[98] D. P. Craig and T. Thirunamachandran. *Molecular Quantum Electrodynamics*. Dover edition, 1998. 14

[99] Carsten A. Ullrich and Zeng-hui Yang. *Brazilian Journal of Physics*, 44(1):154–188, 2014. 14

[100] W. Martin McClain. *Accounts of Chemical Research*, 7(5):129–135, 1974. 15

[101] C. A. Ullrich. *The Journal of Chemical Physics*, 125(23):234108, 2006. 15

[102] K. J. H. Giesbertz, E. J. Baerends, and O. V. Gritsenko. *Phys. Rev. Lett.*, 101:033004, Jul 2008. 15

[103] N Sakkinen, M Manninen, and R van Leeuwen. *New Journal of Physics*, 14:013032, 2012. 15

[104] Kieron Burke, Roberto Car, and Ralph Gebauer. *Phys. Rev. Lett.*, 94:146803, Apr 2005. 15

[105] R Biele and R D'Agosta. *Journal of Physics: Condensed Matter*, 24(27):273201, 2012. 15

[106] David G. Tempel, Mark A. Watson, Roberto Olivares-Amaya, and Alán Aspuru-Guzik. *The Journal of Chemical Physics*, 134(7):074116, 2011. 15

[107] Claudio Verdozzi. *Phys. Rev. Lett.*, 101:166401, Oct 2008. 16

[108] Daniel Karlsson, Antonio Privitera, and Claudio Verdozzi. *Phys. Rev. Lett.*, 106: 116401, Mar 2011. 16

[109] N. David Mermin. *Phys. Rev.*, 137:A1441–A1443, Mar 1965. 16

[110] Johan Henriksson, Trond Saue, and Patrick Norman. *The Journal of Chemical Physics*, 128(2):024105, 2008. 16

[111] Leonardo Belpassi, Loriano Storchi, Harry M. Quiney, and Francesco Tarantelli. *Phys. Chem. Chem. Phys.*, 13:12368–12394, 2011. 16

[112] Hidehiko Saito, Lawrence T. Goodnough, James M. Boyle, and Norbert Heimburger. *The American Journal of Medicine*, 73:179–182, 1997. 16

[113] Allison L Jones, Mark D Hulett, and Christopher R Parish. *Immunol Cell Biol*, 83: 106–118, 2005. 16

[114] Bimalendu Adhikari and Arindam Banerjee. *Chemistry of Materials*, 22(15):4364–4371, 2010. 18

[115] Patrick T K Chin, Marte van der Linden, Elleke J van Harten, Arjan Barendregt, Marcus T M Rood, Abraham J Koster, Fijs W B van Leeuwen, Celso de Mello Donega, Albert J R Heck, and Andries Meijerink. *Nanotechnology*, 24(7):075703, 2013. 18

Chapter 2

Cation induced electrochromism in 2,4-dinitrophenylhydrazine (DNPH): Tuning optical properties of aromatic rings

Cation induced electrochromism in 2,4-dinitrophenylhydrazine (DNPH): Tuning optical properties of aromatic rings

Željka Sanader [a], Claire Brunet [b], Michel Broyer [b], Rodolphe Antoine [b], Philippe Dugourd [b], Roland Mitrić [c], Vlasta Bonačić-Koutecký [a,d,*]

[a] Center for Advanced Science and Technology (ICAST), University of Split, Meštrovićevo Šetalište 45, 2100 Split, Croatia
[b] Institut Lumière Matière, UMR5306 Université Lyon 1-CNRS, Université de Lyon, 69622 Villeurbanne cedex, France
[c] Department of Physics, Free University Berlin, Arnimallee 14, 14195 Berlin, Germany
[d] Insitute für Chemie, Humboldt-Universität zu Berlin, Brook-Taylor-Straße 2, 12489 Berlin, Germany,

ARTICLE INFO

ABSTRACT

We have theoretically investigated the influence of protons and noble metal cations on optical properties of 2,4-dinitrophenylhydrazine (DNPH). We show that optical properties of aromatic rings can be tuned by cation-induced electrochromism in DNPH due to binding to specific NO_2 groups. Our findings on cation-induced electrochromism in DNPH may open new routes in two different application areas, due to the fact that DNPH can easily bind to biological molecules and surface materials through carbonyl groups.

© 2013 Elsevier B.V. All rights reserved.

1. Introduction

Intermolecular interactions involving aromatic rings are playing a significant role in chemistry and biology [1]. In particular, the importance of interactions between aromatic rings and metal ions has been widely recognized and studied [2]. Noncovalent interactions between cations and π rings, represent one of the most important intermolecular binding in context of molecular recognition [2,3]. Valuable insights into structural and bonding properties of cation–π ring interactions were investigated on model compounds using gas-phase ion chemistry [4–7], IR spectroscopy [8–10] and theoretical approaches [11–16].

Another type of interaction between π rings and metal ions can arise through a direct cationization (e.g. with protons for instance) on the ring. This has a dramatical effect on delocalised electrons in the ring and therefore on absorption spectra, thus producing large band shifts with respect to neutral species [17–20]. This is of importance for applications in optoelectronics and sensorics, as it has been shown recently by tuning the optical properties of π-conjugated heterocycles by cationization [21–23].

Finally, interaction with ion can take place outside the aromatic ring without influencing conjugation. This situation occurs for example when the prothestic aromatic groups of proteins are close to a charge provided by the protein skeleton or due to interaction with charged ligands [24–26]. In this case, the observed shifts of light absorption and emission bands are due to internal Stark effect (or internal electrochromism). The electrochromic response is based on direct interaction of the ground- and excited-state dipole moments of the chromophore with the applied electric field [27]. Electrochromism does not require direct electronic coupling of the chromophore with the recognition group and therefore opens new routes to design different sensors with desired properties. In spite of its potential importance, this effect has been only scarcely investigated for aromatic ring molecules [28–30].

In this Letter, we theoretically explore the influence of protons and noble metal cations on optical properties of 2,4-dinitrophenyl-hydrazine (DNPH). DNPH is a benzene ring with an $NHNH_2$ group, and two $-NO_2$ groups bound at para and ortho positions (as displayed in inset in Figure 1). Due to the presence of NO_2 groups at different position on the benzene ring, DNPH is a good prototype for studying the influence of positively charged groups (e.g. Ag^+, H^+, or Ag_3^+) on its optical properties. We wish to show that optical properties of aromatic rings can be tuned by cation-induced electrochromism in DNPH due to binding to specific NO_2 groups.

2. Computational details

Density functional theory (DFT) has been used to determine the structural properties of neutral DNPH, protonated and argentinated DNPH, using the Perdew–Burke–Ernzerhof exchange–correlation functional (PBE0) [31] with Split Valence Polarized (SVP) [32] atomic basis set. For silver atom, the relativistic effective core potential (RECP) of the Stuttgart group has been employed [33]. The harmonic vibrational frequencies were calculated in order to determine the stationary points. The absorption spectra have been calculated within the TDDFT, using either PBE0 functional with SVP basis set or employing the long range correcting version of the hybrid B3LYP functional using Coulomb-attenuated method
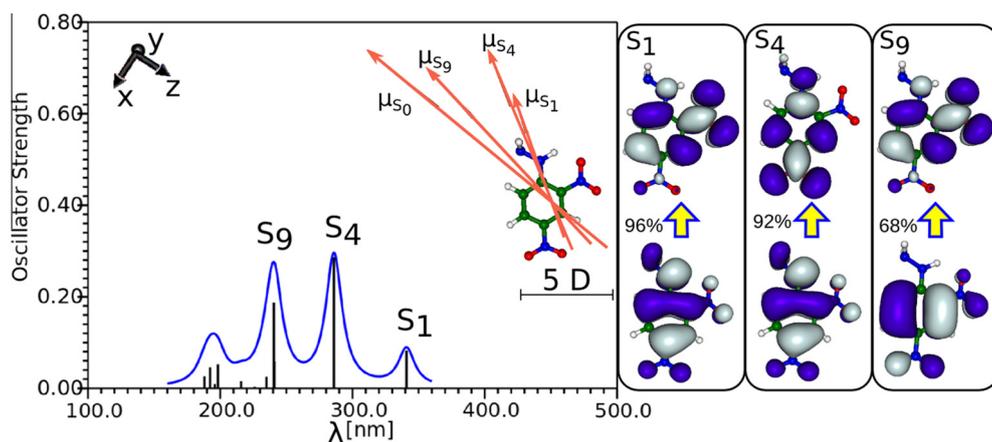
Figure 1. TDDFT absorption spectrum of neutral DNPH using PBE0 functional and SVP basis set (left). The leading excitations for the transitions to S_1, S_4 and S_9 excited states (right). (Cut-off for orbitals is 0.02, minus and plus signs are labeled by blue and grey colors respectively). The dipole moment vectors of the ground state and S_1, S_4 and S_9 excited states are shown in the upper part of the figure together with *xyz* directions (the corresponding dipole moment vector values in Debye are given in Table S1 in Supplementary content). (For interpretation of the references to color in this figure legend, the reader is referred to the web version of this article.)

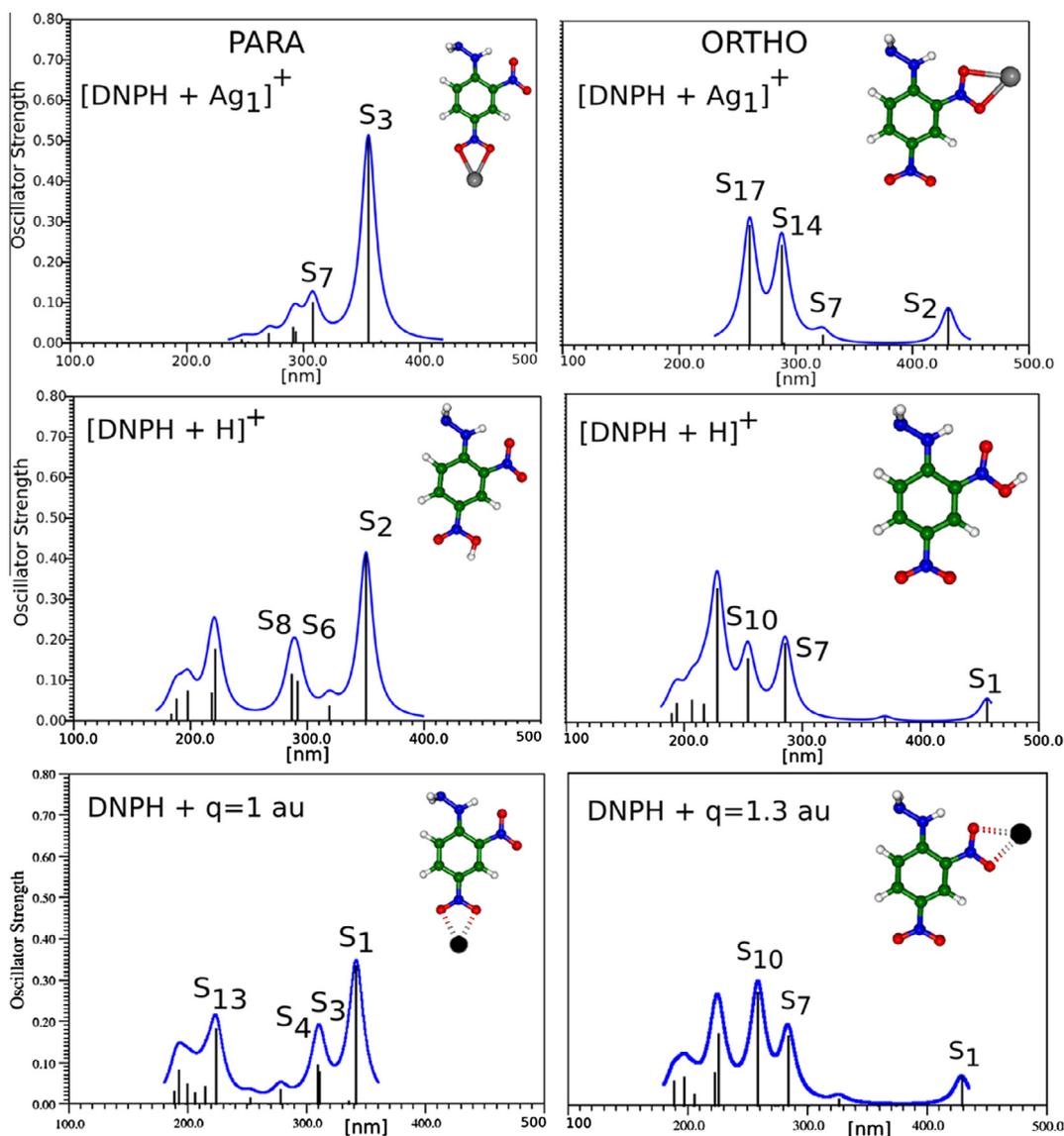**Figure 2.** TDDFT calculated absorption spectra using PBE0 functional and SVP basis set for [DNPH + Ag]$^+$, [DNPH + H]$^+$ and DNPH plus a point charge q. Results for para (left) and ortho (right) isomers are shown (the ortho isomer for [DNPH + Ag]$^+$ is 0.11 eV higher in energy than the para isomer, while ortho isomer for [DNPH + H]$^+$ is 0.3 eV higher than the para isomer).

(CAM-B3LYP) [34] which provides a reliable description of charge transfer transitions.

In a fact, the calculated spectra for protonated and argentinated DNPH with PBE0 and with CAM-B3LYP are similar. The slightly blue shift for the charge transfer state (about 20 nm) has been obtained using CAM-B3LYP, confirming that accuracy of PBE0 is acceptable for our study.

3. Results

First, the TDDFT calculated absorption spectrum of neutral DNPH displayed in Figure 1 shows the first allowed transition at 340 nm and two additional transitions S_4 and S_9 at 288 and 240 nm respectively. These transitions arise from excitations either within the aromatic ring and or including NO_2 groups, as shown on the right-hand side of Figure 1. In order to investigate the influence of cation nature (Ag^+ or H^+) on absorption spectrum of DNPH, the spectra for two classes of structures with cations bound to NO_2 group at para- and ortho- positions are shown in Figure 2. The spectroscopic patterns differ substantially for para and ortho- positions of cations. Moreover, since the optical spectra for protonated DNPH and for its complex with Ag^+ are very similar in particular in the low energy region, it is to expect that the spectroscopic patterns are driven by charge effect. For this reason, we placed a point charge at para and ortho positions of NO_2 as shown in the lower panels in Figure 2. We obtained almost identical spectroscopic patterns to those obtained for protonated and argentinated DNPH. Notice that if the Ag^+ ion is replaced by Ag_3^+ cluster, the same effect on spectroscopic patterns has been found (see Figure S1 in Supplementary content). Since the spectroscopic patterns did not change, the conclusion can be drawn that the different shifts observed for both classes of isomers (para and ortho) can be fundamentally explained by internal Stark effect. Comparing these spectra with the spectrum of neutral DNPH, it is possible to see (left panel in Figure 2) that for the para position of charge, the first intense transition is slightly redshifted but its intensity has significantly increased. In the case of ortho position (right panel in Figure 2), the first intense transition is strongly red-shifted and has comparable intensity with the corresponding transition for neutral DNPH. Red shifts of the lowest intense transitions with respect to the DNPH are also in correspondence with the trends in values of HOMO–LUMO energy gaps (see Table S2 in Supplementary content). Notice that the para isomer is lower in energy than the ortho isomer in all three cases.

In order to confirm the hypothesis of internal Stark effect induced by the charge, we have calculated the optical spectra of DNPH as a function of the strength of the point charge for para and ortho isomers allowing to follow shifts of the transitions as well as changes in their intensities, as shown in Figure 3. In order to better address the Stark effect, the evolution of the energy of the first bands as a function of the point charge value are given in Figure S2 in Supplementary content. The influence of electric field is different for para and ortho isomers. In the case of para isomer, an avoided crossing between two first bands occurs as the value of the point change increases (cf Figure S2).This is responsible for the evolution of the position of the bands as well as for the exchange of the intensities between first two bands after avoided crossing. Consistently with this, the character of transitions is inverted between the two first bands (S_3 and S_7, compare Figure S3a in Supplementary content) with respect to those of DNPH (S_1 and S_4, compare Figure 1). For ortho isomer, the situation is different and simpler since the red-shift of the first band is increasing with the strength of the charge as shown in Figure 3b (first-order Stark effect). Therefore intensity as well as the character of the transition are not modified as it is shown in Figure S3b, in Supplementary
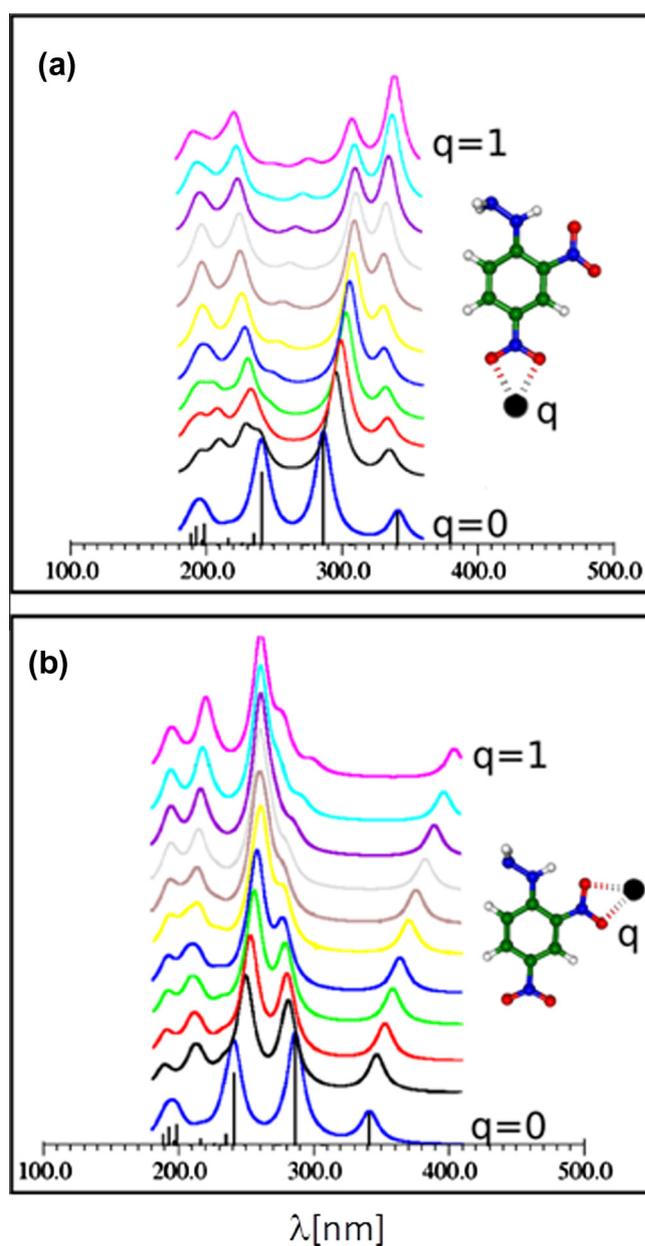

Figure 3. Influence of the strength of point charge located at (a) para and (b) ortho positions at NO_2 groups of DNPH on absorption patterns. Point charge q is varied from 0 (corresponding to neutral DNPH, bottom of the figures) to 1 a.u. by steps of 0.1 a.u.

content. These behaviors are due to different orientations and strength of ground- and excited states dipole moments in interaction with a charge in para and ortho position (see Figure 1).

4. Discussion and conclusion

Our theoretical investigation indicate that the effects of cations on the optical properties of the benzene ring can be fundamentally explained by internal Stark effect. Such effects can be mimic by external static electric fields. Our findings on cation-induced electrochromism in DNPH may open new routes in two different application areas, due to the fact that DNPH can easily bind to biological molecules and surface materials through carbonyl groups.

(i) DNPH is used to probe carbonylated proteins. Indeed, most current methods for determining protein carbonyl content

are based on the reaction of carbonyl groups with DNPH, which can then be detected and quantified spectrophotometrically or immunochemically [35]. Since the optical properties of DNPH are extremely sensitive upon the charge and its location, DNPH might be a good marker to probe the charge (both cations and anions) in proteins as a function of environment (e.g. pH modifications, binding of other molecules to DNPH).

(ii) Optical properties (both absorption and fluorescence) of organic materials could be tuned by using DNPH with added charges or external field, opening possible applications for opto-electronic [36]. For example, one might use carbonyl groups (in analogy to carbonylated proteins) on oxidized diamond electrodes [37] for producing highly oriented DNPH monolayers, for which color tuning could be performed by an applied electric field.

Acknowledgements

Appendix A. Supplementary data

Supplementary data associated with this article can be found, in the online version, at http://dx.doi.org/10.1016/j.cplett.2013.03.049.

References

[1] E.A. Meyer, R.K. Castellano, F. Diederich, Angew. Chem. Int. Ed. 42 (2003) 1210.
[2] J.C. Ma, D.A. Dougherty, Chem. Rev. 97 (1997) 1303.
[3] D.A. Dougherty, Science 271 (1996) 163.
[4] K.F. Willey, C.S. Yeh, D.L. Robbins, M.A. Duncan, J. Phys. Chem. 96 (1992) 9106.
[5] K.F. Willey, P.Y. Cheng, M.B. Bishop, M.A. Duncan, J. Am. Chem. Soc. 113 (1991) 4721.
[6] P. Weis, P.R. Kemper, M.T. Bowers, J. Phys. Chem. A 101 (1997) 8207.
[7] V. Ryzhov, R.C. Dunbar, B. Cerda, C. Wesdemiotis, J. Am. Soc. Mass Spectrom. 11 (2000) 1037.
[8] H.-B. Yi, H.M. Lee, K.S. Kim, J. Chem. Theory Comput. 5 (2009) 1709.
[9] N.C. Polfer, J. Oomens, R.C. Dunbar, Phys. Chem. Chem. Phys. 8 (2006) 2744.
[10] A. Lagutschenkov, R.K. Sinha, P. Maitre, O. Dopfer, J. Phys. Chem. A 114 (2010) 11053.
[11] Y.S. Yang, W.Y. Hsu, H.F. Lee, Y.C. Huang, C.S. Yeh, C.H. Hu, J. Phys. Chem. A 103 (1999) 11287.
[12] A.S. Reddy, G.N. Sastry, J. Phys. Chem. A 109 (2005) 8893.
[13] J.B. Nicholas, B.P. Hay, D.A. Dixon, J. Phys. Chem. A 103 (1999) 1394.
[14] N.L. Ma, K.M. Ng, C.W. Tsang, Chem. Phys. Lett. 277 (1997) 306.
[15] T.D. Jaeger, D. van Heijnsbergen, S.J. Klippenstein, G. von Helden, G. Meijer, M.A. Duncan, J. Am. Chem. Soc. 126 (2004) 10981.
[16] C.W. Bauschlicher, H. Partridge, S.R. Langhoff, J. Phys. Chem. 96 (1992) 3273.
[17] R. Omidyan, Chem. Phys. Lett. 518 (2011) 15.
[18] B.S. Freiser, J.L. Beauchamp, J. Am. Chem. Soc. 98 (1976) 3136.
[19] I. Alata, R. Omidyan, M. Broquier, C. Dedonder, O. Dopfer, C. Jouvet, Phys. Chem. Chem. Phys. 12 (2010) 14456.
[20] I. Alata, M. Broquier, C. Dedonder, C. Jouvet, E. Marceca, Chem. Phys. 393 (2011) 25.
[21] A.J. Zucchero, J.N. Wilson, U.H.F. Bunz, J. Am. Chem. Soc. 128 (2006) 11872.
[22] Z. Zhang et al., J. Am. Chem. Soc. 134 (2012) 4076.
[23] J.M. Hancock, S.A. Jenekhe, Macromolecules 41 (2008) 6864.
[24] J.T. Vivian, P.R. Callis, Biophys. J. 80 (2001) 2093.
[25] P.G. Papadopoulos, S.A. Walter, J.W. Li, G.M. Baker, Biochemistry 30 (1991) 840.
[26] R.C. Davis, S.L. Ditson, A.F. Fentiman, R.M. Pearlstein, J. Am. Chem. Soc. 103 (1981) 6823.
[27] A.S. Klymchenko, A.P. Demchenko, J. Am. Chem. Soc. 124 (2002) 12372.
[28] D. Rai, H. Joshit, A.D. Kulkarni, S.P. Gejji, R.K. Pathak, J. Phys. Chem. A 111 (2007) 9111.
[29] Q. Enjalbert et al., J. Phys. Chem. B 116 (2012) 841.
[30] Y.C. Choi, W.Y. Kim, K.S. Park, P. Tarakeshwar, K.S. Kim, T.S. Kim, J.Y. Lee, J. Chem. Phys. 122 (2005) 094706.
[31] J.P. Perdew, K. Burke, M. Ernzerhof, Phys. Rev. Lett. 77 (1996) 3865.
[32] F. Weigend, R. Ahlrichs, Phys. Chem. Chem. Phys. 7 (2005) 3297.
[33] D. Andrae, U. Haeussermann, M. Dolg, H. Stoll, H. Preuss, Theor. Chim. Acta 77 (1990) 123.
[34] T. Yanai, D.P. Tew, N.C. Handy, Chem. Phys. Lett. 393 (2004) 51.
[35] F. Matthijssens, B.P. Braeckman, J.R. Vanfleteren, Curr. Anal. Chem. 3 (2007) 93.
[36] K. Gurunathan, A.V. Murugan, R. Marimuthu, U.P. Mulik, D.P. Amalnerkar, Mater. Chem. Phys. 61 (1999) 173.
[37] H. Notsu, I. Yagi, T. Tatsuma, D.A. Tryk, A. Fujishima, J. Electroanal. Chem. 492 (2000) 31.

Chapter 3

The nature of electronic excitations at the metal–bioorganic interface illustrated on histidine–silver hybrids

The nature of electronic excitations at the metal–bioorganic interface illustrated on histidine–silver hybrids†

Željka Sanader,[a] Roland Mitrić,*[b] Vlasta Bonačić-Koutecký,*[ac] Bruno Bellina,[de] Rodolphe Antoine[de] and Philippe Dugourd*[de]

We present a joint theoretical and experimental study of the structure selective optical properties of cationic and anionic histidine–silver complexes with Ag and Ag$_3$ which were prepared in the gas phase using mass spectroscopy coupled to electrospray ion source. Our TDDFT calculations provide general insight into the nature of electronic excitations at the metal–bioorganic interface that involve $\pi-\pi^*$ excitation within bio-organic subunits, charge transfer between two subunits and intrametallic excitations. The binding of silver to histidine, one of the most important amino acids, induces red shift in the optical absorption of protonated histidine particularly for anionic species. The presence of the smallest metallic subunit Ag$_3$ increases the intensity of low energy transitions of histidine illustrating a metal cluster-induced enhancement of absorption of biomolecules in hybrid systems. Comparison of calculated absorption spectra with experimental photo-fragmentation yield provides structural assignment of the measured spectroscopic patterns. Our findings may serve to establish silver-labeling as the tool for the detection of histidine or histidine-tagged proteins.

1. Introduction

Metal nanoparticles became attractive in recent years as promising labels for optical detection and imaging of biomolecules.[1] In the meantime it has also been recognized that small silver nanoclusters with only a few atoms produce scaffold-specific optical signals which makes them suitable for optical probing of their biomolecular environment.[2] Thus, characterization and understanding of electronic excitations responsible for the absorption and emission at the interface between metallic particles and biomolecules are of high interest in the context of designing building blocks for new biosensing materials.[3–5] The successful preparation of ligand-protected silver clusters has been achieved only recently[6–10] and their fluorescence properties with different ligands were investigated.[11,12] In general, the

[a] Interdisciplinary Center for Advanced Sciences and Technology (ICAST), University of Split, Meštrovićevo šetalište 45, HR-2100 Split, Republic of Croatia

[b] Julius-Maximilians-Universität, Würzburg, Germany. E-mail: roland.mitric@uni-wuerzburg.de

[c] Department of Chemistry, Humboldt-Universität zu Berlin, Brook-Taylor-Str. 2, 12489 Berlin, Germany. E-mail: vbk@chemie.hu-berlin.de; Fax: +49 30 2093-5573; Tel: +49 30 2093-5579

[d] Université Lyon 1-CNRS, Université de Lyon, 69622 Villeurbanne cedex, France

[e] UMR5306, Institut Lumière Matière, Villeurbanne, France. E-mail: dugourd@lasim.univ-lyon1.fr

† Electronic supplementary information (ESI) available. See DOI: 10.1039/c3cp52712c

electronic excitations in this class of systems involve charge transfer (CT) between the subunits as well as specific excitations within the metallic and biomolecular subunits, which may interact in a subtle way producing new absorption and emission properties. Our previous studies focused on silver cluster–peptide hybrids containing tryptophan aromatic amino acid.[13–18] In such hybrid cluster–biomolecule systems, excitations within both interacting subunits are of molecular discrete nature. The metallic subunit extends and enhances significantly the absorption of the biomolecule subunit into the near UV energy regime.

In addition to tryptophan, histidine is one of the most important amino acids that has been extensively studied due to its biochemical importance. Histidine is involved in various biological processes including enzymatic catalysis.[19] It can act as a catalytic site in certain enzymes and as a coordinating ligand in metalloproteins.[20] As biological molecules, histidine and histidine-tagged proteins play a critical biological role in the human body.[21] An abnormal level of histidine-tagged proteins is an indicator of many diseases such as advanced liver cirrhosis,[22] AIDS,[23] renal disease,[23] asthma,[24] pulmonary disorders,[25] thrombotic disorders[24,26] and malaria.[27]

The affinity of histidine for metal ions can be used in quantitative chemical analysis. Immobilized metal-affinity chromatography was found to be primarily useful for the purification of proteins with natural surface exposed residues and for recombinant proteins with engineered histidine tags or histidine clusters.[28] Interestingly, histidine is one of the strongest silver-ion binders.[29] Imidazole[30] and histidine[31–33] were thus used as efficient capping

This journal is © the Owner Societies 2014

Phys. Chem. Chem. Phys., 2014, **16**, 1257–1261 | 1257

ligands for metal nanoparticles. Histidine-capped silver colloids were recently synthesized and have found application for Ni_2^+ detection as well as for biosensing due to their unique surface enhanced Raman scattering signals. Vibrational spectroscopy of amino acids adsorbed on metal surfaces is quite complex due to the fact that anions, cations or even zwitterionic species can give rise to SERS signals. Moreover, the interaction with the metal ions may take place through only one or more functional groups. Thus, in parallel, gas phase approaches have been proposed to better address the relation between structural and binding motifs in histidine ions and their optical properties. Theoretical investigations[34] and action IR spectroscopy[35,36] have been successfully applied to protonated histidine and cationized histidine with alkali metals.

Therefore, in order to understand and characterize the silver–histidine interface and to characterize the nature of the involved electronic excitations, in this contribution we investigate charged cationic *vs.* anionic hybrids containing up to three silver atoms and compare them to the protonated species.

2. Computational and experimental

Density functional theory (DFT) has been used to determine the structural properties of protonated histidine and histidine silver complexes. The TZVP atomic orbital basis set was used for all atoms.[37] An extensive search for structures was performed using simulated annealing coupled to molecular dynamics (MD) simulations in the frame of the semiempirical AM1 method[38] with parameters for Ag atoms. The structures identified in this way were subsequently reoptimized at the DFT level using gradient minimization techniques, and stationary points were characterized by calculating the harmonic vibrational frequencies. For this purpose, as well as for the absorption spectra, we employed the long-range corrected version of the hybrid B3LYP functional using the Coulomb attenuated method (CAM-B3LYP),[39] which provides a reliable description of charge-transfer transitions. In addition, comparison with the more accurate equation-of-motion coupled cluster method with single and double excitations (EOM-CCSD)[40] has been made for imidazole–Ag^+ species.

Imidazole, histidine and $AgNO_3$ were purchased from Sigma Aldrich. The complexes were prepared by mixing a solution of 100 μM of $AgNO_3$ with 100 μM of histidine (or imidazole) in distilled water. Mass spectrometry and photodissociation measurements were performed using a modified LTQ Velos (Thermo electron) ion trap coupled to a tunable optical parametric oscillator (OPO) laser.[41] The solution was electrosprayed and analyzed by mass spectrometry. $[His + H]^+$, $[His + Ag]^+$, $[imidazole + Ag]^+$ and $[His + Ag − 2H]^-$ were directly observed in the full mass spectrum. Hybrids composed of a histidine amino acid and silver trimers were produced by combining electrospray ionization and multiple stage mass spectrometry.[42,43] The $[His + Ag_3]^+$ complex was formed in trap by collision induced fragmentation of the precursor ion $[(His)_2 + 3Ag − 2H]^+$. The $[His + Ag_3 − 2H]^-$ complex was formed in trap by collision induced fragmentation of the precursor ion $[(His)_2 + 3Ag − 4H]^-$.

The laser is a nanosecond frequency-doubled tunable Panther™ EX OPO laser pumped by a Powerlite™ II Nd:YAG

laser (both from Continuum, Santa Clara, CA, USA). The laser beam passes through two diaphragms (2 mm in diameter) and lenses after which it is injected on the axis of the linear trap through a quartz window fitted on the rear of the LTQ Velos chamber.[41] An electromechanical shutter, electronically synchronized with the mass spectrometer, was placed along the laser beam and allowed to inject the laser light according to a given time sequence. To perform laser irradiation (10 laser shots) for a given period of time, we add in the ion trap RF sequence an MS^n step with an activation amplitude of 0%, during which the shutter located on the laser beam is opened. The different steps of ion selection and excitation are successively carried out in the high pressure cell. Final product ions are then transferred and mass analyzed in the low pressure cell.

The photofragmentation yield is defined as $σ = \ln((I_{precursor} + Σ_{frag})/I_{precursor})/φ$ where $I_{precursor}$ and $Σ_{frag}$ are the intensity of the precursor ion signals and sum of photofragments and $φ$ is the laser fluence. For $[His + Ag − 2H]^-$, the main fragment ion is silver ion (m/z 107), while for $[His + Ag]^+$, internal amino-acid fragments (mainly loss of CO_2 with and without silver (m/z 218 and 110) and a fragment ion at m/z 82 corresponding to ionized Cα–Cβ side chain residue) are observed (see Fig. S1 in ESI†). For complexes with silver trimers, the main fragmentation channel is the loss of Ag_2.

3. Results and discussion

In Fig. 1 we illustrate three general types of electronic excitations which can arise in protonated histidine and at the silver–histidine interface. These include the pure π–π⋆ transitions which are localized at the imidazole subunit, charge transfer from a π-orbital of imidazole to an empty s-orbital of the Ag^+ ion and finally the S–P intracluster excitation within the Ag_3-cluster subunit. The interplay between these illustrated prototype excitations determines the absorption and emission in silver–histidine hybrids and can serve as a general characterization of
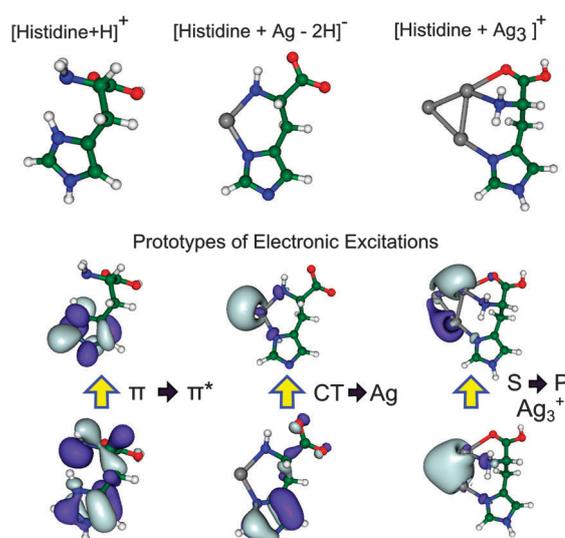

Fig. 1 Characterization of classes of electronic excitations in protonated histidine and silver–histidine complexes.
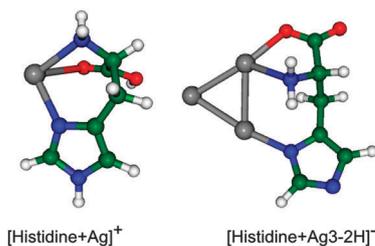
Fig. 2 The lowest energy structures for cationic [His + Ag]⁺ and anionic [His + Ag₃ − 2H]⁻ species, complementary to anionic and cationic complexes in the middle and right upper part of Fig. 1.

the metal–bioinorganic interface. It should be pointed out that the nature of the electronic excitations is closely connected with the structural binding motifs. In general, silver ions have a strong affinity for binding to the free electron pairs present in the amino group (NH_2) and in the carboxy group (COOH) of an amino acid. In the case of histidine, there are additional binding sites due to the presence of nitrogen within the imidazole ring. In Fig. 1, in the most stable structure of [His + H]⁺ the proton is bound to the free N-atom in the imidazole subunit. The structure with a protonated amino group lies 0.19 eV higher in energy (compare Fig. S2 in ESI†). In [His + Ag − 2H]⁻, the silver is bidented and bound to nitrogen atoms of the amino and imidazole moieties. For [His + Ag₃]⁺, an additional bond to the carboxy group is observed.

Structures of cationic and anionic complexes with Ag and Ag₃ are shown in Fig. 1 and 2. In the case of the silver trimer, the same binding motif is observed for cations and anions. In [His + Ag]⁺, silver is tridented, similarly to what is observed for the silver trimer species (for structures of all isomers see Fig. S3 and S4, ESI†). The lowest energy structure of [His + Ag]⁺ is closely related to structures found for alkali atoms bound to histidine.[36]

We start to present the optical properties of protonated histidine which will serve as a reference system for comparison with a metal model for ion–histidine complexes.

The first intense optical transition is located at 200 nm and corresponds to the π–π* excitation in the S₂ excited state (cf. Fig. 1) as shown in Fig. 3. The lowest excited state S₁ at 207 nm has almost no intensity and is of mixed character involving both the π-system as well as the amino acid moiety. Spectra calculated using the TDDFT method and the experimental spectrum are in qualitative agreement. The onset of absorption just above 200 nm is reproduced by the experimental data. In Fig. 3b, we compare the absorption spectrum for another reference system [imidazole + Ag]⁺ calculated with EOM-CCSD and TDDFT methods and experimental data. This illustrates that quantitative agreement with experimental findings is achievable with the EOM-CCSD method, in particular for excited states with charge transfer nature, which is the case for the S₁ state while TDDFT also provides qualitative agreement and is substantially less computationally demanding.

Experimental spectra of histidine complexes with one silver atom are shown in Fig. 4.

For the cation species, the fragmentation yield increases with the photon energy exhibiting 2 clear bands at 230 and 270 nm. For the anion species, two broad bands centered at 260
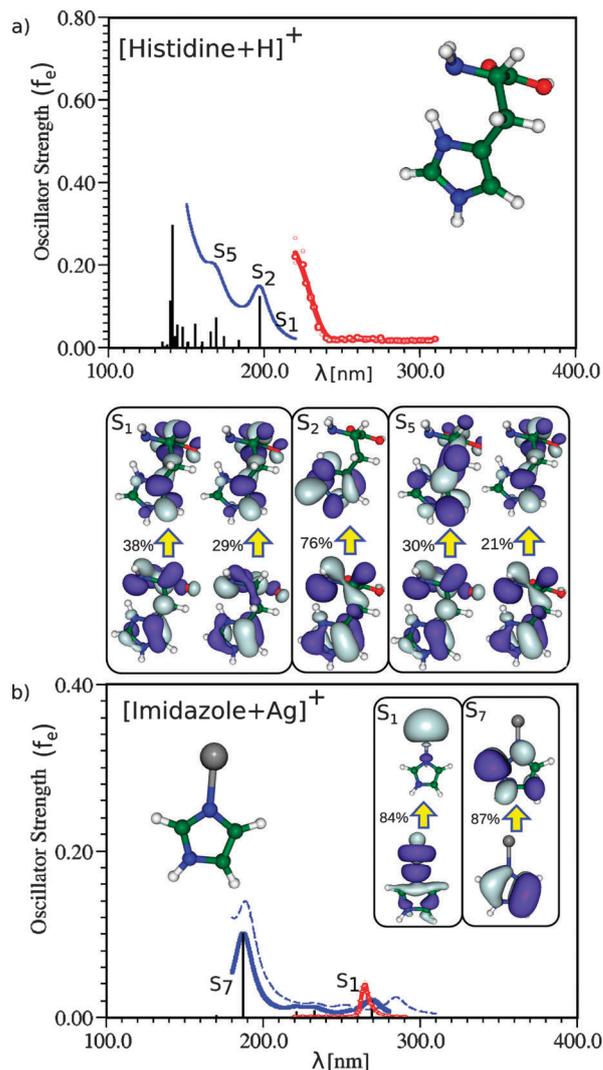

Fig. 3 Comparison between calculated (blue line) and experimental (red line) optical spectra of reference systems (a) protonated histidine (TDDFT with CAMB3LYP and TZVP basis sets) (b) [Imidazole + Ag]⁺ complex (EOM-CCSD and TZVPP basis sets − full blue line, TDDFT with CAMB3LYP and TZVP basis sets − dashed blue line).

and 300 nm are observed. While in protonated histidine, the absorption is mainly due to π–π* excitations, the comparison of the calculated and measured spectra of the lowest structure of [His + Ag]⁺ and [His + Ag − 2H]⁻ shown in Fig. 4 reveals that the lowest electronic transitions into first excited states are either forbidden (in the case of cations) or characterized by the charge transfer excitations into an empty s-orbital of Ag⁺ (in the case of anions). Due to the long range CT character these transitions have very low intensities. The agreement with experimental data in the range between 210 and 300 nm is reasonable. In general, the anionic complexes have lower energy transitions than the cationic ones due to the weaker binding of an extra electron.

In contrast to the species with one silver atom, the smallest cluster subunit of Ag₃ interacting with histidine in [His + Ag₃]⁺ and [His + Ag₃ − 2H]⁻ induces a strong influence of excitations within the cluster which gives rise to intense electronic
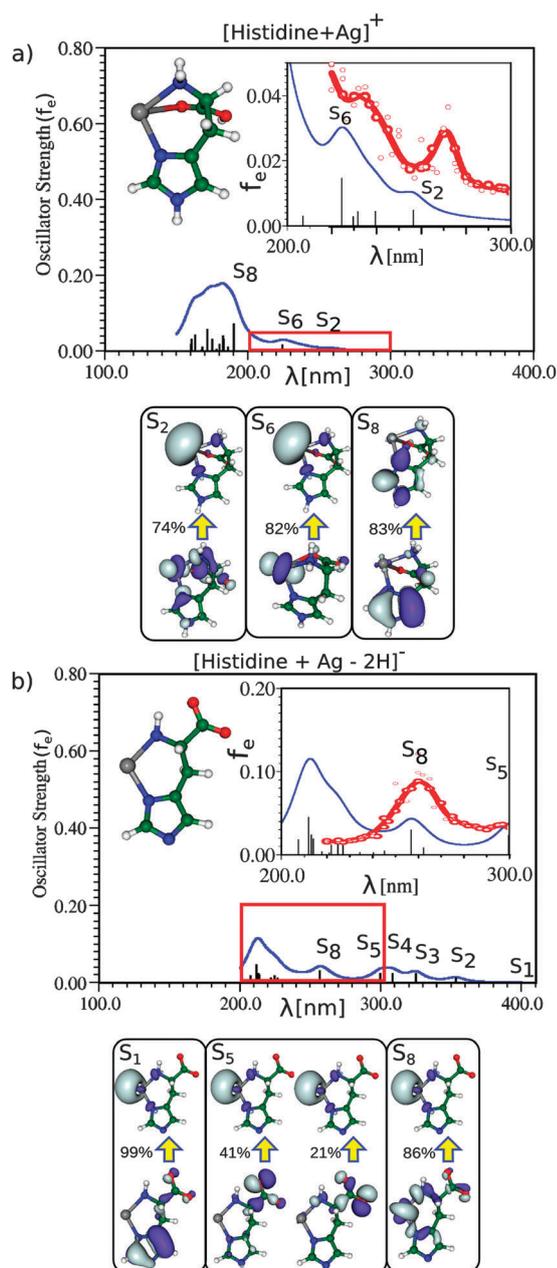
This journal is © the Owner Societies 2014

Phys. Chem. Chem. Phys., 2014, 16, 1257–1261 | 1259

Fig. 4 Comparison of calculated (blue line) and experimental (red line) optical spectra of the lowest energy structures of (a) the cationic [Histidine + Ag]$^+$ complex and (b) the anionic [Histidine + Ag − 2H]$^-$ complex (camB3LYP with TZVP), together with analysis of leading electronic excitations for several excited states.

Fig. 5 Comparison of calculated (blue line) and experimental (red line) spectra of the lowest energy structures of (a) the cationic [Histidine + Ag$_3$]$^+$ complex and (b) the anionic [Histidine + Ag$_3$ − 2H]$^-$ complex (camB3LYP with TZVP), together with analysis of leading electronic excitations for several excited states. The calculated electron density difference $\rho(S_1 - S_0)$ is shown on the right side.

transitions at around 300 nm for cations and 340 nm for anions (*cf.* Fig. 5).

The analysis of the excitations given in Fig. 5 shows dominant characteristics of intense S–P transitions within the cluster for the lowest excited states (*cf.* Fig. 1). This is also confirmed by the electron density difference between the ground and excited states, which is for anionic species presented in Fig. 5. The excited states above 300 nm with some intensity are characterized by the increased mixing with CT excitations from the π-system. The agreement with experimental data in the experimentally

accessible range below 300 nm is excellent for the cation and reasonable for the anion.

4. Conclusions

We have presented a joint theoretical and experimental study of the optical properties of cationic and anionic histidine complexes with Ag and Ag$_3$ and compared them with those of the protonated histidine. We have identified three general prototypes of electronic excitations at the metal bioorganic interface that involve π–π* excitations within bioorganic subunits, charge transfer between two subunits and intrametallic excitation within the cluster subunit. The binding of silver to histidine induces optical absorption up to ∼350 nm, while the bare histidine only absorbs up to ∼230 nm. The presence of an intact metal Ag$_3$ subunit leads to an

increase in the intensity of the transitions in the low energy region. All these properties may serve to establish silver-labelling as a tool for the detection of histidine or histidine-tagged proteins. In particular, the increase in the intensity due to the cluster-effect may improve the detection sensitivity considerably.[21] These findings should serve as a basis for developing protein detection and quantification techniques based either on direct fluorescence detection *in vivo*[44] or at nanostructured surfaces.[45]

Acknowledgements

Notes and references

1 E. Katz and I. Willner, *Angew. Chem., Int. Ed.*, 2004, **43**(45), 6042–6108.
2 V. Bonacic-Koutecky, A. Kulesza, L. Gell, R. Mitric, R. Antoine, F. Bertorelle, R. Hamouda, D. Rayane, M. Broyer, T. Tabarin and P. Dugourd, *Phys. Chem. Chem. Phys.*, 2012, **14**(26), 9282–9290.
3 C.-A. J. Lin, C.-H. Lee, J.-T. Hsieh, H.-H. Wang, J. K. Li, J.-L. Shen, W.-H. Chan, H.-I. Yeh and W. H. Chang, *J. Med. Biol. Eng.*, 2009, **29**(6), 276–283.
4 L. Shang, S. Dong and G. U. Nienhaus, *Nano Today*, 2011, **6**(4), 401–418.
5 J. Yu, S. Choi, C. I. Richards, Y. Antoku and R. M. Dickson, *Photochem. Photobiol.*, 2008, **84**(6), 1435–1439.
6 N. Nishida, H. Yao, T. Ueda, A. Sasaki and K. Kimura, *Chem. Mater.*, 2007, **19**(11), 2831–2841.
7 Y. Cui, Y. Wang, R. Liu, Z. Sun, Y. Wei, Y. Zhao and X. Gao, *ACS Nano*, 2011, **5**(11), 8684–8689.
8 S. Kumar, M. D. Bolan and T. P. Bigioni, *J. Am. Chem. Soc.*, 2010, **132**(38), 13141–13143.
9 T. U. B. Rao, B. Nataraju and T. Pradeep, *J. Am. Chem. Soc.*, 2010, **132**(46), 16304–16307.
10 F. Bertorelle, R. Hamouda, D. Rayane, M. Broyer, R. Antoine, P. Dugourd, L. Gell, A. Kulesza, R. Mitric and V. Bonacic-Koutecky, *Nanoscale*, 2013, **5**, 5637–5643.
11 I. Diez and R. H. A. Ras, *Nanoscale*, 2011, **3**(5), 1963–1970.
12 T. Udaya Bhaskara Rao and T. Pradeep, *Angew. Chem., Int. Ed.*, 2010, **49**(23), 3925–3929.
13 I. Compagnon, T. Tabarin, R. Antoine, M. Broyer, P. Dugourd, R. Mitric, J. Petersen and V. Bonacic-Koutecky, *J. Chem. Phys.*, 2006, **125**(16), 164326.
14 R. Mitric, J. Petersen, A. Kulesza, V. BonaCic-Koutecky, T. Tabarin, I. Compagnon, R. Antoine, M. Broyer and P. Dugourd, *J. Chem. Phys.*, 2007, **127**(13), 134301.
15 T. Tabarin, A. Kulesza, R. Antoine, R. Mitrić, M. Broyer, P. Dugourd and V. Bonačić-Koutecký, *Phys. Rev. Lett.*, 2008, **101**(21), 213001.
16 A. Kulesza, R. Mitrić and V. Bonačić-Koutecký, *Chem. Phys. Lett.*, 2011, **501**(4–6), 211–214.
17 A. Kulesza, R. Mitric and V. Bonačić-Koutecký, *J. Phys. Chem. A*, 2009, **113**(16), 3783–3788.
18 A. Kulesza, R. Mitrić, V. Bonačić-Koutecký, B. Bellina, I. Compagnon, M. Broyer, R. Antoine and P. Dugourd, *Angew. Chem., Int. Ed.*, 2011, **50**(4), 878–881.
19 J. M. Berg, J. L. Tymoczko and L. Stryer, *Biochemistry*, W. H. Freeman and Company, New York, 6th edn, 2007.
20 R. J. Sundberg and R. B. Martin, *Chem. Rev.*, 1974, **74**(4), 471–517.
21 D. R. Bae, W. S. Han, J. M. Lim, S. Kang, J. Y. Lee, D. Kang and J. H. Jung, *Langmuir*, 2009, **26**(3), 2181–2185.
22 H. Saito, L. T. Goodnough, J. M. Boyle and N. Heimburger, *Am. J. Med.*, 1982, **73**(2), 179–182.
23 A. L. Jones, M. D. Hulett and C. R. Parish, *Immunol. Cell Biol.*, 2005, **83**(2), 106–118.
24 L. Engesser, C. Kluft, E. Briët and E. J. P. Brommer, *Br. J. Haematol.*, 1987, **67**(3), 355–358.
25 W. T. Morgan, *Biochem. Med. Metab. Biol.*, 1986, **36**(2), 210–213.
26 C. Kuhli, I. Scharrer, F. Koch and L.-O. Hattenbach, *Am. J. Ophthalmol.*, 2003, **135**(2), 232–234.
27 D. J. Sullivan, I. Gluzman and D. Goldberg, *Science*, 1996, **271**, 219–222.
28 V. Gaberc-Porekar and V. Menart, *J. Biochem. Biophys. Methods*, 2001, **49**(1–3), 335–360.
29 T. Shoeib, K. W. M. Siu and A. C. Hopkinson, *J. Phys. Chem. A*, 2002, **106**(25), 6121–6128.
30 V. V. Vukovic and J. M. Nedeljkovic, *Langmuir*, 1993, **9**(4), 980–983.
31 J. Guan, L. Jiang, J. Li and W. Yang, *J. Phys. Chem. C*, 2008, **112**(9), 3267–3271.
32 Z. Liu, Z. Xing, Y. Zu, S. Tan, L. Zhao, Z. Zhou and T. Sun, *Mater. Sci. Eng., C*, 2012, **32**(4), 811–816.
33 Z. Liu, Y. Zu, Y. Fu, R. Meng, S. Guo, Z. Xing and S. Tan, *Colloids Surf., B*, 2010, **76**(1), 311–316.
34 Z. Huang, Z. Lin and C. Song, *J. Phys. Chem. A*, 2007, **111**(20), 4340–4352.
35 M. Citir, C. S. Hinton, J. Oomens, J. D. Steill and P. B. Armentrout, *Int. J. Mass Spectrom.*, 2012, **330–332**, 6–15.
36 M. Citir, C. S. Hinton, J. Oomens, J. D. Steill and P. B. Armentrout, *J. Phys. Chem. A*, 2012, **116**(6), 1532–1541.
37 F. Weigend and R. Ahlrichs, *Phys. Chem. Chem. Phys.*, 2005, **7**(18), 3297–3305.
38 M. J. S. Dewar, E. G. Zoebisch, E. F. Healy and J. J. P. Stewart, *J. Am. Chem. Soc.*, 1985, **107**(13), 3902–3909.
39 T. Yanai, D. P. Tew and N. C. Handy, *Chem. Phys. Lett.*, 2004, **393**(1–3), 51–57.
40 J. F. Stanton and R. J. Bartlett, *J. Chem. Phys.*, 1993, **98**(9), 7029–7039.
41 B. Bellina, R. Antoine, M. Broyer, L. Gell, Z. Sanader, R. Mitric, V. Bonacic-Koutecky and P. Dugourd, *Dalton Trans.*, 2013, **42**(23), 8328–8333.
42 G. N. Khairallah and R. A. J. O'Hair, *Angew. Chem., Int. Ed.*, 2005, **44**(5), 728–731.
43 T. Tabarin, R. Antoine, M. Broyer and P. Dugourd, *Eur. Phys. J. D*, 2006, **37**(2), 237–239.
44 Y. Antoku, J.-i. Hotta, H. Mizuno, R. M. Dickson, J. Hofkens and T. Vosch, *Photochem. Photobiol. Sci.*, 2010, **9**(5), 716–721.
45 R. E. Palmer and C. Leung, *Trends Biotechnol.*, 2007, **25**(2), 48–55.

Chapter 4

Tuning Ag$_{29}$ nanocluster light emission from red to blue with one and two-photon excitation

Tuning Ag$_{29}$ nanocluster light emission from red to blue with one and two-photon excitation†

Isabelle Russier-Antoine,[a] Franck Bertorelle,[a] Ramzi Hamouda,[a] Driss Rayane,[a] Philippe Dugourd,[a] Željka Sanader,[b,c] Vlasta Bonačić-Koutecký,[b,d] Pierre-François Brevet[a] and Rodolphe Antoine*[a]

We demonstrate that the tuning of the light emission from red to blue in dihydrolipoic acid (DHLA) capped Ag$_{29}$ nanoclusters can be trigged with one and two photon excitations. The cluster stoichiometry was determined with mass spectrometry and found to be Ag$_{29}$(DHLA)$_{12}$. In a detailed optical investigation, we show that these silver nanoclusters exhibit a strong red photoluminescence visible to the naked eye and characterized by a quantum yield of nearly ~2% upon one-photon excitation. In the nonlinear optical (NLO) study of the properties of the clusters, the two-photon excited fluorescence spectra were recorded and their first hyperpolarizability obtained. The two-photon absorption cross-section at ~800 nm for Ag$_{29}$(DHLA)$_{12}$ is higher than 10^4 GM and the hyperpolarizability is 106×10^{-30} esu at the same excitation wavelength. The two-photon excited fluorescence spectrum appears strongly blue-shifted as compared to the one-photon excited spectrum, displaying a broad band between 400 and 700 nm. The density functional theory (DFT) provides insight into the structural and electronic properties of Ag$_{29}$(DHLA)$_{12}$ as well as into interplay between metallic subunit or core and ligands which is responsible for unique optical properties.

Introduction

Atomically precise silver nanoclusters (Ag NCs) have emerged as fascinating fluorescent nanomaterials and attracted considerable research interest in both fundamental research and practical applications, including biosensing,[1] bioimaging,[2] catalysis,[3] or photonics.[4] Due to enhanced quantum confinement, in particular, they exhibit new optical properties which are observed neither in molecules nor in bulk metals.[5] Remarkable progress has been reported over recent years in their synthesis or applications (for recent reviews, see for example ref. 6–8). In particu-

lar, the synthetic route using templates to stabilize low nuclearity silver clusters is one of the most promising. Different scaffolds used as stabilizers for silver nanoclusters have been proposed, including dendrimers,[9] DNA oligomers,[10] cryogenic noble gas matrixes,[11] or inorganic glasses.[12]

Ligands containing thiol groups are good candidates to stabilize silver NCs due to the high energy of the sulfur–silver bond. Kitaev and co-workers[13,14] have initiated this field using chiral thiols to build these silver clusters. More recently, Bigioni and co-workers,[15] Heiz and coworkers[16] and our group[17] have reported the synthesis of glutathione stabilized magic-number silver cluster compounds. Interestingly, Roy *et al.*[18] have reported for these clusters with different size blue, green and red emission through a mere temperature or silver salt concentration change during synthesis. These highly fluorescent properties[17–20] were however counterbalanced by polydispersity, uncharacterization or poor photo-stability. Another thiolated ligand, namely dihydrolipoic acid (DHLA), also leads to highly fluorescent silver clusters, emitting in the red part of the optical spectrum and having a long period stability.[19,21] Nonetheless, the preparation of sized silver quantum clusters with different wavelength range fluorescence emission using the same synthesis conditions like solvent, silver salt precursor, stabilizing ligand or reducing agent remains a challenging issue.

While progresses aiming at producing silver clusters with attractive features including brightness, tunability and photostability have been made recently, nonlinear optics may be an

[a]Institut Lumière Matière, UMR CNRS 5306 and Université Claude Bernard Lyon 1, Université de Lyon, 69622 Villeurbanne cedex, France. E-mail: rodolphe.antoine@univ-lyon1.fr
[b]Center of excellence for Science and Technology-Integration of Mediterranean region (STIM) at Interdisciplinary Center for Advanced Sciences and Technology (ICAST), University of Split, Meštrovićevošetalište 45, HR-2100 Split, Republic of Croatia
[c]Faculty of Science, University of Split, Teslina 12, HR-2100 Split, Republic of Croatia
[d]Department of Chemistry, Humboldt Universitatzu Berlin, Brook-Taylor-Strasse 2, 12489 Berlin, Germany

†Electronic supplementary information (ESI) available: CID spectrum of Ag$_{29}$(DHLA)$_{12}$, spectroscopic characterization of the synthesized Ag clusters, lifetime measurements of silver cluster, schematic diagram showing the excited state relaxation dynamics, HRS intensity *versus* wavelength for Ag$_{29}$(DHLA)$_{12}$, DFT optimized structures and TDDFT calculated one photon absorption spectra of Ag$_{29}$(DHLA)$_{12}$, Leading excitations for transition for prototype structures two-photon cross section for Ag$_{29}$(DHLA)$_{12}$ at different wavelengths and optimal setting for the ESI-MS. See DOI: 10.1039/c5nr08122j

alternative route to tunability. Indeed, the different selection rules of one-photon and two-photon excitations may provide contrasted radiative properties due to the different excited states involved. In their pioneering work, Dickson et al. have thus shown that two-photon excited fluorescence (TPEF) spectra of oligonucleotide-encapsulated silver clusters were blue-shifted with respect to the corresponding one-photon excited fluorescence (OPEF) ones, indicating that with TPEF, higher excited electronic states different than those reached by OPEF were involved.[22] Also, Polavarapu et al.[23] have successfully demonstrated that water soluble glutathione capped small gold clusters can be used for live cell imaging with both OPEF and TPEF. On our side, we have recently reported enhanced two-photon absorption cross sections and first hyperpolarizabilities for protected Au_{15} and Au_{25} clusters.[24] Theoretical attempts to reproduce enhanced TPA cross-sections and first hyperpolarizabilities of thiolated-protected gold clusters were also recently reported.[25,26]

In this work, we investigate the nonlinear optical (NLO) properties of DHLA capped 29 atom silver clusters upon two-photon excitation. We have thus determined the two-photon excited fluorescence spectra and the first hyperpolarizability for these clusters. We then show that the tuning of the fluorescence emission from the red to the blue side of the optical spectrum can be triggered by a one or a two-photon excitation.

Results and discussion

Synthesis and characterization

The silver clusters synthesis is based on the method already published by Adhikari et al.[19] However, this synthesis led to highly sodated silver clusters[21] preventing the easy assignment of their composition by mass spectrometry. Therefore, in order to obtain mass spectra without sodium adducts, $NaBH_4$ and NaOH were replaced with tetramethylammonium borohydride ($TMABH_4$) and NH_4OH respectively (see Materials and methods section). The solution of the as-prepared silver clusters has an orange color. The size of the prepared silver clusters was assigned using ESI-mass spectrometry, a particularly useful technique in the case of silver clusters due to their unequivocal isotopic pattern. An ESI mass spectrum of the as-prepared DHLA protected silver clusters acquired under gentle ESI conditions is shown in Fig. 1 (see Table ST1 in ESI† for the optimal parameters for gentle ionization conditions of ESI-MS). A charge state distribution was observed ranging from $[M - 2H]^{2-}$ to $[M - 5H]^{5-}$ along with peaks at lower masses corresponding to the neutral loss of 208 Da. The ESI spectra in the inset of Fig. 1 show the isotopic resolution for the 3- charge state. The measured mass distribution is compared with a simulated isotopic distribution of the $[Ag_{29}(DHLA)_{12} - 3H]^{3-}$ cluster. The agreement between the experimental and simulated distributions is found to be good. The observation reported here for the Ag_{29} clusters is different from the assignment previously reported for the Ag to Ag_5 and $[Ag_{25}(DHLA)_{14} - xH + xNa]$ clusters.[19,21] Different solvent com-
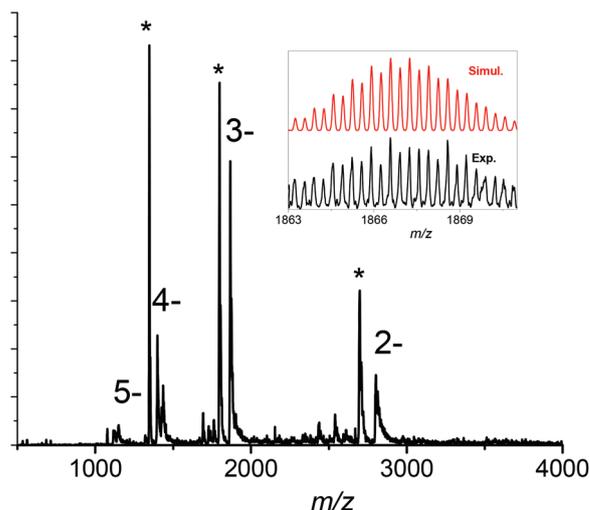

Fig. 1 ESI mass spectrum of the synthesized Ag clusters. Right inset: comparison of the experimental and simulated isotopic distributions for the 3- charge state of the Ag clusters ($[Ag_{29}(DHLA)_{12} - 3H]^{3-}$). The asterisk corresponds to peaks assigned to the loss of one DHLA molecule from the Ag clusters (see text for details).

position and different reducing agents may give different stoichiometry of Ag nanoclusters as those reported in ref. 21. Note that single DHLA ligand can be bound to more than one Ag atom and the core of several Ag atoms can be formed as discussed below. Interestingly, using bidentate ligands like 1,3-benzenedithiol (BDT) in conjunction with triphenylphosphine (TPP), a tetravalent $Ag_{29}(BDT)_{12}(TPP)_4$ nanocluster can be synthesised, readily assembling to form well-defined macroscopic crystals enabling its structure determination.[27]

The peaks relative intensity corresponding to the neutral loss of 208 Da was found to strongly depend on the ESI source parameters and ionic train voltages. This suggests that these ions arise from the $[Ag_{29}(DHLA)_{12} - 3H]^{3-}$ fragmentation. To validate this hypothesis, we performed collision-induced dissociations in the ion trap. Fig. S1† shows the CID spectrum of the $[Ag_{29}(DHLA)_{12} - 3H]^{3-}$ cluster. The observed 208 Da intense loss is attributed to the loss of one DHLA ligand molecule ($C_8H_{16}O_2S_2$). Note also that CID pathways for liganded clusters involve the formation of $Ag_n(DHLA)_m$ cluster ion products, see Fig. S1 in ESI.† The stoichiometry observed here is different from the one reported for gluthatione-protected gold clusters and may be attributed to the fact the DHLA possesses two sulphur atoms leading to different staple motifs as discussed below.

Linear optical properties

The optical properties of the DHLA protected Ag clusters were characterized by absorption spectroscopy in the UV-visible-NIR range. The absorption spectrum, shown in Fig. 2, shows several sharp transition bands with maxima at 328, 428 and 499 nm combined with a shallow absorbance onset around 600 nm. Photoluminescence excitation spectra of dilute silver nanocluster colloidal solutions at room temperature are also
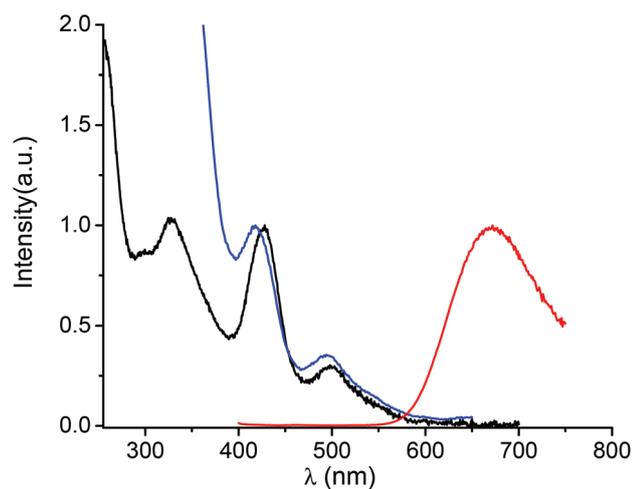
Paper

Fig. 2 Spectroscopic characterization of the synthesized Ag clusters dispersed in water. Absorption spectrum (black), fluorescence spectrum (red) with excitation at 385 nm and photoluminescence excitation spectrum (blue) with emission at 670 nm.

Fig. 3 Two-photon excited fluorescence spectra for Ag clusters as a function of wavelength for the two excitation wavelengths of 790 nm and 950 nm.

presented in Fig. 2. The photoluminescence spectra show emission maxima at ~670 nm upon excitation at 385 nm. No significant change in the emission maximum was observed when changing the excitation wavelength (from 385 nm to 500 nm), see Fig. S2 in ESI.† The luminescence quantum yield was measured to be 2 ± 1% using Nile Blue as the reference dye (see the Materials and methods section for details). In order to have a better understanding of the excited-state dynamics, we performed picosecond time-resolved fluorescence decay measurements for silver clusters. Results are given in Fig. S3 in ESI.† The decay curve can be fitted by a triple exponential curve, with a long decay time of 951 ns. Light emission through ligand-to-metal or ligand-to-metal-metal charge transfer (LMCT/LMMCT) always shows a long fluorescence lifetime, partly because the LMCT/LMMCT can affect the excited state relaxation dynamics. Therefore, the observed emission is thought to arise from Ag(I) states on the nanocluster surface. These Ag(I) states may be present as Ag(I)–thiolate complexes capping a Ag(0) core, a structural feature that has been found for thiolated gold nanoclusters.[28] The linear optical properties reported here are similar to those presented in ref. 19 and 21.

Nonlinear optical properties

TPEF spectra with excitation at 790 nm and 950 nm were recorded for the $Ag_{29}(DHLA)_{12}$ clusters, see Fig. 3. A broad band in the visible range, between 400 and 650 nm, is observed upon excitation at 790 nm whereas for an excitation at 950 nm, the TPEF spectrum is red shifted between 550 and 750 nm. These TPEF spectra drastically contrast with their linear OPEF counterpart where emission in the red only, between 550 and 750 nm is observed, see Fig. 2. The latter OPEF spectrum closely resembles the TPEF one with excitation at 950 nm. However, it is clearly observed that a tuning of the
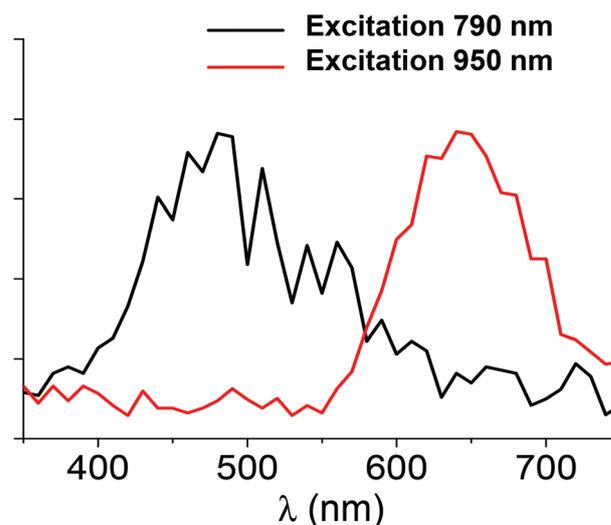
emission from red to blue can be trigged by the appropriate choice of the excitation, either a one photon excitation or a two photon excitation with 790 nm light. Such a difference between the emission resulting from one or two photon absorption has already been reported by Dickson et al.[22] for DNA-protected silver clusters and organic dyes.[29] The relative transition strengths for OPEF and TPEF are indeed highly symmetry dependent because they do not obey the same transition rules. Interestingly, the TPEF spectrum upon excitation at 950 nm is strongly red-shifted and compares well with the one reported upon excitation at 790 nm, see Fig. 3. Upon excitation at 950 nm for the TPEF spectrum and 426 or 498 nm for the OPEF one, both emission spectra appear similar, see Fig. S2 in ESI.† The difference observed between the OPEF and TPEF spectra may therefore be accounted for by the different symmetry rules required for the metal-to-metal excitations within the silver cluster core and the LMCT/LMMCT excitations as shown in the excitation pathway scheme given in Fig. S4 of the ESI.†

We attempted to determine the two-photon absorption and emission cross-sections for these $Ag_{29}(DHLA)_{12}$ nanoclusters, using the methods reported in our previous work.[24] Experimentally, we found that the TPEF cross-section for a 790 nm excitation is 0.5 GM and the TPA cross-section 12 930 GM. These experimental cross-sections point to a quantum yield (QY = $\sigma_{TPE}/\sigma_{TPA}$) for $Ag_{29}(DHLA)_{12}$ nanoclusters of about 4 × 10^{-5}, see Table ST2 in ESI† for the experimental cross-sections at different wavelengths. As already observed for gold nanoclusters, silver protected clusters are excellent two-photon absorbers but present a limited two-photon emission cross section due to a rather low quantum yield. Nevertheless, the two photon quantum yield is about two orders of magnitude higher for silver clusters than for the gold ones. First hyperpolarizabilities of these $Ag_{29}(DHLA)_{12}$ nanoclusters were also obtained using the hyper-Rayleigh scattering (HRS) technique.

The HRS intensity was recorded for several concentrations of the $Ag_{29}(DHLA)_{12}$ clusters dispersed in aqueous solutions, see Fig. S5 in ESI.† The first hyperpolarizability β determined for an excitation wavelength of 800 nm for the $Ag_{29}(DHLA)_{12}$ clusters is found to be 106×10^{-30} esu, close to the value reported for Au_{25} clusters, *i.e.* 128×10^{-30} esu.[24] Beside the exact number of atoms in the cluster metallic core, the ligands also participate to the rather large first hyperpolarizabilities, either directly with an intrinsic contribution or indirectly by imprinting symmetry changes on the core.

Calculated structure and absorption spectra of protected silver nanocluster

Structures of $Ag_{29}(DHLA)_{12}$ are composed from DHLA ligands in which two sulfur atoms are bound to different number of Ag atoms, such that silver cores of different sizes can be formed. In the case that the central Ag atom is present, the symmetric structure (point group T) is formed. However, in the case of the neutral species, deviation from point group T for Ag_{13} subunit occurs due to odd degenerate orbitals are not fully occupied due to odd number of electrons which do not correspond to superatom occupancy. For the structure with central Ag atom, two sulfur atoms of DHLA are bound to two and three Ag atoms respectively, forming Ag_{13} subunit related to centered icosahedral structure in which twelve Ag atoms are bound to twelve S atoms (*cf.* right side of Fig. S6†).

In contrast, if the central atom is not present, other structural class arise with higher energy. For example, the core of six Ag atoms as capped trigonal bipyramid can be formed, in which S atoms from DHLA are not bound to Ag atoms of the core. In this case, the symmetry of structure is removed. Each S atom is bound to one or two Ag atoms not belonging to the core, as illustrated on the right side of Fig. S6.† In this case the interface between the silver core and the ligand staples (S–Ag–S) contains also silver atoms forming an additional ligand shell. Similar situation occurs for structures containing two or five silver atoms as illustrated on Fig. S6.†

Search for the global minimum is very demanding and has not been yet ensured. Moreover, calculations of optical properties for systems with odd number of electrons, such as $Ag_{29}(DHLA)_{12}$ and for the structures with almost degenerate HOMO orbitals that are not fully occupied are methodologically difficult. Therefore, we have calculated absorption properties for two classes of structures: (A) containing central Ag atom and almost symmetrical Ag_{13} subunit and (B) structures with silver core of different sizes containing interface of silver atoms as described above. Comparison of TDDFT calculated absorption features for the lowest energy structure belonging to class (A) with the measured experimental absorption spectra, as shown in Fig. 4, illustrates good qualitative agreement, exhibiting characteristic absorption features between 300 and 500 nm containing pronounced maximum at 420 nm which arises due to excitations involving Ag_{13} subunit as well as ligands. Since two photons excitations can occur through resonance with the low lying one-photon excited states, resonance conditions for large TPA cross-sections can be easily ful-
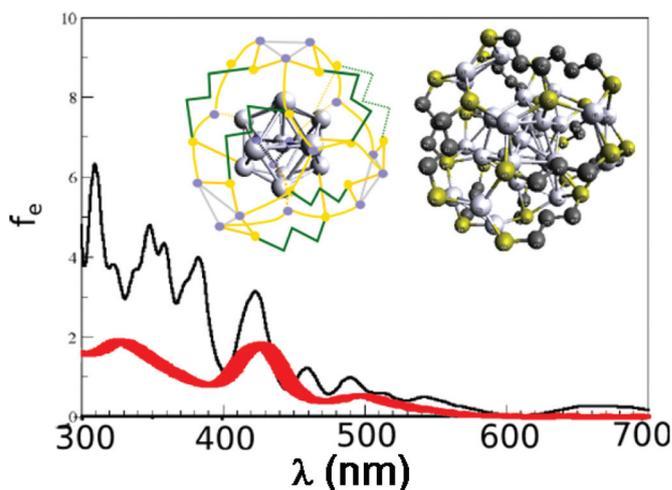

Fig. 4 Comparison of experimental (red line) and theoretical absorption spectra (black line) obtained by PAW TDDFT for optimised structure with Ag_{13} subunit (see computational for details). Right inset: DFT optimized structure of $Ag_{29}(DHLA)_{12}$. The DHLA is represented by $S-(CH_2)_3-S$ and carboxylic tail is replaced by one H atom. Silver atoms are labelled by grey balls bound to S atoms (yellow balls). Middle insert: illustrative scheme of the optimized structure shown in the right inset.

filled, as it has been experimentally found. Comparison of absorption properties for the lowest energy structure containing central Ag atom to those belonging to structural class (B) are shown on the left side of Fig. S6.† The excitations responsible for the transition close to 420 nm for both prototype of structural classes, involving silver subunit or core and ligands are shown in Fig S7.† The agreement with experimental findings is slightly better for structural class (A).

All together $Ag_{29}(DHLA)_{12}$ owns novel properties due to its electronic structure with odd number of electrons and relatively low HOMO–LUMO gap giving rise to low energy one-photon excited states which are also reachable by two-photons. This indicates that the search for liganded silver species, in which various sizes of metal core can be formed giving rise to different structural classes might lead towards design of systems with unique linear and non-linear properties useful in context of different applications.

Conclusions

Atomically size-controlled synthesis of monodispersed silver nanoclusters offers the possibility to prepare hybrid metal–organic nanoclusters with a well-defined stoichiometry. Their linear and nonlinear optical properties can then be finely compared. It appears then that the different selection rules involved for one- and two-photon excitations provide interesting radiative features in their emission spectra, notably because different excited states are accessible by one- and two-photon excitation depending on the wavelength of irradiation. We have found in particular that for the $Ag_{29}(DHLA)_{12}$

nanoclusters, the TPEF spectrum is strongly blue-shifted with 790 nm excitation as compared to the OPEF spectrum and the TPEF one with excitation at 950 nm. It displays a broad emission band between 400 and 700 nm instead of the usual emission band between 550 and 750 nm. Structural and electronic properties of $Ag_{29}(DHLA)_{12}$ nanocluster opens the route for recognizing the important role of ligands and their interface with metallic subunits for inducing unique linear and non-linear optical properties in these systems. These newly prepared bright fluorescence silver nanoclusters hold an interesting promise in the future for contrasted biolabeling, biosensing or other applications where OPEF and TPEF wavelength tuning is requested.

Materials and methods

Synthesis

Silver nitrate ($AgNO_3$), (±)-α-lipoic acid and tetramethyl-ammonium borohydride ((CH_3)$_4$NBH$_4$) were purchased from Sigma Aldrich. In a 100 ml flask, 100 mg of (±)-α-lipoic acid is dissolved in 5 ml of methanol and 10 ml of water are added followed by 2 equivalents (85 mg) of tetramethylammonium borohydride (under agitation 30 min) to reduce lipoic acid. Then, excess of reducer is eliminated by sonication (1 hour). 41 mg of silver nitrate (dissolved in 15 ml of water) is quickly added, followed by 1 ml of 10% NH_4OH solution. The solution is heated at 50 °C and 2 equivalents of tetramethylammonium borohydride are added (85 mg) and stirred. After one hour the color becomes bright orange and one equivalent of tetramethylammonium borohydride (42.5 mg) is added. After one hour, the solution is concentrated to ≈1 ml by using a rotary evaporator and transferred into a centrifuge tube. 5 ml of ethanol and 20 ml of diethyl ether are added, followed by 50 μl of glacial acetic acid. The precipitate was centrifuged 5 minutes at 9000 rpm and the supernatant subsequently removed. The precipitate is washed first with ethanol/diethyl ether and then with diethyl ether alone. The resulting brown powder is dried.

Mass spectrometry

Solutions were diluted without gel separation at a concentration of ~1 mg ml^{-1} in water, electrosprayed at a flow rate of 10 ml min^{-1} and analyzed in negative mode with a linear quadrupole ion trap mass spectrometer (LTQ, Thermo Fisher Scientific, San Jose, CA) with a spray voltage of 3 kV and a capillary temperature of 150 °C. Other instrument settings were adjusted for each species to optimize the distribution of charge states observed in the mass spectrum (see Table ST1 in ESI† for the optimal parameters for gentle ionization conditions of ESI-MS). Isotope-resolved mass spectra were recorded using the zoom scan mode of the instrument (mass resolution ~10 000, mass accuracy <0.2 Th). Collision-induced dissociation (CID) was performed using helium gas at a normalized collision energy of 20% for 30 ms.

UV/visible and fluorescence measurements

UV-vis spectra in solution were recorded using an AvaSpec-2048 fiber optic spectrometer and an AvaLight-DH-S deuterium-halogen light source. Fluorescence excitation and emission spectra and lifetime measurements were obtained using a Fluoromax-4 Horiba fluorescence spectrophotometer in the time resolved mode. Luminescence decay curves were collected with the time-correlated single-photon counting (TCSPC) extension of Fluoromax-4 using a nanoLED source at 370 nm.

Quantum yield measurement

Nile Blue dissolved in methanol (quantum yield of 0.27)[30] used as a standard and 500 nm was chosen as the excitation wavelength. The emission intensities of Nile Blue and the silver nanoclusters were integrated from 500 nm up to 850 nm. Both the excitation and the emission slit apertures were 5 mm.

HRS and TPE measurements

The light source for the HRS, TPA and TPE experiments was a mode-locked femtosecond Ti:sapphire laser delivering at the fundamental wavelength of 780 nm and 950 nm pulses with a duration of about 140 femtoseconds at a repetition rate of 76 MHz. After passing through a low-pass filter to remove any unwanted harmonic light generated prior to the cell, the fundamental beam of about 300 mW was focused by a microscope objective into a 0.5 cm spectrophotometric cell containing the aqueous solutions. The HRS and TPEF light were collected at an angle of 90° from the incident direction by a 2.5 cm focal length lens. The HRS light was separated from the excitation light by a high-pass filter and a monochromator position at the second harmonic wavelength. The HRS light was then detected with a photomultiplier tube working in the single photon counting regime. For the TPE signal, the wavelength of the spectrometer (iHR320 spectrometer) was varied between 350 nm and 750 nm.

TPA experimental arrangement

The light source for the present TPA experiments was the same as the above. The beam was gently focused by a 5 cm focal lens and sent in transmission into a 0.5 cm path length spectrophotometric cuvette. The transmitted light was detected with a large aperture photodiode. The incident power was controlled with a half-wave plate and a polarizing cube. The sample absorption, the concentration of which was set to 500 μM, was then determined as a function of the incident power. Fluorescein was used as a reference to determine the beam waist at focus in particular. The calibration of the photodiode signal was obtained with a neat water cuvette through a variation of the incident power. As expected with the neat water cuvette, the plot of the transmitted light *versus* the incident light exhibits a linear behavior whereas in the presence of the silver nanoclusters, a decrease of the transmitted intensity is observed as the absorption increases due to the nonlinear contribution.

Computational

Different level of DFT has been used to determine structural properties of $Ag_{29}(DHLA)_{12}$. For this purpose, a DFT approach with Perdew–Burke–Ernzerhof functional (PBE),[31] and resolution of identity (RI-approximation)[32] has been employed. Silver atoms were treated with Stuttgart relativistic core (RECP) potential with corresponding basis set.[33] In extensive search for the lowest energy structures within Turbomole code-package,[34] also crystal structure $Ag_{29}(BDT)_{12}(TPP)_4$[27] has served as one of the guidance routes because the search for global minimum is very difficult for this size of the system. Therefore, structural properties have been also investigated with projector augmented waves (PAW) as implemented in real-space code-package GPAW[35,36] because it is less computationally demanding. Since the both DFT methods give rise to almost identical structures, the optical absorption spectra were also calculated by using linear response TDDFT as implemented in GPAW.[37] The PAW setup was defined for atomic valence of $Ag(4d^{10}\ 5s^1)$, $S(3s^2\ 3p^2)$, $C(2s^2\ 2p^2)$ and $H(1s^1)$ with scalar relativistic effects included for Ag. The PBE exchange correlation functional was employed with real space grid spacing of 0.2 A and 0.05 eV $Å^{-1}$ convergence criteria for residual forces acting on atoms for calculation of ground state energy and structural properties. For the absorption properties, the spacing in real space grid was 0.2 Å and Gaussian broadening of 0.04 eV has been used.

References

1 V. Bonacic-Koutecky, A. Kulesza, L. Gell, R. Mitric, R. Antoine, F. Bertorelle, R. Hamouda, D. Rayane, M. Broyer, T. Tabarin and P. Dugourd, *Phys. Chem. Chem. Phys.*, 2012, **14**, 9282–9290.

2 S. Choi, R. M. Dickson and J. Yu, *Chem. Soc. Rev.*, 2012, **41**, 1867–1891.

3 W. Chen, in *Silver Nanoparticles: Synthesis, Uses and Health Concerns*, ed. I. Armentano and J. M. Kenny, Nova Science Publishers, Inc., 2013.

4 S. M. Copp, D. E. Schultz, S. Swasey and E. G. Gwinn, *ACS Nano*, 2015, **9**, 2303–2310.

5 R. C. Jin, *Nanoscale*, 2010, **2**, 343–362.

6 I. Diez and R. H. A. Ras, *Nanoscale*, 2011, **3**, 1963–1970.

7 T. Udayabhaskararao and T. Pradeep, *J. Phys. Chem. Lett.*, 2013, **4**, 1553–1564.

8 K. Zheng, X. Yuan, N. Goswami, Q. Zhang and J. Xie, *RSC Adv.*, 2014, **4**, 60581–60596.

9 J. Zheng and R. M. Dickson, *J. Am. Chem. Soc.*, 2002, **124**, 13982–13983.

10 J. T. Petty, J. Zheng, N. V. Hud and R. M. Dickson, *J. Am. Chem. Soc.*, 2004, **126**, 5207–5212.

11 W. Harbich, S. Fedrigo and J. Buttet, *Chem. Phys. Lett.*, 1992, **195**, 613–617.

12 R. Espiau de Lamaestre, H. Béa, H. Bernas, J. Belloni and J. L. Marignier, *Phys. Rev. B: Condens. Matter*, 2007, **76**, 205431.

13 N. Cathcart and V. Kitaev, *J. Phys. Chem. C*, 2010, **114**, 16010–16017.

14 N. Cathcart, P. Mistry, C. Makra, B. Pietrobon, N. Coombs, M. Jelokhani-Niaraki and V. Kitaev, *Langmuir*, 2009, **25**, 5840–5846.

15 S. Kumar, M. D. Bolan and T. P. Bigioni, *J. Am. Chem. Soc.*, 2010, **132**, 13141–13143.

16 M. Farrag, M. Tschurl and U. Heiz, *Chem. Mater.*, 2013, **25**, 862–870.

17 F. Bertorelle, R. Hamouda, D. Rayane, M. Broyer, R. Antoine, P. Dugourd, L. Gell, A. Kulesza, R. Mitric and V. Bonacic-Koutecky, *Nanoscale*, 2013, **5**, 5637–5643.

18 S. Roy, A. Baral and A. Banerjee, *ACS Appl. Mater. Interfaces*, 2014, **6**, 4050–4056.

19 B. Adhikari and A. Banerjee, *Chem. Mater.*, 2010, **22**, 4364–4371.

20 X. Le Guével, C. Spies, N. Daum, G. Jung and M. Schneider, *Nano Res.*, 2012, **5**, 379.

21 P. T. K. Chin, M. van der Linden, E. J. van Harten, A. Barendregt, M. T. M. Rood, A. J. Koster, F. W. B. van Leeuwen, C. de Mello Donega, A. J. R. Heck and A. Meijerink, *Nanotechnology*, 2013, **24**, 075703.

22 S. A. Patel, C. I. Richards, J.-C. Hsiang and R. M. Dickson, *J. Am. Chem. Soc.*, 2008, **130**, 11602–11603.

23 L. Polavarapu, M. Manna and Q.-H. Xu, *Nanoscale*, 2011, **3**, 429–434.

24 I. Russier-Antoine, F. Bertorelle, M. Vojkovic, D. Rayane, E. Salmon, C. Jonin, P. Dugourd, R. Antoine and P.-F. Brevet, *Nanoscale*, 2014, **6**, 13572–13578.

25 P. N. Day, K. A. Nguyen and R. Pachter, *J. Chem. Theory Comput.*, 2010, **6**, 2809–2821.

26 S. Knoppe, H. Häkkinen and T. Verbiest, *J. Phys. Chem. C*, 2015, **119**(49), 27676–27682.

27 L. G. AbdulHalim, M. S. Bootharaju, Q. Tang, S. Del Gobbo, R. G. AbdulHalim, M. Eddaoudi, D.-E. Jiang and O. M. Bakr, *J. Am. Chem. Soc.*, 2015, **137**, 11970–11975.

28 Z. K. Wu and R. C. Jin, *Nano Lett.*, 2010, **10**, 2568–2573.

29 C. Xu and W. W. Webb, *J. Opt. Soc. Am. B*, 1996, **13**, 481–491.

30 R. Sens and K. H. Drexhage, *J. Lumin.*, 1981, **24**, 709–712.

31 J. P. Perdew, K. Burke and M. Ernzerhof, *Phys. Rev. Lett.*, 1996, **77**, 3865–3868.

32 K. Eichkorn, O. Treutler, H. Öhm, M. Häser and R. Ahlrichs, *Chem. Phys. Lett.*, 1995, **242**, 652–660.

33 D. Andrae, U. Haeussermann, M. Dolg, H. Stoll and H. Preuss, *Theor. Chim. Acta*, 1990, **77**, 123.

34 TURBOMOLE V6.2 2010, a development of University of Karlsruhe and Forschungszentrum Karlsruhe GmbH and T. G. 1989–2007, since 2007; available from http://www.turbomole.com.

35 J. Enkovaara, C. Rostgaard, J. J. Mortensen, J. Chen, M. Dułak, L. Ferrighi, J. Gavnholt, C. Glinsvad, V. Haikola, H. A. Hansen, H. H. Kristoffersen, M. Kuisma, A. H. Larsen, L. Lehtovaara, M. Ljungberg, O. Lopez-Acevedo, P. G. Moses, J. Ojanen, T. Olsen, V. Petzold, N. A. Romero, J. Stausholm-Møller, M. Strange,

G. A. Tritsaris, M. Vanin, M. Walter, B. Hammer, H. Häkkinen, G. K. H. Madsen, R. M. Nieminen, J. K. Nørskov, M. Puska, T. T. Rantala, J. Schiøtz, K. S. Thygesen and K. W. Jacobsen, *J. Phys.: Condens. Matter*, 2010, **22**, 253202.

36 J. J. Mortensen, L. B. Hansen and K. W. Jacobsen, *Phys. Rev. B: Condens. Matter*, 2005, **71**, 035109.

37 M. Walter, H. Häkkinen, L. Lehtovaara, M. Puska, J. Enkovaara, C. Rostgaard and J. J. Mortensen, *J. Chem. Phys.*, 2008, **128**, 244101.

This journal is © The Royal Society of Chemistry 2016

Chapter 5

Two-photon absorption of ligand-protected Ag$_{15}$ nanoclusters. Towards a new class of nonlinear optics nanomaterials

COMMUNICATION

CrossMark
click for updates

Two-photon absorption of ligand-protected Ag$_{15}$ nanoclusters. Towards a new class of nonlinear optics nanomaterials†

Željka Sanader,[ab] Marjan Krstić,[a] Isabelle Russier-Antoine,[c] Franck Bertorelle,[c] Philippe Dugourd,[c] Pierre-François Brevet,[c] Rodolphe Antoine*[c] and Vlasta Bonačić-Koutecký*[ad]

We report theoretical and experimental results on two-photon absorption (TPA) cross section of thiolated small silver cluster Ag$_{15}$L$_{11}$ exhibiting extraordinary large TPA in red. Our findings provide the responsible mechanism and allow proposing new classes of nanoclusters with large TPAs which are promising for biological and medical applications.

Ligand protected noble metal clusters in the size regime smaller than ~1 nm exhibit remarkable quantum size effects.[1] In particular, their nonlinear optical (NLO) properties show extraordinary trends in the non-scalable size regime where each atom counts.[2–4] For instance, the two-photon absorption cross section for Au$_{25}$ in hexane is 427 000 GM at 800 nm, a value significantly larger than the typical value of approximately 1000 GM for organic macromolecules.[5] Also, it has been reported that water-soluble ssDNA-encapsulated Ag clusters exhibit large two-photon cross sections reaching 50 000 GM with high quantum yields in the red and near-IR part of the optical spectrum.[6] In spite of this, the elucidation of the fundamental photophysical mechanisms underlying two photon excited light emission from ligated nanoclusters with few noble metal atoms still requires an in-depth understanding of the structural and electronic interplay between the metallic and ligated parts of the clusters. The determination of the clusters structural properties is therefore the first step needed for the interpretation of the NLO experimental results. Structural properties for several ligated nanoclusters, mainly containing gold atoms, have thus been determined by single crystal X-ray crystallography.[7] Ligated clusters with 25 gold atoms have recently been reported to exhibit large two-photon absorption (TPA).[4,5] For such thiolated gold clusters [Au$_{25}$(SH)$_{18}$]$^{-1}$, which structure is known from crystallographic data,[8,9] TDDFT calculations have been used[10] to explain the large TPA cross sections that have been experimentally reported by Goodson and coworkers.[5] Calculated TPA cross sections within the three-states approximation were explained by resonance effects between one- and two-photon transitions. Besides, their values were shown to be strongly dependent on the choice of the X–C functional. Recently, one-photon absorption (OPA) properties of the smaller glutathione silver clusters (Ag$_{15}$(SG)$_{11}$)[11] as well as the OPA and the NLO properties of the 15 gold atoms clusters (Au$_{15}$SG$_{13}$)[7,11,12] exhibiting remarkable optical properties have been found. Two-photon absorption theory has been developed long time ago[13] but calculation of nonlinear properties of systems involving silver and gold subunits are more recent.[10,14,15] In this communication, we report TDDFT determined NLO properties of Ag$_{15}$L$_{11}$ (L = SH) with four confined electrons in the Ag$_8$ core. For this system, large fluorescence following OPA has been measured. Due to resonance effects, huge TPA cross sections in the red part of the spectrum are calculated while moderate TPA cross sections in the near-IR are predicted. This observation is in reasonable agreement with the measured TPA cross sections for the Ag$_{15}$(SG)$_{11}$ clusters, which are available in the range of 750–800 nm.

The two-photon absorption cross section for an excitation from the ground state $|0\rangle$ to a final state $|f\rangle$ is related to TPA transition probability for which the transition amplitude tensor has to be determined. For this purpose, we apply the quadratic response density functional theory QR-DFT using either single residue (SR) analytical formulation or *via* sum over states (SOS) method for which transition dipole moments are calculated within double residue QR method as described in Computational part, both in the framework of the DALTON quantum chemistry program.[19]

[a] *Center of excellence for Science and Technology-Integration of Mediterranean region (STIM) at Interdisciplinary Center for Advanced Sciences and Technology (ICAST), University of Split, Meštrovićevo šetalište 45, HR-21000 Split, Republic of Croatia*

[b] *Faculty of Science, University of Split, Teslina 12, HR-21000 Split, Republic of Croatia*

[c] *Institut Lumière Matière, UMR CNRS 5306 and Université Claude Bernard Lyon 1, Université de Lyon, 69622 Villeurbanne cedex, France. E-mail: rodolphe.antoine@univ-lyon1.fr*

[d] *Department of Chemistry, Humboldt Universitat zu Berlin, Brook-Taylor-Strasse 2, 12489 Berlin, Germany. E-mail: vbk@cms.hu-berlin.de*

† Electronic supplementary information (ESI) available: Analysis of transitions of one and two-photon absorption for Ag$_{15}$SH$_{11}$. Two-photon emission spectra at different pump powers for Ag$_{15}$SG$_{11}$. See DOI: 10.1039/c6cp00207b

We started with the structure of the $Ag_{15}L_{11}$ cluster (with L = SCH_3) containing an Ag_8 core which is protected by four ligands belonging to three different types.[11] In the present work, the ligand L has been further reduced to SH because the features of the one-photon absorption (OPA) spectrum remain almost unchanged.[11] Three types of ligands are present: L_1 (HS–Ag–SH), L_2 (HS–Ag–SH–Ag–SH) and L_3 type (HS–Ag–SH–Ag–SH–Ag–SH). The optimized structure of $Ag_{15}(SH)_{11}$ as well as the core with two L_1, and one L_2 and L_3 are shown in Fig. 1a.

The calculated and experimental one-photon absorption spectra of $Ag_{15}(SH)_{11}$ are given in Fig. 2. The analysis of the first four transitions (see Fig. S1 in ESI†) shows that these transitions arise from an excitation from the P-cluster-core orbital to the D-cluster-core-orbitals labelled by "core–core". S_2, S_3, S_4 transitions are located between 390 nm and 450 nm in good agreement with the position of the plateau observed in the experimental absorption spectrum (see Fig. 2).
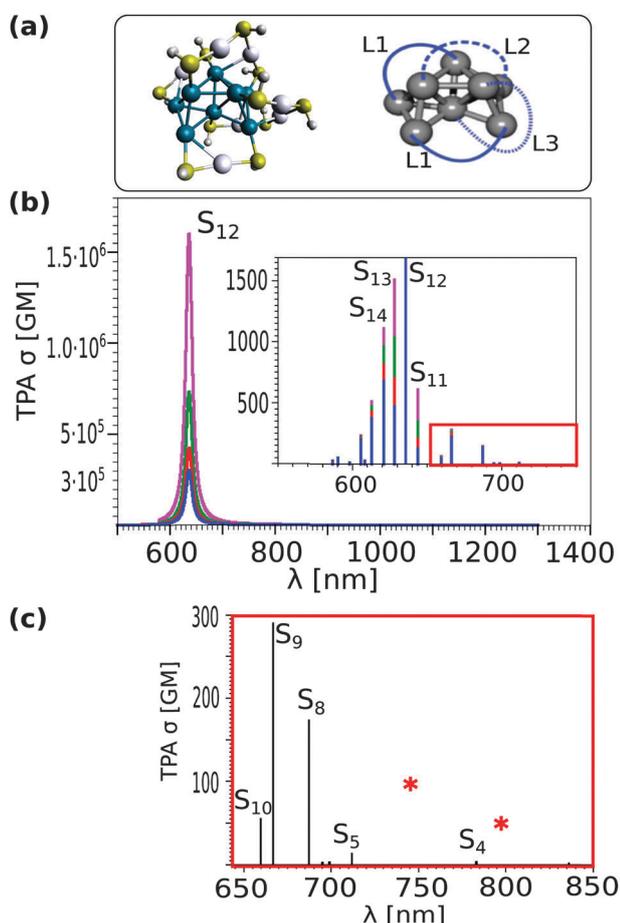

Fig. 1 (a) The lowest energy structure of $Ag_{15}L_{11}$ (with an Ag_8 core and staple ligands L_n where n is the number of Ag atoms involved in the staple motif). (b) Two-photon absorption spectrum obtained with quadratic response QR-DFT method using sum over states (SOS) approach allowing to include a damping factor for each one photon transition (Γ = 0.02, violet; Γ = 0.03, green; Γ = 0.04, red and Γ = 0.05, blue). (c) Red asterisks are experimental TPA values reported in this work for $Ag_{15}(SG)_{11}$ compared with the single residue (SR) QR-DFT calculated values presented by black sticks.
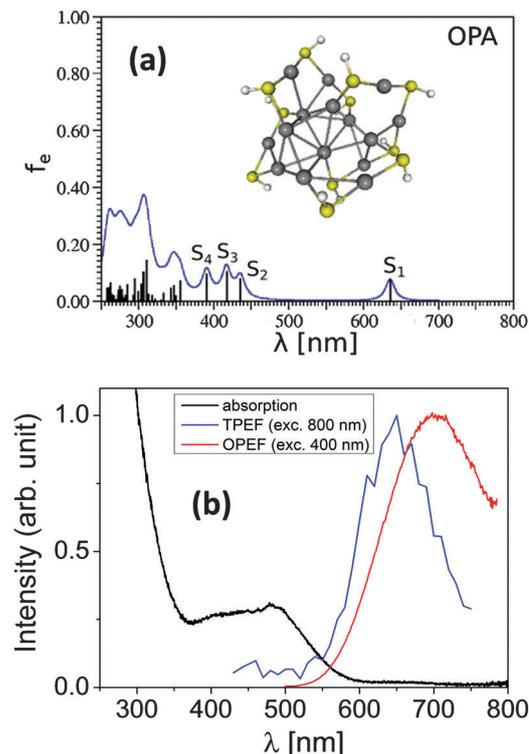

Fig. 2 (a) One-photon absorption spectrum for the lowest energy of $Ag_{15}(SH)_{11}$ obtained with TDDFT method using CAM-B3LYP functional and def2-TZVP basis set. (b) Spectroscopic characterization of the synthesized $Ag_{15}(SG)_{11}$ clusters dispersed in water. (top) Absorption (black), one photon excited (red) and two photon excited (blue) fluorescence spectra.

The two-photon absorption (TPA) spectrum for the optimized structure of $Ag_{15}L_{11}$ obtained with the quadratic response QR-DFT method using single residue (SR) (see Fig. 1c) and the sum over states (SOS) approach allowing to include a damping factor Γ for each one photon transition is presented in Fig. 1b. Notice that the values of the cross sections calculated for $\Gamma = 0$ are identical with those obtained using single residue approach. A large resonance enhancement occurs when the excitation energy of an OPA state is close to half that of a TPA state. This is nicely illustrated in Fig. 3, with S_1 (630 nm) and S_{12} (2 × 315 nm). In fact, the first excited state at 630 nm is in resonance with several states near 2 × 315 nm, resulting in an extremely large calculated TPA of over 10^6 GM (see Fig. 1b). Note that the largest contributions to the sum-over states (see eqn (1)) are $\langle S_1|\mu|S_{12}\rangle$ = 23 D and $\langle S_{13}|\mu|S_{13}\rangle$ = 4 D. Indeed, the leading excitations corresponding to large TPA cross sections involve the ligands' orbitals and not only the core's ones (see Fig. S2 in ESI†). However, the absolute value of the cross section for TPA is found to be strongly dependent on the value of the damping factor. The choice of the Γ values served to introduce corrections to TPA cross sections for more than two orders of magnitude as illustrated in Fig. 1b. For Γ = 0.05 (cf. also ref. 10) the TPA cross section σ is 300 000 GM. Indeed, the damping factor for two-photon transitions prevents the TPA cross section from blowing up near a one-photon resonance.

These results may have some features in common with π-organic molecules and in particular the stilbene derivative
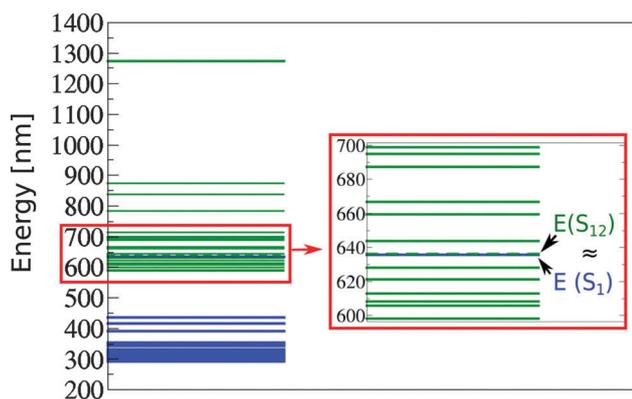
Fig. 3 Energies of one-photon OPA (blue) and two-photon TPA (green) states in nm illustrating the resonance between S_1 OPA and S_{12} TPA excited states shown on right hand side.

(BDAS) with two π-donor groups (dibutyl amino group).[16] In BDAS, one of the largest changes occurs on the nitrogens, which are located at the opposite ends of the molecule. This change, coupled with the extended distance from the molecular origin results in a large transition dipole moment for this molecule, and thus leading to TPA about 20 times larger than the one reported for the molecule without the electron donor groups. In ligand protected silver nanoclusters, the central metal core may act as reservoir of delocalized electrons and the ligand surrounding the core may act as "donor groups". Upon excitation, ligand-to-core charge transfer (LCCT) or opposite core-to-ligand charge transfer (CLCT) might occur which is reflected in large transition dipole moments which has been obtained by calculations as mentioned above.

We attempted to determine the two-photon absorption and emission cross sections for these $Ag_{15}(SG)_{11}$ nanoclusters using the method reported in our previous work.[12] Experimentally, we found that the TPEF cross section at 800 nm excitation is 0.002 ± 0.0005 GM and the TPA cross section 69 GM. These experimental cross sections point to a quantum yield (QY = $\sigma_{TPE}/\sigma_{TPA}$) for $Ag_{15}(SG)_{11}$ nanoclusters of about 2.9×10^{-5}. At 750 nm, the TPA cross section increases up to 103 GM. These experimental values are in a good agreement with the calculated cross sections in this wavelength range using single residue approach (see Fig. 1c).

Conclusions

In this communication, we report TDDFT calculations on the $Ag_{15}L_{11}$ (L = SH) clusters with four confined electrons in the Ag_8 core, for which a large one photon excited fluorescence has been observed. Due to resonance effects, huge TPA cross sections in the red part of the spectral region have been obtained within QR-TDDFT approach, while moderate TPA cross sections in near-IR have been calculated, in acceptable agreement with measured TPA cross sections of $Ag_{15}(SG)_{11}$ clusters. Exceptionally high TPA cross sections at long wavelength are expected when resonance between TPA and S_1 state of OPA occurs. The S_1 state

is dominated by a HOMO–LUMO excitation. A low HOMO–LUMO gap is found in $Ag_{15}L_{11}$, indicating that S_1 is located in the red spectral range. The leading excitations in states with large TPA cross sections always involve ligands and not just the metal core. In ligand protected silver nanoclusters, the central metal core may act as reservoir of delocalized electrons whereas the ligands surrounding the core may act as the substituted groups, similarly to the BDAS case, where it acts as a donor, albeit in a 3D spatial frame. The above findings contain the key ingredients to propose new class of nanoclusters based NLO-phores with large TPA cross sections. The basic concepts presented here open a new route to control and tune the desired NLO properties for biological molecular reporters using silver nanoclusters.

Computational

The structural and linear optical response properties corresponding to one-photon absorption (OPA) of $Ag_{15}L_{11}$ liganded clusters with L = SH have been determined using density functional theory (DFT) and its time-dependent version (TDDFT).[11,17]

For the silver atoms, the 19-e$^-$ relativistic effective core potential (19-e$^-$ RECP) from the Stuttgart group[18] taking into account scalar relativistic effects has been employed. For all atoms, triple zeta plus polarization atomic basis sets (TZVP) have been used.[18,19] The Perdew–Burke–Ernzerhof (PBE)[20] functional and Coulomb-attenuated version of Becke's three-parameter non-local exchange functional together with the Lee–Yang–Parr gradient-corrected correlation functional(CAM-B3LYP)[21] have been employed to determine the structural and OPA properties of $Ag_{15}L_{11}$, respectively.

For the two-photon absorption cross section the second order transition moments S_{ab} can be identified from the single residue of the quadratic response function (see ref. 22 and 23 and reference therein). The two-photon absorption transition matrix from the ground state $|0\rangle$ to an excited state $|f\rangle$ can be written as a sum over state expression:

$$S_{ab} = \sum_k \left[\frac{\langle 0|\hat{\mu}_a|k\rangle\langle k|\hat{\mu}_b|f\rangle}{\omega_k - \omega_f/2} + \frac{\langle 0|\hat{\mu}_b|k\rangle\langle k|\hat{\mu}_a|f\rangle}{\omega_k - \omega_f/2} \right] \quad (1)$$

where it is assumed that the frequency of the incident radiation is equal to half the excitation energy from the ground to the excited state, i.e. $\omega = \omega_f/2$. In the above equation μ_a and μ_b are the Cartesian components of the dipole moment operator μ and ω_k and ω_f are the frequencies of excitation from $|0\rangle$ to $|k\rangle$ and $|f\rangle$ respectively. In the case of linearly polarized light for an isotropic system, the two-photon absorption probability is defined as:

$$\langle \delta^{TPA} \rangle = \frac{1}{15} \sum_{ab} (S_{aa}S_{bb}^* + 2S_{ab}S_{ba}^*), \quad (2)$$

which can be converted to TPA cross section:

$$\sigma^{TPA} = \frac{(2\pi)^3 \alpha a_0^5 \omega^2}{c\pi L} \delta^{TPA} \quad (3)$$

where Lorentzian broadening with width $L = 0.1$ eV is used, α is the fine structure constant, a_0 is Bohr radius, ω is the energy of incoming photon and c is the speed of the light.[24]

Alternatively, within the sum over states (SOS) approach for the case where both photons have the same energy E_λ, orientationally averaged expressions for the two-photon matrix elements for linearly polarized photons with parallel polarization two-photon matrix elements can be formulated as:

$$|S_{f0}|^2 = \frac{4}{15} \sum_j^N \sum_k^N \left\{ \begin{array}{l} \dfrac{(\langle k|\mu|0\rangle \cdot \langle f|\mu|k\rangle)(\langle j|\mu|0\rangle \cdot \langle f|\mu|j\rangle)}{[(E_k - E_\lambda)(E_j - E_\lambda) + \Gamma^2]} \\[2ex] + \dfrac{(\langle k|\mu|0\rangle \cdot \langle j|\mu|0\rangle)(\langle f|\mu|k\rangle \cdot \langle f|\mu|j\rangle)}{[(E_k - E_\lambda)(E_j - E_\lambda) + \Gamma^2]} \\[2ex] + \dfrac{(\langle k|\mu|0\rangle \cdot \langle f|\mu|j\rangle)(\langle f|\mu|k\rangle \cdot \langle j|\mu|0\rangle)}{[(E_k - E_\lambda)(E_j - E_\lambda) + \Gamma^2]} \end{array} \right\} \tag{4}$$

The damping factor Γ for each one-photon transition serves to prevent the TPA cross section from blowing up near the one-photon resonances. For this reason, we adapted the SOS approach which requires explicit calculation of all transition dipole moments among excited states, as well as between them and the ground state which we realized in the framework of the double residue (DR) approach within DALTON program. This allowed us to adequately correct the TPA cross sections when necessary as well as to include manifold of states, usually 20 to 30 excited states avoiding "few states" model in which only the dominating terms in the two-photon absorption transition amplitude tensor are accounted for.[10] No influence of the truncation of the SOS from *e.g.* 20 to 15 states on the values of cross sections has been found. Notice that computational results should be considered as qualitative, since the influence of different functionals as well as inclusion of double excitations has not been investigated. Nevertheless, they can be used to illustrate the conceptual issues.

Experimental

Synthesis and characterization

$Ag_{15}(SG)_{11}$ nanoclusters were formed by reducing silver nitrate in the presence of excess glutathione, using a method that was similar to a previously reported method.[11] For characterization, PAGE separation was carried out by using a vertical gel electrophoresis unit with a size of 0.2 cm $\times$ 20 cm $\times$ 20 cm. The separating and stacking gels were prepared by acrylamide/bis-(acrylamide) monomers with the total contents of 35 wt% (acrylamide/bis-(acrylamide) 94:6), respectively. The eluting buffer consisted of 192 mM glycine and 25 mM tris(hydroxymethylamine). The as-prepared $Ag_{15}(SG)_{11}$ clusters were dissolved in a 15% (v/v) glycerol/water solution (6 mg in 100 μl). The samples solutions were loaded onto the stacking gel (10 μl per well) and eluted for 7 h at a constant voltage mode (150 V) to achieve sufficient separation. After gel separation, our synthesis leads to a major band closely located near the "band 2" in the Bigioni synthesis.[25,26]

NLO experiments

The light source for the present two-photon absorption and emission experiments was a mode-locked femtosecond Ti:sapphire laser delivering at the fundamental wavelength of 800 nm pulses with a duration of about 140 femtoseconds at a repetition rate of 76 MHz. The beam was gently focused by a 5 cm focal length lens to a waist of 10 μm and sent in transmission into a 0.5 cm path length spectrophotometric cuvette. The transmitted light was detected with a large aperture photodiode. The incident power was controlled with a half-wave plate and a polarizing cube. The sample absorption, the concentration of which was set to 1 mM, was then determined as a function of the incident power. Such an experimental set-up is effectively a P-scan set-up. The calibration of the photodiode signal was obtained prior to the experiment by removing the cuvette and varying the incident power. The TPE light was collected at an angle of 90° from the incident direction by a 2.5 cm focal length lens. A short pass filter with a cut-off wavelength at 750 nm was placed before the monochromator to minimize the light scattering from the excitation beam (800 nm). Fig. S3 in ESI† shows the fluorescence spectra obtained after excitation at 800 nm and at different pump-powers for Ag_{15} and pump-power dependence of the fluorescence which gave a slope of ~ 2 suggesting that it is indeed a two-photon excited emission.

Note added in proof

After the submission of this paper we became aware of the recently published study, which reports a density functional theory (DFT) and time-dependent DFT (TDDFT) investigation on the linear and nonlinear optical response in silver nanoclusters.[27]

Acknowledgements

Notes and references

1 R. C. Jin, *Nanoscale*, 2010, **2**, 343–362.
2 R. Philip, P. Chantharasupawong, H. Qian, R. Jin and J. Thomas, *Nano Lett.*, 2012, **12**, 4661–4667.
3 S. Knoppe, H. Häkkinen and T. Verbiest, *J. Phys. Chem. C*, 2015, **119**, 27676–27682.
4 S. H. Yau, O. Varnavski and T. Goodson, *Acc. Chem. Res.*, 2013, **46**, 1506–1516.
5 G. Ramakrishna, O. Varnavski, J. Kim, D. Lee and T. Goodson, *J. Am. Chem. Soc.*, 2008, **130**, 5032–5033.
6 S. A. Patel, C. I. Richards, J.-C. Hsiang and R. M. Dickson, *J. Am. Chem. Soc.*, 2008, **130**, 11602–11603.
7 R. Hamouda, F. Bertorelle, D. Rayane, R. Antoine, M. Broyer and P. Dugourd, *Int. J. Mass Spectrom.*, 2013, **335**, 1–6.

8 M. W. Heaven, A. Dass, P. S. White, K. M. Holt and R. W. Murray, *J. Am. Chem. Soc.*, 2008, **130**, 3754–3755.

9 M. Zhu, C. M. Aikens, F. J. Hollander, G. C. Schatz and R. Jin, *J. Am. Chem. Soc.*, 2008, **130**, 5883–5885.

10 P. N. Day, K. A. Nguyen and R. Pachter, *J. Chem. Theory Comput.*, 2010, **6**, 2809–2821.

11 F. Bertorelle, R. Hamouda, D. Rayane, M. Broyer, R. Antoine, P. Dugourd, L. Gell, A. Kulesza, R. Mitrić and V. Bonačić-Koutecký, *Nanoscale*, 2013, **5**, 5637–5643.

12 I. Russier-Antoine, F. Bertorelle, M. Vojković, D. Rayane, E. Salmon, C. Jonin, P. Dugourd, R. Antoine and P.-F. Brevet, *Nanoscale*, 2014, **6**, 13572–13578.

13 S. H. Lin, Y. Fujimura, H. J. Neusser and E. W. Schlag, *Multiphoton spectroscopy of molecules*, Academic Press, Inc., 1984.

14 Z. Rinkevicius, J. Autschbach, A. Baev, M. Swihart, H. Ågren and P. N. Prasad, *J. Phys. Chem. A*, 2010, **114**, 7590–7594.

15 X. Li, Z. Rinkevicius and H. Ågren, *J. Chem. Theory Comput.*, 2014, **10**, 5630–5639.

16 M. Albota, D. Beljonne, J.-L. Brédas, J. E. Ehrlich, J.-Y. Fu, A. A. Heikal, S. E. Hess, T. Kogej, M. D. Levin, S. R. Marder, D. McCord-Maughon, J. W. Perry, H. Röckel, M. Rumi, G. Subramaniam, W. W. Webb, X.-L. Wu and C. Xu, *Science*, 1998, **281**, 1653–1656.

17 V. Bonačić-Koutecký, A. Kulesza, L. Gell, R. Mitrić, R. Antoine, F. Bertorelle, R. Hamouda, D. Rayane, M. Broyer, T. Tabarin and P. Dugourd, *Phys. Chem. Chem. Phys.*, 2012, **14**, 9282–9290.

18 D. Andrae, U. Haeussermann, M. Dolg, H. Stoll and H. Preuss, *Theor. Chim. Acta*, 1990, **77**, 123–141.

19 F. Weigend and R. Ahlrichs, *Phys. Chem. Chem. Phys.*, 2005, **7**, 3297–3305.

20 J. P. Perdew, K. Burke and M. Ernzerhof, *Phys. Rev. Lett.*, 1996, **77**, 3865–3868.

21 T. Yanai, D. P. Tew and N. C. Handy, *Chem. Phys. Lett.*, 2004, **393**, 51–57.

22 N. H. List, R. Zaleśny, N. A. Murugan, J. Kongsted, W. Bartkowiak and H. Ågren, *J. Chem. Theory Comput.*, 2015, **11**, 4182–4188.

23 P. Norman, *Phys. Chem. Chem. Phys.*, 2011, **13**, 20519–20535.

24 L. Frediani, Z. Rinkevicius and H. Ågren, *J. Chem. Phys.*, 2005, **122**, 244104.

25 J. Guo, S. Kumar, M. Bolan, A. Desireddy, T. P. Bigioni and W. P. Griffith, *Anal. Chem.*, 2012, **84**, 5304–5308.

26 S. Kumar, M. D. Bolan and T. P. Bigioni, *J. Am. Chem. Soc.*, 2010, **132**, 13141–13143.

27 P. N. Day, R. Pachter, K. A. Nguyen and T. P. Bigioni, *J. Phys. Chem. A*, 2016, DOI: 10.1021/acs.jpca.5b09623.

Chapter 6

Ligand-Core NLO-phores: a combined experimental and theoretical approach of the two-photon absorption and two-photon excited emission properties of small ligated silver nanoclusters

Nanoscale

ARTICLE

Ligand-Core NLO-phores: a combined experimental and theoretical approach of the two-photon absorption and two-photon excited emission properties of small ligated silver nanoclusters

Isabelle Russier-Antoine,[a] Franck Bertorelle,[a] Željka Sanader,[b,d] Marjan Krstić,[b] Clothilde Comby-Zerbino,[a] Philippe Dugourd,[a] Pierre-François Brevet,[a] Vlasta Bonačić-Koutecký,[b,c]* and Rodolphe Antoine[a]*

We report a combined experimental and theoretical study of the two-photon absorption and excited emission properties of monodisperse ligand stabilized Ag_{11}, Ag_{15} and Ag_{31} nanoclusters in aqueous solutions. The nanoclusters were synthesized using a cyclic reduction under oxidative conditions and separated by vertical gel electrophoresis. The two-photon absorption cross-sections of these protected noble metal nanoclusters measured within the biologically attractive 750-900 nm window are several orders of magnitude larger than that reported for commercially available standard organic dyes. The two-photon excited fluorescence spectra are also presented for excitation wavelengths within the same excitation spectral window. They exhibit size-tunability. Because the fundamental photophysical mechanisms underlying these multiphoton processes in ligand protected clusters with only few metal atoms are not fully understood yet, a theoretical model is proposed to identify the key driving elements. Elements that regulate the dipole moments and the nonlinear optical properties are the nanocluster size, its structure and the charge distribution on both the metal core and the bound ligands. We coined this new class of NLO materials as « Ligand-Core » NLO-phores.

Introduction

Two-photon absorption (TPA) defined as the electronic excitation of a molecular system induced by the simultaneous absorption of a pair of photons was first proposed theoretically by M. Göppert-Mayer in 1931.[1] TPA was then only demonstrated experimentally in 1961, soon after the invention of the laser.[2] TPA is obtained with photons at a frequency half of the actual energy gap between the ground and excited states. As a result, for transitions in the visible to blue side of the optical spectrum, TPA is readily accessible with the femtosecond pulses delivered by standard femtosecond oscillators with a wavelength tunability in the 700–1300 nm range. This is therefore a definite advantage to access a deeper penetration depth into the heavily scattering biological tissue media. TPA has thus gained a widespread popularity in the biology community especially in the development of microscopy. Other applications like photodynamic therapy with in-situ photon conversion have also been recently proposed as an alternative method to the more conventional one-photon absorption (OPA)

one. Besides the deeper penetration depth of long wavelength irradiation into tissues, a gain in spatial resolution is also observed owing to the multiphoton character of the interaction of light with the medium.[3] Similarly, the technique of two-photon excited fluorescence (TPEF), that entails a TPA process in a first stage before emission of the fluorescence photon, is also gaining a widespread popularity within the same community.[4] Here, the advantages not only lie in the increased penetration depth in tissues but also in the reduced background fluorescence of the images collected.

Within this context, considerable efforts have been made to engineer molecular systems or nanoparticles with the largest TPA and TPEF cross-sections. Interestingly, it is also attractive to compare these cross-sections with their molecular first hyperpolarizability. The latter is the cross-section for the process of frequency doubling better known as Second Harmonic Generation (SHG). SHG relies on the quadratic or first hyperpolarizability whereas TPA and TPEF rely on the cubic nonlinearity or second hyperpolarizability. In the case of SHG for

instance, the standard class of molecular systems is known as the asymmetric push-pull chromophores whereas for the TPEF process it is rather customary to have centrosymmetric systems.[5-7] Push-pull chromophore systems consist of donor and acceptor end-groups connected by a charge conjugation path. The latter introduces the possibility of a large charge transfer along the conjugated molecular axis upon excitation. Recently, Ågren and collaborators have proposed a simple relationship between the metric of the charge transfer excitation Δr of a bright π-π* state, involved in the first hyperpolarizability, and the two-photon absorption cross-section for two families of push−pull π-conjugated systems.[8] The change in dipole moment upon excitation Δr can also be viewed as a measure of the average hole-electron distance upon the excitation and can therefore be used to link hyperpolarizability values to the conjugated chain length of push-pull systems. While extremely appealing as efficient chromophores, or more precisely nonlinear optical (NLO)-phores, for quadratic and cubic nonlinear processes, such push-pull systems in the form of dipolar organic dyes suffer usually from poor water solubility, severe photobleaching and high cytotoxicity. Alternatives to organic NLO-phores must therefore be sought.

Figure 1: OPEF a) and TPEF b) spectra for Ag₁₁(SG)₇, Ag₁₅(SG)₁₁ and Ag₃₁(SG)₁₉ nanoclusters with an excitation at 450 nm (OPEF) and 800 nm (TPEF).

Noble metal nanoclusters constitute another route to provide efficient linear optical (LO)-[9] and NLO-phores.[10] The search for ultra-bright emitting metal nanoclusters has been developed over the last 12 years or so using the concept of a ligand shell protected metal core. The latter core is however composed of only a few metal atoms in order to avoid developing a surface plasmon resonance.[11, 12] Different ligand shell templates have been proposed, from small organic compounds[13, 14] to larger proteins,[15] DNA[16] and dendrimers for example.[17] Such nanoclusters then display intense luminescence with large Stokes shifts and long lifetimes along with good photostability.[18] In addition, the use of peptides or proteins as templates brings a good biocompatibility and low cytotoxicity, rendering these nanoclusters highly appealing for bio-imaging applications.[19] Moreover, these nanoclusters display giant TPA cross sections in the NIR region as shown by Goodson and collaborators[20] and more recently by our groups.[21, 22] In particular, biocompatible glutathione capped gold nanoclusters are excellent one- and two-photon excited fluorescence contrast agents for live cells imaging, as proposed by Polavarapu et al.[23]

However, predicting the emission properties upon one- and two-photon excitation in these nanoclusters remains a difficult task. Radiative de-excitation pathways involving either metal-metal transitions within the metal core or ligand-to-metal and ligand-to-metal-metal charge transfer (LMCT and LMMCT respectively) transitions are rather efficient.[24, 25] It is the purpose of this contribution to propose through a combined experimental and theoretical study concepts to design ligand protected nanoclusters with large cross-sections for quadratic and cubic nonlinear processes based on the interplay between the ligand role and the non uniform delocalisation of electrons within the metal core.

In a recent communication, we have reported theoretical results on the TPA cross section of the small thiolated silver nanoclusters Ag₁₅L₁₁ where L stands for the –SH ligand. This system exhibits an extremely large TPA cross-section in the red side of the visible spectrum.[26] Such large TPA cross-sections at long wavelengths are indeed expected when a resonance between a TPA and an OPA process to the final excited state occurs. Also, the leading excitations in states yielding large TPA cross-sections always involve ligands and not just the metal core. The TPA process is accompanied with a large charge transfer upon excitation. In the present work, we have adapted our size-focusing separation method to produce glutathione (SG) ligand protected Ag₁₁, Ag₁₅ and Ag₃₁ nanoclusters. This achievement allows us to explore the size effect on the TPA and TPEF cross-sections. The size influences both the optical band gap and then resonance effects and the charge transfer effects. Both result from a change in the metal core charge distribution, including confinement of core electrons. A thorough comparison of the experimental findings with DFT and TDDFT calculations therefore allowed us to reveal the structural and electronic properties of these low nuclearity liganded silver nanoclusters constituting the new class of nonlinear nanomaterials termed "Ligand-Core" NLO-phores.
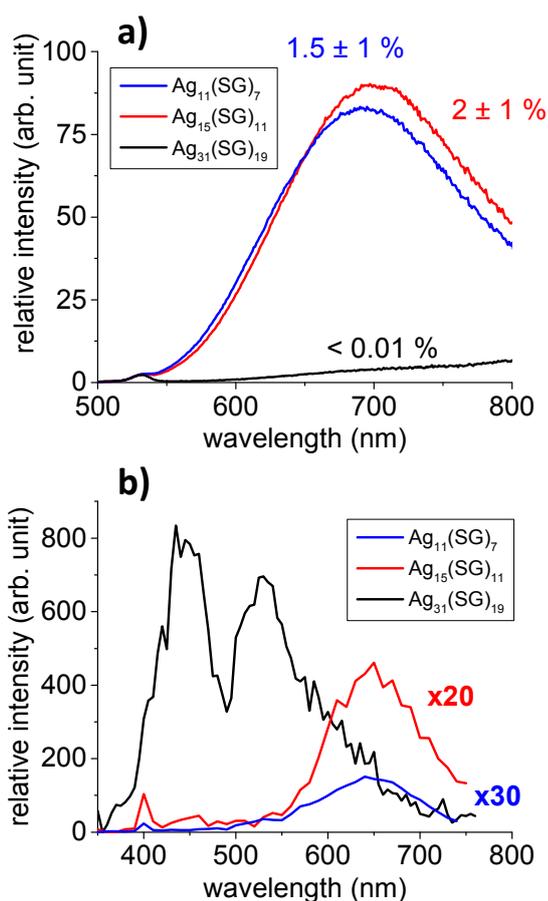
Results and discussion

Linear optical properties

Three of the smallest silver nanoclusters, previously denoted as bands 1, 2, and 6 in the synthesized mixtures obtained by Bigioni and collaborators[27] were produced in a "size-focusing" way using a cyclic reduction under oxidative conditions.[28, 29] Two of these species have been formally identified previously using electrospray-ionization (ESI) mass spectrometry (MS) as $Ag_{31}(SG)_{19}$ (band 6) and $Ag_{15}(SG)_{11}$ (band 2).[29] The smallest size (band 1) has been identified as the $Ag_{11}(SG)_7$ species in a recent work.[30] PAGE and ESI-Time-of-Flight (TOF) MS analysis on band 1 in water/methanol (50/50 v/v) are shown for this band in Fig. S1 and S2. Two charge states for $Ag_{11}(SG)_7$ were observed, namely $[M - 2H+]^{2-}$ and $[M - 3H+]^{3-}$, in the mass spectra. In addition to $Ag_{11}(SG)_7$, minor $Ag_{14}(SG)_{10}$ species along with fragmented species were also present in the ESI-MS spectra, see in Fig. S2.

Optical absorption and fluorescence spectra for the three nanocluster sizes, namely $Ag_{11}(SG)_7$, $Ag_{15}(SG)_{11}$ and $Ag_{31}(SG)_{19}$ were then recorded, as shown in Figure S3. The $Ag_{15}(SG)_{11}$ and $Ag_{11}(SG)_7$ absorption spectra are rather similar. They do not exhibit prominent features, only a monotonous increase of the absorption at wavelengths below 600 nm with a plateau between 400 and 500 nm. In contrast, the $Ag_{31}(SG)_{19}$ absorption spectrum shows a large characteristic peak centered at about 490 nm with an absorption onset near 700 nm. This band is attributed to a core-to-core excitation within the metal core, from the P-cluster-core orbital to the D-cluster-core-orbitals.[29] The fluorescence spectra for these nanoclusters were also recorded, as shown in Figure S3b. All solutions were excited at 450 nm. $Ag_{15}(SG)_{11}$ and $Ag_{11}(SG)_7$ display similar fluorescence spectra with a broad emission band centred at about 700 nm. $Ag_{11}(SG)_7$ presents though a small blue-shift of its emission band as compared to $Ag_{15}(SG)_{11}$. The quantum yields were measured to be 1.5± 1% and 2±1% for $Ag_{15}(SG)_{11}$ and $Ag_{11}(SG)_7$ respectively using DCM dye as reference. $Ag_{31}(SG)_{19}$ is found to be extremely weakly fluorescent upon one-photon excitation at 450 nm. A slowly rising onset of fluorescence appears though in the NIR region but remains very low. While the present spectra for $Ag_{15}(SG)_{11}$ and $Ag_{11}(SG)_7$ are in qualitative agreement with those reported by Bigioni and collaborators[31], they clearly disagree for band 6. Indeed, $Ag_{31}(SG)_{19}$ is here found non fluorescent whereas clusters in band 6 were previously found fluorescent in ref.[31] with a behaviour very similar to those of $Ag_{15}(SG)_{11}$ and $Ag_{11}(SG)_7$. We speculate that this discrepancy may arise from the synthesis as band 6 was previously attributed to the $Ag_{32}(SG)_{19}$ stoichiometry.[32] One may therefore argue that the Ag_{31} and Ag_{32} metal cores introduce very different absorption and fluorescence properties. Note also that two small peaks at 335 and 635 nm were reported in the Ag_{32} absorption spectra, peaks that we do not observed in our synthesis, see Figure S3.

Two-photon excited fluorescence spectra

TPEF spectra with excitation at 800 nm were recorded for the three $Ag_{11}(SG)_7$, $Ag_{15}(SG)_{11}$ and $Ag_{31}(SG)_{19}$ nanoclusters, see Figure 1. A broad band in the visible range between 400 and 650 nm with a large characteristic peak centered at about 530 nm is observed for $Ag_{31}(SG)_{19}$ whereas the TPEF spectra are red-shifted between 550 and 750 nm for $Ag_{11}(SG)_7$ and $Ag_{15}(SG)_{11}$. Also, while the TPEF and OPEF spectra are closely related for $Ag_{11}(SG)_7$ and $Ag_{15}(SG)_{11}$, the TPEF spectrum for $Ag_{31}(SG)_{19}$ is dramatically contrasted as compared to its linear OPEF counterpart where only an extremely weak emission in the NIR is observed, see Fig. 1. This $Ag_{31}(SG)_{19}$ TPEF spectrum bares though some similarity with the corresponding absorption spectrum. Figure S4 reports the same TPEF spectrum albeit with an excitation at 780 nm but no change as compared to an excitation at 800 nm are observed. Such a difference between the emission spectra resulting from one or two photon excitation has already been reported for Ag_{29} silver nanoclusters in a previously reported work.[21] One reason for this difference stems from a high symmetry dependence of the fluorescence spectra because OPEF and TPEF processes do not obey the same selection rules. The differences observed between the OPEF and TPEF spectra may therefore be accounted for by the different electronic distribution in the states involved in the metal-to-metal excitation within the silver nanocluster core and the LMCT and LMMCT excitations. We attempted to determine the TPA and TPEF cross-sections for these silver nanoclusters, using the methods reported in our previous works.[22] Experimentally, we found that the TPEF cross-sections at 800 nm excitation are 3.3×10^{-4}, 0.00169 and 0.066 GM for the $Ag_{11}(SG)_7$, $Ag_{15}(SG)_{11}$ and $Ag_{31}(SG)_{19}$ nanoclusters respectively, see Table 1. These experimental TPEF cross-sections are related to the TPA ones through the quantum yield QY, namely QY = $\sigma_{TPE}/\sigma_{TPA}$, see also Table 1. For the silver nanoclusters, this quantum yield is therefore found roughly constant at about 5×10^{-3} %. Similarly to gold nanoclusters, ligand protected silver nanoclusters are therefore excellent two-photon absorbers but present a limited two-photon emission cross-section due to a rather low quantum yield. Yet, the two photon quantum yields for these small silver nanoclusters remains about two orders of magnitude higher than that of the gold nanoclusters.

Table 1 : Two-photon cross sections and quantum yields for Ag nanoclusters excited at 800 nm.

Silver nanoclusters	TPA cross section (in GM units)	TPEF cross section (in GM units)	Two Photon QY (in %)
$Ag_{11}(SG)_7$ (band 1)	6.6	3.3×10^{-4}	4.9×10^{-3}
$Ag_{15}(SG)_{11}$ (band 2)	63.5	0.00169	2.7×10^{-3}
$Ag_{31}(SG)_{19}$ (band 6)	950	0.066	6.9×10^{-3}
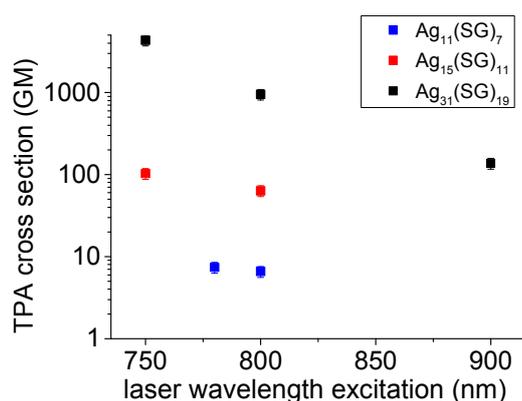
Figure 2: TPA cross sections as a function of wavelength for the Ag$_{11}$(SG)$_7$ Ag$_{15}$(SG)$_{11}$ and Ag$_{31}$(SG)$_{19}$ nanoclusters.

Two-photon absorption cross section

In parallel to the two photon excited emission properties, we also investigated the TPA cross-section as a function of the laser excitation wavelength. Figure 2 displays the cross-section for different wavelengths for the three nanocluster stoichiometries. Clearly, two trends emerge. First, the larger the nanocluster size, or more precisely the higher the number of silver atoms content, the larger is the TPA cross-section. Second, the TPA cross-section increases as the excitation wavelength shortens. Here, it must be emphasized that the TPA cross-sections are reported on a logarithmic scale. The observed effects are therefore large. TPA cross-sections derive from the imaginary part of the cubic or second hyperpolarizability. A simple three-state model, involving a ground, an intermediate and a final state was proposed to qualitatively describe the TPA cross-sections for push-pull organic dye molecules. In this model, the TPA cross-sections depend on the transition energy between the ground to the intermediate and the ground to the final state and the related transition dipole moments. The resonance effect describes the possibility to have an excitation resonant at one or two photons between the three states involved. In liganded clusters, the transition dipole moments effect is related to the geometry taken by the core metal atoms and the ligands. These two effects have been further investigated with a theoretical approach.

Structural, electronic and nonlinear optical properties of small ligand protected silver nanoclusters. Insight from theory.

Theoretical investigation of the nonlinear optical properties for the lowest energy structures of the Ag$_{11}$L$_7$, AG$_{15}$L$_{11}$ and Ag$_{31}$L$_{19}$ nanoclusters, where L stands for SCH$_3$ group, were performed. Although the ligand is different from the -SG one used in the experimental work, this study is a first step in confirming that the two effects introduced above are mainly responsible for the amplitude of the TPA, TPEF and first hyperpolarizability of these small clusters. It is obvious that the full computation involving SG ligands would be highly desirable but such a computation is not within reach at the present time due to the resources required. Time dependent density functional theory (TDDFT) calculations were thus performed for the 3 above mentioned nanoclusters. They contain 4, 8 and 12 delocalized electrons within the core as reported in Figure 3. Several factors influencing the TPA cross-sections have been identified: (*i*) the excitation between ligands and the metal core are characteristic of the nonlinear transitions, (*ii*) resonance between states involved in the OPA and TPA processes is required to obtain large TPA cross-sections, (iii) large dipole transition moments are related to nonuniform electron distribution within the metal core. The role of the structural properties, i.e. of the geometry of the metal core in determining this electron distribution, is therefore crucial.
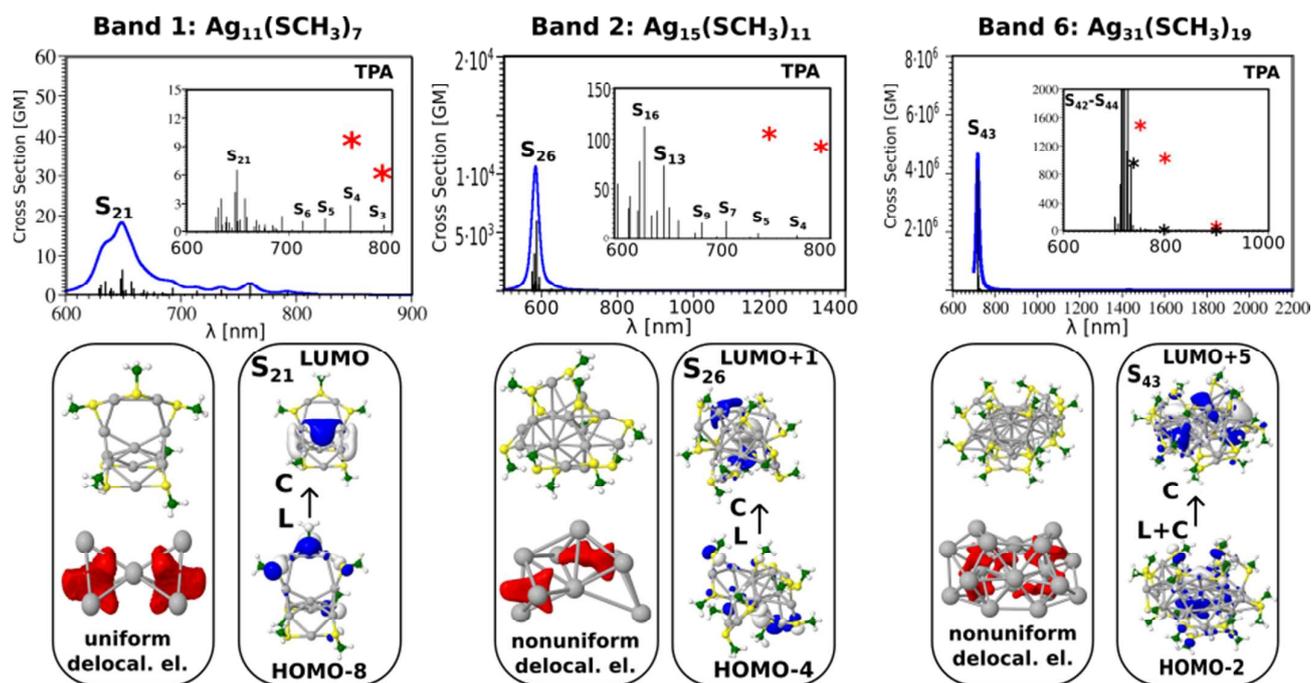
Figure 3: Comparison of TDDFT TPA spectra (Upper part) for $Ag_{11}(SCH_3)_7$, $Ag_{15}(SCH_3)_{11}$ and $Ag_{31}(SCH_3)_{19}$ nanoclusters for the lowest energy structures involving 4, 8 and 12 delocalized electrons in metal core. Red asterisks label experimental values, while black label theoretical values. Damping factor of 0.02 is used for $Ag_{15}(SCH_3)_{11}$ yielding lower TPA cross-sections values within 2 orders of magnitude. For $Ag_{31}(SCH_3)_{19}$, a three state model is used accounting for only leading transition dipole moment contributions to TPA cross section avoiding the calculation for transition dipole moments of all excited states. This allows correcting the values of TPA cross-sections for S_{43} within 4 orders of magnitude, instead of using the damping factor. Structures of the clusters together with the electron localization function (ELF) representing delocalized electrons within the core plotted for the isovalue 0.20 (Lower part). Leading excitations responsible for the large TPA cross-sections illustrating the participation of the ligands and the core are also shown in the lower part.

All the above listed factors are illustrated on Figures. 3 and 4. In the case of the $Ag_{11}L_7$ nanoclusters, resonance between the OPA process with an excited S1 state localised at a wavelength of about 450 nm (see Fig. S3) cannot be achieved considering a manifold of about 100 states within the calculation. The ELF representing delocalized electrons within the core in $Ag_{11}L_7$ nanoclusters (see fig. 3) show an electron delocalization distributed in between all core atoms. This induces low values for the transition dipole moments through LMMCT excitations. For this stoichiometry, the central metal core is formed with one central Ag atom and two symmetrical Ag_3 subunits. In contrast, for the $Ag_{15}L_{11}$ and $Ag_{31}L_{19}$ nanoclusters, the situation is strikingly different, as illustrated in Figure Fig. 3. First, there is resonance between the low lying states accessible through OPA and TPA in the spectral range around 590 nm (case of $Ag_{15}L_{11}$) and 730 nm (case of $Ag_{31}L_{19}$). Second, in both cases, the delocalised electron distributions within the core are non-uniform as shown by the electron localization function (ELF) in the lower part of the Figure. 3. This is a prerequisite for large transition dipole moments of LMMCT excitations involving ligands and the metal core. Notice, that in the case of $Ag_{15}L_{11}$ with L=SCH_3 the wavelength of the largest cross-sections is blue shifted by 56 nm with respects to previously published result for $Ag_{15}L_{11}$ with L=SH,[26] thus the structure of ligands influences

quantitatively but not qualitatively the results. Of course, an increase in the size of metal core induces a red shift of the resonance between OPA and TPA and therefore plays an important role in the context of applications where the excitation wavelength lies in the NIR window.

The influence of changing uniform to non-uniform charge distribution on the values of cross-sections is illustrated on $Ag_{11}L_7$ by introducing a positive external charge on the central Ag atom of the metal core. This pushes the electron distribution from Ag_3 group towards the central part of the core. Redistribution of electron density causes the increase of transition dipole moments through LMMCT excitations and induces an increase in TPA, as shown in Figure 4. Though, this underlines that not only the size of the core but also the structure of the metal core responsible for the distribution of the charge might be important for giving rise to large TPA.

Altogether, despite the simplification of the nanocluster ligand nature, our findings suggest that, in addition to the role of ligands as acceptors or donors, the structural properties of the core, responsible for charge distribution of the delocalized electrons, plays an important role in the design of large TPA cross-sections systems.

The experimental and theoretical values for the TPA cross-sections are in acceptable agreement considering the simplification introduced. However, the wavelengths predicted with the theoretical calculations to yield very high TPA cross-sections are not yet experimentally accessible. From the application point of view, the design of NLO-phores with large TPA cross-sections in the NIR spectral window is desirable and can be realised according to the above proposed criteria.
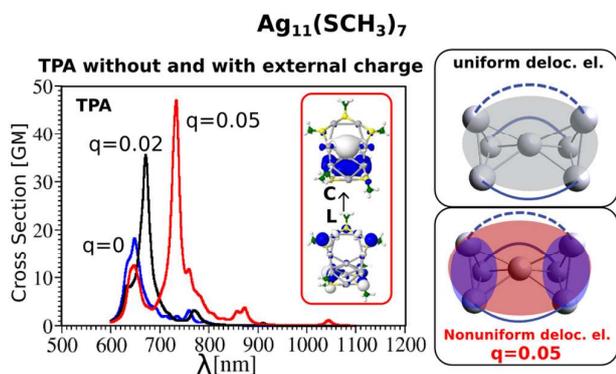

Figure 4 : Comparison of TPA spectra for $Ag_{11}(SCH_3)_7$ without and with external charge on central Ag atom illustrating an increase of transition dipole moments as well as transition from uniform delocalized electrons (q=0) to non-uniform delocalized electrons (q=0.05). Blue-positive, red-negative delocalization of electronic charge. Leading excitation from ligand to core for the considered excited state in inset. Values of maximal transition dipole moments (Debye) and cross sections (GM) for three values of external charge: q=0 are 4.2 Debye (6 GM), q=0.02 are 4.6 Debye (26 GM) and q=0.05 are 16.3 Debye (36 GM).

Concluding remarks

As already observed for Ag_{29} nanoclusters, it appears that the different selection rules involved for one- and two-photon excitations are indeed playing a critical role in determining cross-sections for TPA, TPEF and SHG processes. In the case of the TPA cross-sections which we have investigated based also on theoretical contribution, a resonance between TPA and OPA is essential. Large transition dipole moments are due to ligand-to-core or inversely core-to-ligand excitations, and are reinforce by non-uniform electronic distribution in the metal core. So large dipoles are a consequence of both the structural properties of the metal core and its size. Besides this analysis, the optical band gap decrease as the size of the silver nanoclusters increases shifting the spectra towards the NIR spectral region, a feature useful for bio-imaging applications. Altogether, understanding of leading factors governing non-linear properties of ligated small silver nanoclusters presented in this communication allows us to propose novel ligand-core NLO-phores with potential for different applications.

Materials and Methods

Experimental
Synthesis and characterization
Gluthatione protected Ag (Ag(SG)) nanoclusters were formed by reducing silver nitrate in the presence of excess glutathione, using a method that was similar to that previously reported. For band 1 ($Ag_{11}(SG)_7$) cluster synthesis : 90 mg of glutathione is dissolved in methanol (50ml) and triethylamine (3ml). Then 0.5 ml of silver trifluoroacetate solution is added (64mg/ml in methanol) under agitation and the mix is left undisturbed at 50°C overnight.
12 hours later, the mixture is cooled to -10°C and irradiated with commercial UV lamp ("black light" lamp type, λmax 365nm, 25W). 50mg (powder) of tetrabutylammonium borohydride is quickly added under agitation. After one hour, 20 mg (powder) of tetrabutylammonium borohydride is added and solution is agitated one more hour. Then, clusters are precipitated (and centrifuged) by adding 0.5 ml of 1M NaOH (or KOH) solution. After being redissolved in water (≈1ml), 20 ml of methanol is added. Precipitate was centrifuged again. This cycle (dissolution/precipitation/centrifugation) is done one more time before drying powder under vacuum.
For characterization, PAGE separation was carried out by using a vertical gel electrophoresis unit with a size of 0.2 cm × 20 cm × 20 cm. The separating and stacking gels were prepared by acrylamide/bis-(acrylamide) monomers with the total contents of 35 wt% (acrylamide/bis-(acrylamide) 94[thin space (1/6-em)]:[thin space (1/6-em)]6), respectively. The eluting buffer consisted of 192 mM glycine and 25 mM tris(hydroxymethylamine). The as-prepared Ag(SG) clusters were dissolved in a 15% (v/v) glycerol/water solution (6 mg in 100 μl). The samples solutions were loaded onto the stacking gel (10 μl per well) and eluted for 7 h at a constant voltage (150 V) to achieve sufficient separation. After gel separation, our synthesis led to a major band closely located near the "band 1", "band 2" and "band 6" of the Bigioni synthesis.

NLO experiments
The light source for the present two-photon absorption and emission experiments was a mode-locked femtosecond Ti:sapphire laser delivering at the fundamental wavelength of 800 nm pulses with a duration of about 140 femtoseconds at a repetition rate of 76 MHz. The beam was gently focused by a 5 cm focal length lens to a waist of 10 μm and sent in transmission into a 0.5 cm path length spectrophotometric cuvette. The transmitted light was detected with a large aperture photodiode. The incident power was controlled with a half-wave plate and a polarizing cube. The sample absorption, the concentration of which was set to 1 mM, was then determined as a function of the incident power. Such an experimental set-up is effectively a P-scan set-up. The calibration of the photodiode signal was obtained prior to the experiment by removing the cuvette and varying the incident power. The TPEF light was collected at an angle of 90° from the incident direction by a 2.5 cm focal length lens. A short pass filter with a cut-off wavelength at 750 nm was placed before the monochromator to minimize the light scattering from the excitation beam at 800 nm. The laser source could be tuned around 800 nm to record similar spectra at a different excitation wavelength.

Computational.

The structural, one and two photon (OPA and TPA) absorption properties of liganded silver nanoclusters with L= SCH_3 were

determined using density functional theory (DFT), time-dependent version (TDDFT)[29,33] and quadratic response approach.

For the silver atoms, (Ag$_n$, n=10, 11, 15, 31) the 19-e- relativistic effective core potential (19-e- RECP) from the Stuttgart group[34] taking into account scalar relativistic effects has been employed. For all atoms, triple zeta plus polarisation atomic basis sets (TZVP) have been used.[34, 35] The Perdew–Burke–Ernzerhof (PBE)[36] functional and Coulomb-attenuated version of Becke's three-parameter non-local exchange functional together with the Lee–Yang–Parr gradient-corrected correlation functional (CAM-B3LYP)[37] have been employed to determine the structural and optical properties.

For the calculation of TPA the cross section (σ)[38], the two-photon absorption probability (DELTA) is needed which can be obtained from two-photon absorption transition matrices from the ground to the excited state using either single residue[8, 39] or double residue quadratic response procedure. In the latter case, the sum-over-states (SOS) approach can be used which contains also the dumping factor Γ serving to prevent the TPA cross-sections from blowing up near the one-photon resonances. This allowed to adequately correct the TPA cross-sections when necessary as well as to include manifold of states, usually 20 to 30 excited states. In some cases "few states" model as a simplified version in which only the dominating terms in the two-photon absorption transition amplitude tensor are accounted for was used[40]. For calculations the DALTON[41, 42] program and its modified version was used.

Notes

[a]Univ Lyon, Université Claude Bernard Lyon 1, CNRS, Institut Lumière Matière, F-69622, LYON, France

[b]Center of excellence for Science and Technology-Integration of Mediterranean region (STIM) at Interdisciplinary Center for Advanced Sciences and Technology (ICAST), University of Split, Meštrovićevošetalište 45, HR-2100 Split, Republic of Croatia

[c]Department of Chemistry, Humboldt Universitatzu Berlin, Brook-Taylor-Strasse 2, 12489 Berlin, Germany

[d]Faculty of Science, University of Split, Teslina 12, HR-2100 Split, Republic of Croatia

References

1. M. Göppert-Mayer, *Ann. Phys.*, 1931, 401, 273-294.
2. W. Kaiser and C. G. B. Garrett, *Phys. Rev. Lett.*, 1961, 7, 229.
3. A. V. Kachynski, PlissA, A. N. Kuzmin, T. Y. Ohulchanskyy, BaevA, QuJ and P. N. Prasad, *Nat Photon*, 2014, 8, 455-461.
4. W. Denk, J. Strickler and W. Webb, *Science*, 1990, 248, 73-76.
5. C. Barsu, R. Cheaib, S. Chambert, Y. Queneau, O. Maury, D. Cottet, H. Wege, J. Douady, Y. Bretonniere and C. Andraud, *Org. Biomol. Chem.*, 2010, 8, 142-150.
6. F. Terenziani, C. Katan, E. Badaeva, S. Tretiak and M. Blanchard-Desce, *Adv. Mater. (Weinheim, Ger.)*, 2008, 20, 4641-4678.
7. M. Kivala and F. Diederich, *Acc. Chem. Res.*, 2009, 42, 235-248.
8. N. H. List, R. Zaleśny, N. A. Murugan, J. Kongsted, W. Bartkowiak and H. Ågren, *J. Chem. Theor. Comp.*, 2015, 11, 4182-4188.
9. R. Jin, *Nanoscale*, 2015, 7, 1549-1565.
10. S. H. Yau, O. Varnavski and T. Goodson, *Acc. Chem. Res.*, 2013, 46, 1506-1516.
11. L.-Y. Chen, C.-W. Wang, Z. Yuan and H.-T. Chang, *Anal. Chem.*, 2015, 87, 216-229.
12. I. Diez and R. H. A. Ras, *Nanoscale*, 2011, 3, 1963-1970.
13. J. Akola, M. Walter, R. L. Whetten, H. Hakkinen and H. Gronbeck, *J. Am. Chem. Soc.*, 2008, 130, 3756-+.
14. M. Zhu, C. M. Aikens, F. J. Hollander, G. C. Schatz and R. Jin, *J. Am. Chem. Soc.*, 2008, 130, 5883-5885.
15. J. Xie, Y. Zheng and J. Y. Ying, *J. Am. Chem. Soc.*, 2009, 131, 888-+.
16. J. T. Petty, J. Zheng, N. V. Hud and R. M. Dickson, *J. Am. Chem. Soc.*, 2004, 126, 5207-5212.
17. J. Zheng and R. M. Dickson, *J. Am. Chem. Soc.*, 2002, 124, 13982-13983.
18. X.-R. Song, N. Goswami, H.-H. Yang and J. Xie, *Analyst*, 2016, 141, 3126-3140.
19. X. Qu, Y. Li, L. Li, Y. Wang, J. Liang and J. Liang, *J. Nanomat.*, 2015, 2015, 23.
20. G. Ramakrishna, O. Varnavski, J. Kim, D. Lee and T. Goodson, *J. Am. Chem. Soc.*, 2008, 130, 5032-5033.
21. I. Russier-Antoine, F. Bertorelle, R. Hamouda, D. Rayane, P. Dugourd, Z. Sanader, V. Bonacic-Koutecky, P.-F. Brevet and R. Antoine, *Nanoscale*, 2016, 8, 2892-2898.
22. I. Russier-Antoine, F. Bertorelle, M. Vojkovic, D. Rayane, E. Salmon, C. Jonin, P. Dugourd, R. Antoine and P.-F. Brevet, *Nanoscale*, 2014, 6, 13572-13578.
23. L. Polavarapu, M. Manna and Q.-H. Xu, *Nanoscale*, 2011, 3, 429-434.
24. K. G. Stamplecoskie and P. V. Kamat, *J. Am. Chem. Soc.*, 2014, 136, 11093-11099.
25. K. G. Stamplecoskie, Y.-S. Chen and P. V. Kamat, *J. Phys. Chem. C*, 2014, 118, 1370-1376.
26. Z. Sanader, M. Krstic, I. Russier-Antoine, F. Bertorelle, P. Dugourd, P.-F. Brevet, R. Antoine and V. Bonacic-Koutecky, *Phys. Chem. Chem. Phys.*, 2016, 18, 12404-12408.
27. S. Kumar, M. D. Bolan and T. P. Bigioni, *J. Am. Chem. Soc.*, 2010, 132, 13141-13143.
28. N. Cathcart, P. Mistry, C. Makra, B. Pietrobon, N. Coombs, M. Jelokhani-Niaraki and V. Kitaev, *Langmuir*, 2009, 25, 5840-5846.
29. F. Bertorelle, R. Hamouda, D. Rayane, M. Broyer, R. Antoine, P. Dugourd, L. Gell, A. Kulesza, R. Mitric and V. Bonacic-Koutecky, *Nanoscale*, 2013, 5, 5637-5643.
30. A. Baksi, M. S. Bootharaju, X. Chen, H. Häkkinen and T. Pradeep, *J. Phys. Chem. C*, 2014, 118, 21722-21729.
31. B. A. Ashenfelter, A. Desireddy, S. H. Yau, T. Goodson and T. P. Bigioni, *J. Phys. Chem. C*, 2015, 119, 20728-20734.
32. J. Guo, S. Kumar, M. Bolan, A. Desireddy, T. P. Bigioni and W. P. Griffith, *Anal. Chem.*, 2012, 84, 5304-5308.
33. V. Bonacic-Koutecky, A. Kulesza, L. Gell, R. Mitric, R. Antoine, F. Bertorelle, R. Hamouda, D. Rayane, M. Broyer, T. Tabarin and P. Dugourd, *Phys. Chem. Chem. Phys.*, 2012, 14, 9282-9290.
34. D. Andrae, U. Haeussermann, M. Dolg, H. Stoll and H. Preuss, *Theor. Chim. Acta*, 1990, 77, 123.
35. F. Weigend and R. Ahlrichs, *Phys. Chem. Chem. Phys.*, 2005, 7, 3297.
36. J. P. Perdew, K. Burke and M. Ernzerhof, *Phys Rev Lett.*, 1996, 77, 3865-3868.
37. T. Yanai, D. P. Tew and N. C. Handy, *Chem. Phys. Lett.*, 2004, 393, 51-57.
38. L. Frediani, Z. Rinkevicius and H. Ågren, *J. Chem. Phys.*, 2005, 122, 244104
39. P. Norman, *Phys Chem Chem Phys.*, 2011, 13, 20519-20535.
40. P. N. Day, K. A. Nguyen and R. Pachter, *J. Chem. Theory Comput.*, 2010, 6, 2809-2821.

41.   K. Aidas, C. Angeli, K.L. Bak, V. Bakken, R. Bast, L. Boman, O. Christiansen, R. Cimiraglia, S. Coriani, P. Dahle, E.K. Dalskov, U. Ekström, T. Enevoldsen, J.J. Eriksen, P. Ettenhuber, B. Fernández, L. Ferrighi, H. Fliegl, L. Frediani, K. Hald, A. Halkier, C. Hättig, H. Heiberg, T. Helgaker, A.C. Hennum, H. Hettema, E. Hjertenæs, S. Høst, I.-M. Høyvik, M.F. Iozzi, B. Jansík, H.J.A. Jensen, D. Jonsson, P. Jørgensen, J. Kauczor, S. Kirpekar, T. Kjærgaard, W. Klopper, S. Knecht, R. Kobayashi, H. Koch, J. Kongsted, A. Krapp, K. Kristensen, A. Ligabue, O.B. Lutnæs, J.I. Melo, K.V. Mikkelsen, R.H. Myhre, C. Neiss, C.B. Nielsen, P. Norman, J. Olsen, J.M.H. Olsen, A. Osted, M.J. Packer, F. Pawlowski, T.B. Pedersen, P.F. Provasi, S. Reine, Z. Rinkevicius, T.A. Ruden, K. Ruud, V.V. Rybkin, P. Sałek, C.C.M. Samson, A.S. de Merás, T. Saue, S.P.A. Sauer, B. Schimmelpfennig, K. Sneskov, A.H. Steindal, K.O. Sylvester-Hvid, P.R. Taylor, A.M. Teale, E.I. Tellgren, D.P. Tew, A.J. Thorvaldsen, L. Thøgersen, O. Vahtras, M.A. Watson, D.J.D. Wilson, M. Ziolkowski, and H. Ågren, Wiley Interdisciplinary Reviews: Computational Molecular Science, 2014. **4**(3): p. 269-284.

42.   *Dalton, a molecular electronic structure program, Release Dalton2016.0* (2015).

CONCLUSIONS AND OUTLOOK

Investigation of unique linear and nonlinear optical properties of functionalized silver nanoclusters by biomolecules and ligands within this thesis provided an excellent insight of mutual interactions between subunits, thus offering the basis for different biosensing and imaging applications.

In this context intermolecular interactions involving aromatic rings play a significant role and therefore we first studied theoretically proprieties of aromatic rings interacting with metal ions on example of DNPH molecule. Our results show that optical properties of aromatic rings can be tuned by Ag cation induced electrochromism in DNPH due to binding to specific NO_2 groups. Our findings open new routs in two different application areas due to the fact that DNPH can easily bind to biological molecules and surface materials through carbonyl groups. In the context of biosensing, DNPH is used to probe carbonylated proteins, which upon the reaction of carbonyl groups with DNPH, can be detected and quantified spectrophotometrically. As presented in the thesis, optical properties of DNPH change depending on presence and position of charge in its environment, which can be used as marker to probe the surrounding charge (both cations and anions) of proteins. In the context of opto-electronics, DNPH in external field can be used to tune optical properties (both absorption and fluorescence) of organic materials. One example could be highly oriented DNPH monolayers on oxidized diamond electrodes. These monolayers could be produced using carbonyl groups (in analogy to carbonylated proteins) and color tuning could be performed by an applied electric field.

Our theoretical study of the nature of electronic excitations at metal-bioorganic interface illustrated on histidine-silver hybrids provided the important result that the presence of smallest silver subunit increases the intensity of low energy transition in histidine illustrating metal cluster induces enhancement of absorption of biomolecules in hybrid systems. This is due to three general types of electronic excitation at the metal inorganic interface: π–π^* excitations within bioorganic subunits, charge transfer between organic and cluster subunit and intrametallic excitation within the cluster subunit. Thus, binding of silver to histidine has profound effects on absorption of bare histidine. Comparison of calculated absorption spectra with experimental photo-fragmentation yield allows for structural assignment of measured spectroscopic patterns. Our findings may serve to establish silver-labeling as the tool for detection of histidine and histidine-tagged proteins.

Our theoretical investigations of linear and nonlinear properties of ligand protected (thiolated) small silver clusters provided the responsible mechanism for intense linear absorption (OPA) and extraordinary large two-photon absorption (TPA) allowing to propose new classes of nanoclusters with large TPAs which are promising for biosensing and medical applications. The results are based on investigation of four classes of systems including $Ag_{29}(DHLA)_{12}$, $Ag_{11}L_7$, $Ag_{15}L_{11}$ and $Ag_{31}L_{19}$ (L=SCH_3). The density functional theory provided the insight

into structural and electronic properties of ligated silver clusters as well as into interplay between metallic subunit or core and ligands, which is responsible for unique optical properties. The comparison with the experimental OPA and TPA spectra allowed to assign the structural properties to the measured features as well as to determine general conditions necessary for achievement of large TPA cross sections. These are: resonance between linear absorption states and two photon absorption states, large transition dipole moments between excited states for which nonuniform distribution of electrons within the core is desirable. Very large TPA have been calculated for $Ag_{15}L_{11}$ and $Ag_{31}L_{19}$ since these ligated clusters satisfy the above listed conditions. Analysis of the leading excitations in states with large TPA cross sections always shows the contributions of ligands and not just the metal core. The basic concepts presented here open a new route to control and tune the desired nonlinear optical (NLO) properties for biological molecular reporters using silver nanoclusters. These findings direct the search for new class of ligand-metallic core NLO-phores with large TPA cross sections.

All together, the obtained results, which have been confirmed by experimental findings, open new route for proposing new materials for biosensing and bioimaging in the future.

Appendix A

Formation and characterization of thioglycolic acid-silver cluster complexes

Formation and characterization of thioglycolic acid–silver cluster complexes

Bruno Bellina,[a] Rodolphe Antoine,[a] Michel Broyer,[a] Lars Gell,[b] Željka Sanader,[c] Roland Mitrić,[d] Vlasta Bonačić-Koutecký[b,c] and Philippe Dugourd*[a]

Gas phase reactivity observed in an ion trap was used to produce silver clusters protected with thioglycolic acid. Fragmentation pathways as well as optical properties were explored experimentally and theoretically. Sequential losses of SCH_2 and CO_2 in the ion trap lead to redox reactions with charge transfers between the metal part and the carboxylate and thiolate groups. This allows us to control the number of electrons in the metallic subunit and thus optical properties of the complexes. The presented formation process can be used as a prototype for tuning optical and chemical properties of ligated metal clusters by varying the number of confined electrons within the metallic subunit.

Introduction

The optical and electronic properties of noble metal nanoparticles and clusters have drawn considerable research interest due to possible applications in the fields of biosensing, single molecule spectroscopy and optoelectronics.[1,2] In a metal, conduction electrons are highly delocalized over large space, but in small nanoparticles and clusters, the decrease in size confines the electronic motion until separation of conduction and valence bands occurs and eventually molecular-like discrete electronic states and a nonzero HOMO–LUMO gap appear.[3–5] Their optical spectra display discrete visible or near-infrared absorption and emission bands, in contrast to optical spectra of large nanoparticles that are characterized by a broad band given by the surface plasmon resonance.[6] The order and spacing of the discrete levels depend on the structure of confinement and the number of electrons. Ligand-protected noble metal clusters are particularly attractive for applications,[3,7–10] such as optical labeling. In addition to protecting and to stabilizing the metal core, the ligands modify the dielectric constant at the surface of the metal core as well as the space in which the electrons are confined.[11] There may also be one or several electrons localized in metal–thiolate or metal–carboxylate bonds reducing the number of electrons in the metal core.[12,13] An alternative to the formation of protected clusters by wet chemistry is the synthesis of small and well defined organo-metallic cluster hybrids in gas phase. This approach was pioneered by the group of O'Hair[14–16] using gas phase sequential reactions by excitation of various precursor ions.[17]

In this paper, we study silver cluster protected with thioglycolic acid ligands in order to create species with a tunable number of electrons which are delocalized within the metal cluster subunit and we examine experimentally and theoretically their optical properties. Due to the large s–d energy gap in silver, the absorption at low energy in hybrid systems is mainly due to s-electron excitations within the silver subunit, in contrast to gold clusters where the relativistic effects responsible for the small s–d gap permit excitations of d electrons. The latter leads to optical transitions of similar intensities spread over a large energy interval while for silver a strong absorption in a narrow wavelength regime is observed.[18] Thioglycolic acid was chosen as a prototype ligand allowing for the joint experimental and theoretical investigations. It contains a thiol functional group and is soluble in water. We focus on clusters containing 3 and 4 silver atoms and use gas phase reactivity to produce species with different numbers of electrons which can be confined within the cluster subunit.

Materials and methods

Experimental

Thioglycolic acid (L = $HSCH_2COOH$) and $AgNO_3$ were purchased from Sigma Aldrich. The complexes were prepared by mixing a solution of 50 μM of $AgNO_3$ with 50 μM of thioglycolic acid in distilled water plus 2% of NH_3. Mass spectrometry and photodissociation measurements were performed using a

[a] *Institut Lumière Matière, UMR5306 Université Lyon 1-CNRS, Université de Lyon, 69622 Villeurbanne cedex, France*

[b] *Humboldt-Universität zu Berlin, Brook-Taylor-Straße 2, 12489 Berlin, Germany. E-mail: vbk@chemie.hu-berlin.de*

[c] *Center for Advanced Sciences and Technology (ICAST), University of Split, Meštrovićevo Šetalište bb., 2100 Split, Croatia*

[d] *Department of Physics, Free University Berlin, Arnimallee 14, 14195 Berlin, Germany. E-mail: philippe.dugourd@univ-lyon1.fr; Tel: +33 4 72 43 11 32*
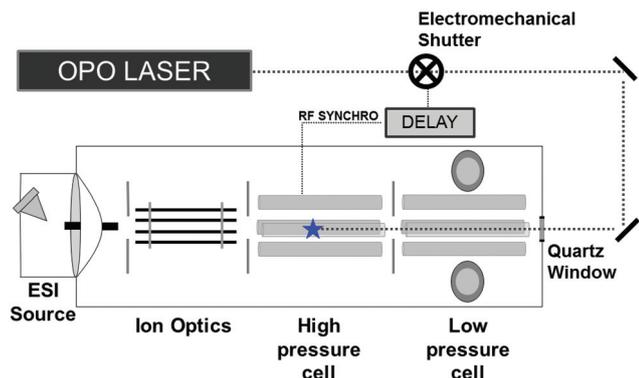
Fig. 1 Experimental set-up. Ions are irradiated in the high pressure cell.

modified LTQ Velos (Thermo electron) ion trap coupled to a tunable optical parametric oscillator (OPO) laser. Fig. 1 displays schematically the experimental set-up developed for this work. The laser is a nanosecond frequency-doubled tunable Panther™ EX OPO laser pumped by a Powerlite™ II Nd:YAG laser (both from Continuum, Santa Clara, CA, USA). The laser beam passes through two diaphragms (2 mm diameter) and lenses after which it is injected on the axis of the linear trap through a quartz window fitted on the rear of the LTQ Velos chamber. The collimation and focusing of the laser beam were optimized for maximal overlap between the laser beam and the ion cloud in the high pressure cell. It is then possible to select and excite the ions by laser and/or collision in this first linear ion trap (high pressure cell). An electromechanical shutter, electronically synchronized with the mass spectrometer, was placed along the laser beam and allowed to inject the laser light according to a given time sequence. To perform laser irradiation for a given period of time, we add in the ion trap RF sequence an MS^n step with an activation amplitude of 0%, during which the shutter located on the laser beam is opened.

The different species studied in this contribution were "synthesized" in the gas phase by successive sequences of collision induced dissociation (CID) of a silver–thioglycolic acid complex precursor (MS^n experiments). The different steps of ion selection and excitation are successively carried out in the high pressure cell. Final product ions are then transferred and mass analyzed in the low pressure cell. Photofragmentation yields at λ = 295, 355 and 440 nm were measured by irradiating ionic species for 500 ms (10 laser shots). The yield is defined as $\sigma = \ln(I0_{precursor}/(I_{precursor}))$ where $I0_{precursor}$ and $I_{precursor}$ are the intensities of the precursor ion signals recorded without and with laser irradiation.

Computational

Density functional theory (DFT) has been used to determine the structural properties of ligand-protected silver complexes employing the PBE0 functional[19] and the relativistic effective core potential (RECP) of the Stuttgart group for silver atoms.[20] The TZVP atomic orbital basis set was used for all atoms.[21] An extensive search for structures was performed using simulated

annealing coupled to molecular dynamics (MD) simulations in the frame of the semiempirical AM1 method[22] with parameters for Ag atoms. The structures identified in this way were subsequently reoptimized at the DFT level using gradient minimization techniques, and stationary points were characterized by calculating the harmonic vibrational frequencies. Notice that low-energy structures obtained by DFT techniques differ substantially from those reached by the AM1 technique, in particular for larger complexes. Therefore, in spite of extensive search for the lowest energy structures, finding of the global DFT minimum is not fully guaranteed. The absorption spectra were computed employing the long-range corrected version of the hybrid B3LYP functional using the Coulomb-attenuated method (CAM-B3LYP),[23] which provides a reliable description of charge-transfer transitions. Molecular Dynamic simulations have been performed at the DFT level in order to understand the fragmentation processes and the electron transfers. Therefore MD simulation at constant energy with an initial kinetic energy of 5 eV was applied using the PBE functional and the SVP atomic orbital basis set for all atoms. The electron localization functions (ELF)[24] have been calculated in order to analyze the nature of bonding and the distribution of excess electrons within the cluster cores.

Results

The full mass spectrum (not shown) obtained after electrospraying the solution displays intense peaks corresponding to $[nL + (n + 1)Ag - (n + 2)H]^-$ anions, which may result from the formation of $\cdots Ag\text{–}S\text{–}Ag\text{–}S\text{–}Ag\cdots$ chains. The peak corresponding to two thioglycolic acids and 3 silvers was selected and further fragmented by CID (Fig. 2). Successive losses of 44 and 46 uma are attributed to CO_2 and SCH_2 losses leading to a complex made of one thioglycolic acid and 3 silver atoms. Isolation and fragmentation of this latter complex lead also to the successive losses of 44 and 46 which corresponds to the formation of $[SCH_2 + 3Ag]^-$ and Ag_3^- ions (Fig. 2). To our knowledge, this is the first observation of the anionic Ag_3^- obtained
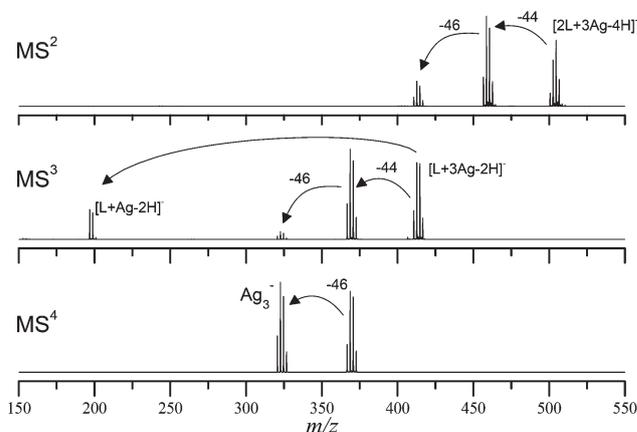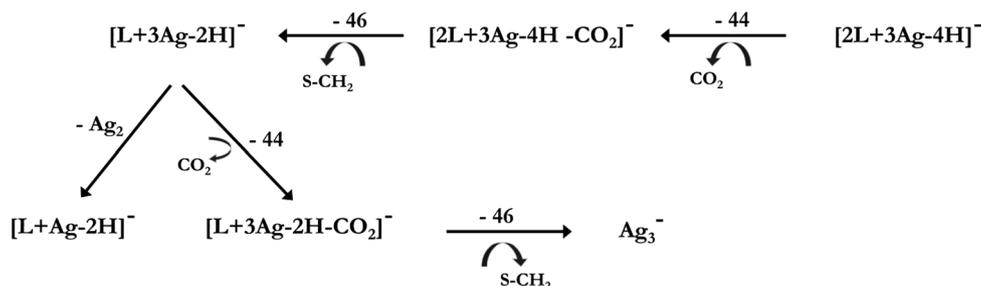

Fig. 2 MS^n spectra recorded after CID of $[2L + 3Ag - 4H]^-$.

Scheme 1

through the fragmentation of small ligated metal clusters, while the formation of the cationic species *via* ESI/CID was reported in earlier work.[14,17] A loss of a silver dimer leading to the formation of an Ag–thioglycolic acid complex is also observed. Scheme 1 summarizes the fragmentation pathways obtained from MS^n experiments. Results of MD simulations starting from the $[2L + 3Ag − 4H]^−$ complex with a kinetic energy of 5 eV are shown in Fig. 3a. The initial structure is composed of a silver trimer with one ligand on each side. The structural properties are very similar to $[Ag_3 + 2GSH − 4H]^−$ (GSH glutathione peptide)[25] although the ligand is different. After 500 fs a loss of CO_2 is observed leading to the formation of a complex in which Ag_3 is bound to $L − 2H$ on one face and SCH_2 on the other triangle face. At longer time the loss of SCH_2 is observed with the formation of the $[L + 3Ag − 2H]^−$ complex. The successive losses of CO_2 and SCH_2 observed along the MD trajectory are in full agreement with experimental findings and confirm Scheme 1. Fig. 3b shows structures and natural bond orbital (NBO) charges corresponding to the different equilibrium and transition state structures as well as their relative energies during the fragmentation process of $[2L + 3Ag − 4H]^−$. The decarboxylation obtained after excitation of the precursor ion ($[2L + 3Ag − 4H]^−$) results in the attachment of CH_2 to the silver trimer, which slightly reduces the net charge of the silver cluster from +1.69 to +1.39. Since this species is not the most stable isomer, it can undergo a reductive elimination reaction with a barrier of 1.48 eV forming an ester bond between the CH_2 and the COO groups. This leads to a silver cluster with a net charge of +0.3. Alternatively to this reductive elimination reaction, the loss of SCH_2 can occur forming $[1L + Ag_3 − 2H]^−$ over transition state (TS_3) that is significantly lower in energy than over the previous one (TS_2) as confirmed experimentally since the species with an ester bond has not been observed as pointed out later. Thus the energy profiles shown in Fig. 3b confirm the experimental finding that the loss of SCH_2 occurs preferably without formation of the ester bond leading directly to the formation of $[1L + Ag_3 − 2H]^−$ with two confined electrons.

For species containing 4 silver atoms, the complex made of 3 thioglycolic acids and 4 silver atoms was first selected in the full MS. After CID, successive neutral losses of CO_2 and SCH_2 were also observed. The spectra obtained after isolation and activation of the different intermediate species allow us to establish the fragmentation pathways described in Scheme 2.
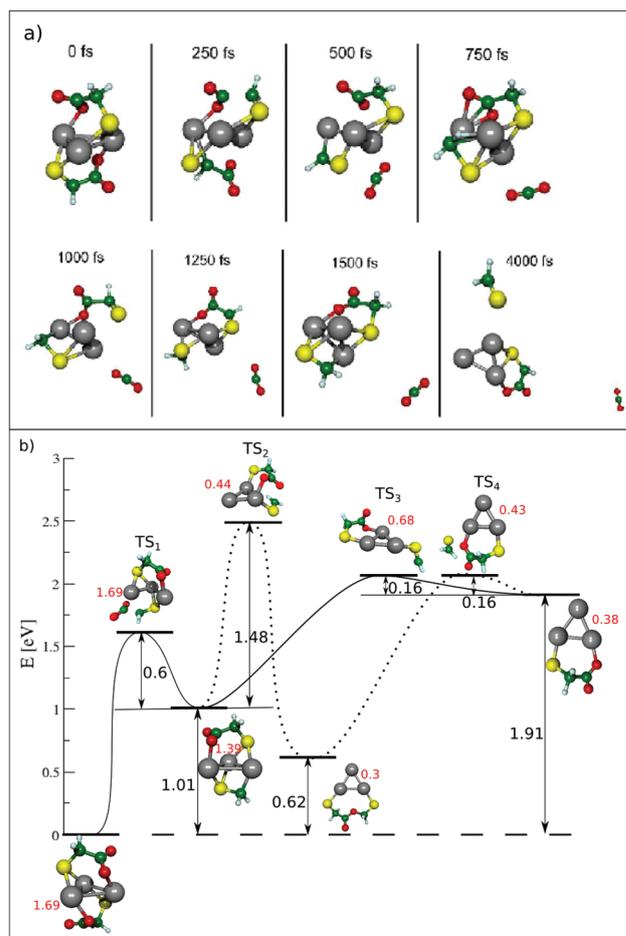

Fig. 3 (a) MD simulation starting from $[2L + 3Ag − 4H]^−$ at $E = 5.0$ eV. (b) Equilibrium and transition state structures, relative energies and NBO charges on a silver trimer starting from $[2L + 3Ag − 4H]^−$. The net charge of silver clusters is indicated in red.

The theoretical MD simulations confirm the first loss of CO_2 as shown in Fig. 4 while for the second loss of CO_2 and the subsequent loss of SCH_2 the simulations on a much longer time scale are needed. In the initial structure of $[3L + 4Ag − 5H]^−$ (*cf.* Fig. 4), two ligands are doubly deprotonated while the third one is singly deprotonated. The three thiolate groups and the two carboxylate groups are bound to silver. The first difference between Schemes 1 and 2 is that, in the case of 4 silver atoms, two CO_2 losses are observed before the loss of
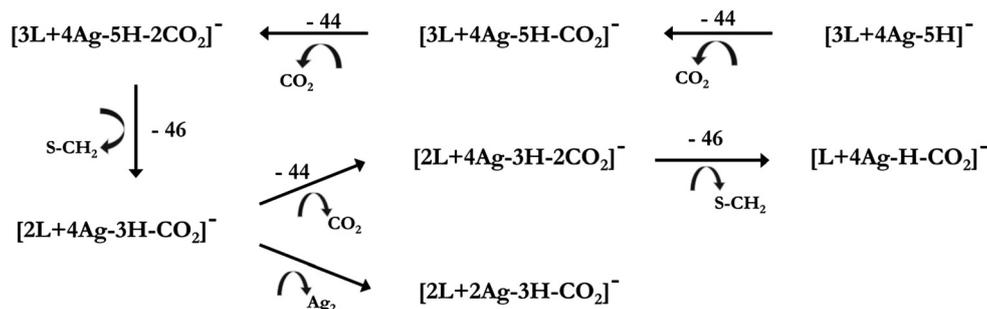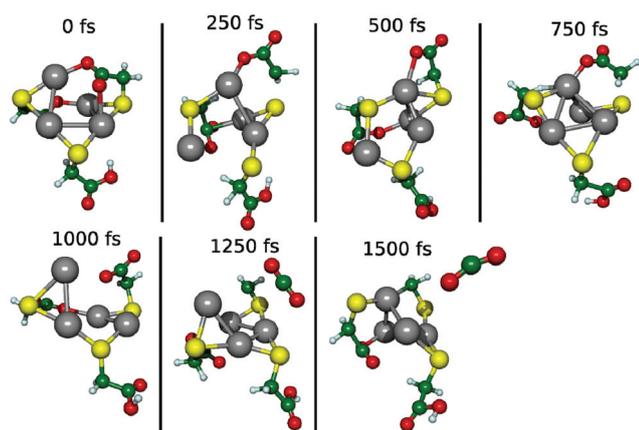
Scheme 2

Fig. 4 MD simulation of the first decarboxylation of $[3L + 4Ag − 5H]^−$ at $E = 5.0$ eV.
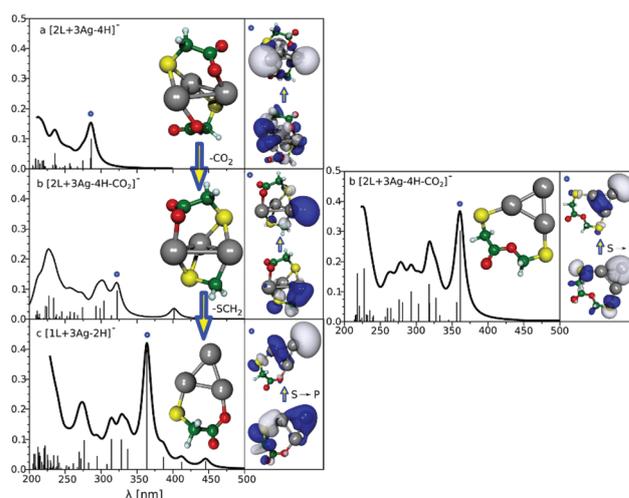

Fig. 5 Calculated spectra and transitions computed for a $[2L + 3Ag − 4H]^−$, b $[2L + 3Ag − 4H − CO_2]^−$ and c $[L + 3Ag − 2H]^−$. Orbitals for leading excitation corresponding to the marked transition are shown (cutoff for all orbitals is 0.025). Right panel corresponds to the structure of $[2L + 3Ag − 4H − CO_2]^−$ with an ester bond.

Fig. 6 Calculated electron localization functions for $[L + 3Ag − 2H]^−$ (left) and for $[2L + 4Ag − 3H − CO_2]^−$ illustrating confined electrons within the metallic subunit.

SCH$_2$. This reflects the higher strength of silver–sulphur bonds as compared to carboxylate–silver bonds. No ester bonds are formed after the first or second decarboxylation. Activation of the last complex is followed by the loss of Ag$_2$ or of the last CO$_2$ group followed by the loss of S═CH$_2$.

The optical spectrum calculated for the $[2L + 3Ag − 4H]^−$ complex displays a leading HOMO–LUMO excitation for transition at ~290 nm arising mainly from sulfur–silver binding orbitals to a linear combination of silver s-orbitals (*cf.* Fig. 5). After decarboxylation in principle two species can be formed. In the first species the ligands are bound above and below the Ag$_3$ plane, while in the second one an ester bond is formed between both ligands, bridging an Ag$_3$ subunit from the side. The absorption bands for the first species are red shifted. The first transition with low intensity appears at 400 nm and is due to excitation from the S–Ag and C–Ag bonds into the silver atom s orbital within the S–Ag–S bridge. The transition at 320 nm arises from the excitation from the S–Ag and C–Ag bonds into the silver atom s orbital bridging the sulphur and carbon atoms. The spectroscopic pattern of the second species in which an ester bond is formed is characterized by a strong transition at 360 nm (corresponding to S–P excitation within the cluster subunit). After loss of CO$_2$ and of the S═CH$_2$ part, the main feature in the optical spectrum is an intense S–P excitation at 360 nm accompanied by several weaker transitions at

higher wavelengths. The position and oscillator strength of the S–P excitation are directly related to the confinement of two electrons in the silver subunit as illustrated in Fig. 6.

Experimental photofragmentation yields were measured for the three complexes $([2L + 3Ag − 4H]^−$, $[2L + 3Ag − 4H − CO_2]^−$, $[L + 3Ag − 2H]^−)$ at 3 wavelengths chosen to be

Fig. 7 Relative experimental photofragmentation yields recorded at 3 wavelengths. For each species the main relaxation channel is the loss of one electron leading to a neutral species. The photofragmentation yield is defined by $\ln(I0_{precursor}/(I_{precursor}))$ where $I0_{precursor}$ and $I_{precursor}$ are the intensities of the precursor ion signals recorded without and with laser irradiation.

discriminant for structural assignment. The main relaxation channel after photoexcitation is an electron loss resulting in a neutral species, which cannot be detected. In addition, 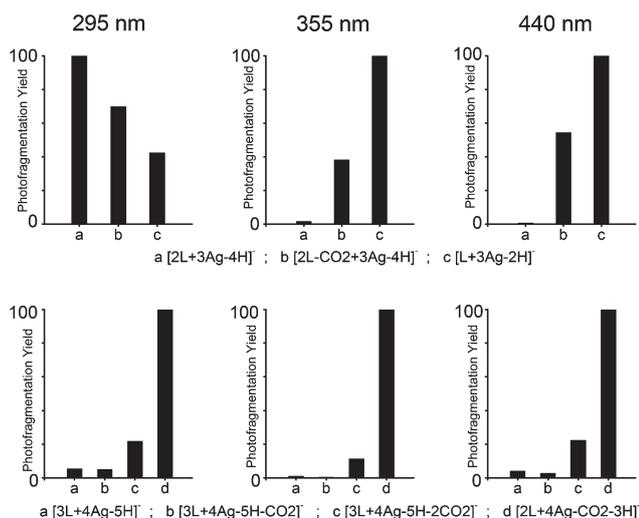ion products similar to those obtained after collisional excitation are observed, except for $[L + 3Ag - 2H]^-)$ for which Ag_3^- is the only species obtained in the mass spectrum after photoexcitation (in addition to the electron loss). The total yield of fragmentation is obtained by comparing the intensity of the parent ion peak with and without laser irradiation. Results are shown in Fig. 7. According to calculations, at 295 nm, all complexes are expected to absorb. At 355 and at 440 nm, absorption is expected only for species with confined electrons. Experimental results confirmed that while the first species ($[2L + 3Ag - 4H]^-$) is not excited at 355 and 440 nm, the two others show electron loss (main relaxation channel) and fragmentation at these wavelengths. For $[2L + 3Ag - 4H - CO_2]^-$, the species with the ester bond does not show absorption at 440 nm which has been observed experimentally and corresponds to the transition calculated at 400 nm for the species without the ester bond (*cf.* Fig. 5b, left panel).

The theoretical absorption spectra of the initial species with 4 silver atoms and after the first decarboxylation are very similar as shown in Fig. 8 since the silver cluster subunit with confined electrons is not yet formed. No transitions above 260 nm are observed and the intense absorptions around 225 nm arise from binding Ag–S orbitals to mixed states composed of unoccupied cluster S, P and D orbitals. The most contributing excitations are shown on the right hand side of Fig. 8. The second decarboxylation gives rise to the transition which involves excitations from the bonds of SCH_2 to the silver cluster orbitals which is slightly red shifted to 280 nm. After the loss of SCH_2 three intense transitions arise at 456 nm, 388 nm and 321 nm corresponding to excitations from the
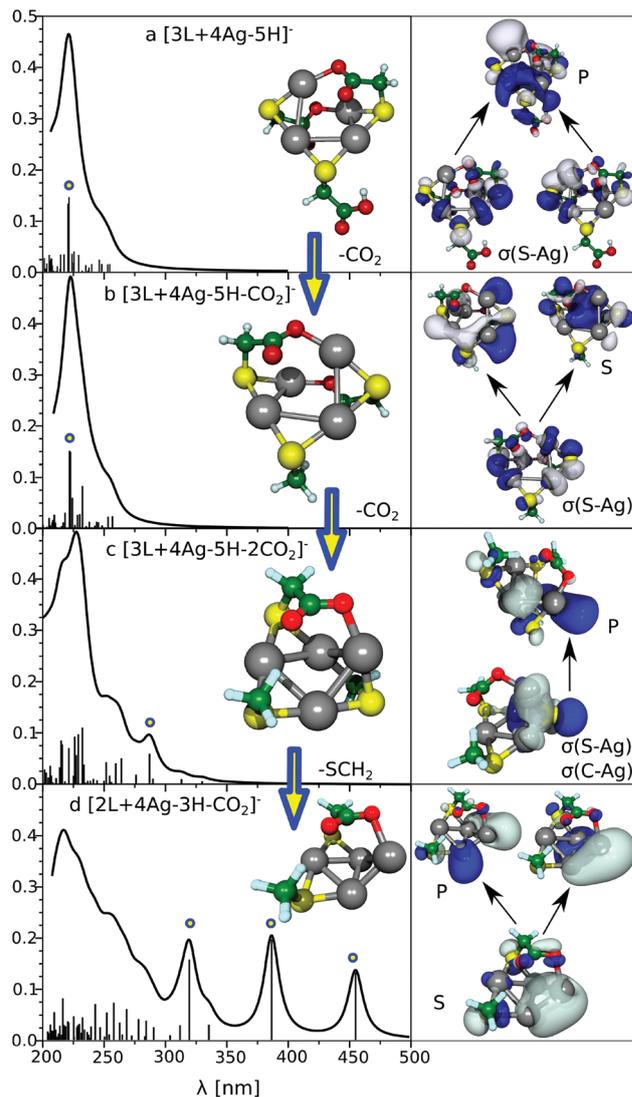
Fig. 8 Calculated spectra and transitions computed for (a) $[3L + 4Ag - 5H]^-$, (b) $[3L + 4Ag - 5H - CO_2]^-$, (c) $[3L + 4Ag - 5H - 2CO_2]^-$ and (d) $[2L + 4Ag - CO_2 - 3H]^-$. Orbitals for leading excitation corresponding to the marked transition are shown. For $[2L + 4Ag - CO_2 - 3H]^-$, two transitions for the 3 s–p type transitions are shown (the cut-off value for the orbitals was 0.025).

cluster S-orbital to the three cluster P-orbitals (only the first two are shown). Experimental results (Fig. 7) clearly show a strong increase in photofragmentation yield for the species $[2L + 4Ag - CO_2 - 3H]^-$ as compared to the yields recorded for the other species, which is in agreement with two confined electrons within the silver subunit as illustrated in Fig. 6.

Conclusion

Altogether, these results show that gas phase reactivity in an ion trap allows us to produce in a controlled way liganded metal clusters either without or with 2 electrons confined within the cluster subunit, exhibiting unique optical properties. Changes in the number of confined electrons occur

through a reductive elimination reaction with charge transfers between the metal part and the carboxylate and thiolate groups induced by losses of thiolate and carboxylic groups. The presented formation process can be used as a prototype for tuning optical and chemical properties of ligated metal clusters by varying the number of confined electrons.

Acknowledgements

References

1 M. C. Daniel and D. Astruc, *Chem. Rev.*, 2004, **104**, 293–346.
2 P. K. Jain, X. Huang, I. H. El-Sayed and M. A. El-Sayed, *Acc. Chem. Res.*, 2008, **41**, 1578–1586.
3 S. W. Chen, R. S. Ingram, M. J. Hostetler, J. J. Pietron, R. W. Murray, T. G. Schaaff, J. T. Khoury, M. M. Alvarez and R. L. Whetten, *Science*, 1998, **280**, 2098–2101.
4 M. A. El-Sayed, *Acc. Chem. Res.*, 2001, **34**, 257–264.
5 W. A. de Heer, *Rev. Mod. Phys.*, 1993, **65**, 611–676.
6 T. G. Schaaff, M. N. Shafigullin, J. T. Khoury, I. Vezmar, R. L. Whetten, W. G. Cullen, P. N. First, C. Gutierrez-Wing, J. Ascensio and M. J. Jose-Yacaman, *J. Phys. Chem. B*, 1997, **101**, 7885–7891.
7 R. L. Whetten, M. N. Shafigullin, J. T. Khoury, T. G. Schaaff, I. Vezmar, M. M. Alvarez and A. Wilkinson, *Acc. Chem. Res.*, 1999, **32**, 397–406.
8 A. C. Templeton, W. P. Wuelfing and R. W. Murray, *Acc. Chem. Res.*, 2000, **33**, 27–36.
9 Y. Negishi, K. Nobusada and T. Tsukuda, *J. Am. Chem. Soc.*, 2005, **127**, 5261–5270.
10 R. Jin, *Nanoscale*, 2010, **2**, 343–362.
11 C. M. Aikens, *J. Phys. Chem. Lett.*, 2011, **2**, 99–104.
12 R. Hamouda, B. Bellina, F. Bertorelle, I. Compagnon, R. Antoine, M. Broyer, D. Rayane and P. Dugourd, *J. Phys. Chem. Lett.*, 2010, **1**, 3189–3194.
13 M. Walter, J. Akola, O. Lopez-Acevedo, P. D. Jadzinsky, G. Calero, C. J. Ackerson, R. L. Whetten, H. Groenbeck and H. Hakkinen, *Proc. Natl. Acad. Sci. U. S. A.*, 2008, **105**, 9157–9162.
14 G. N. Khairallah and R. A. J. O'Hair, *Angew. Chem., Int. Ed.*, 2005, **44**, 728–731.
15 C. Brunet, R. Antoine, M. Broyer, P. Dugourd, A. Kulesza, J. Petersen, M. I. S. Röhr, R. Mitric, V. Bonacic-Koutecky and R. A. J. O'Hair, *J. Phys. Chem. A*, 2011, **115**, 9120–9127.
16 G. N. Khairallah, T. Waters and R. A. J. O'Hair, *Dalton Trans.*, 2009, 2832–2836, DOI: 10.1039/b822371h.
17 T. Tabarin, A. Kulesza, R. Antoine, R. Mitric, M. Broyer, P. Dugourd and V. Bonacic-Koutecky, *Phys. Rev. Lett.*, 2008, **101**, 213001.
18 V. Bonacic-Koutecky, A. Kulesza, L. Gell, R. Mitric, R. Antoine, F. Bertorelle, R. Hamouda, D. Rayane, M. Broyer, T. Tabarin and P. Dugourd, *Phys. Chem. Chem. Phys.*, 2012, **14**, 9282–9290.
19 J. P. Perdew, K. Burke and M. Ernzerhof, *Phys. Rev. Lett.*, 1996, **77**, 3865–3868.
20 D. Andrae, U. Haussermann, M. Dolg, H. Stoll and H. Preuss, *Theor. Chim. Acta*, 1990, **77**, 123–141.
21 F. Weigend and R. Ahlrichs, *Phys. Chem. Chem. Phys.*, 2005, **7**, 3297–3305.
22 M. J. S. Dewar, E. G. Zoebisch, E. F. Healy and J. J. P. Stewart, *J. Am. Chem. Soc.*, 1985, **107**, 3902–3909.
23 T. Yanai, D. P. Tew and N. C. Handy, *Chem. Phys. Lett.*, 2004, **393**, 51–57.
24 A. D. Becke and K. E. Edgecombe, *J. Chem. Phys.*, 1990, **92**, 5397–5403.
25 B. Bellina, I. Compagnon, F. Bertorelle, M. Broyer, R. Antoine, P. Dugourd, L. Gell, A. Kulesza, R. Mitric and V. Bonacic-Koutecky, *J. Phys. Chem. C*, 2011, **115**, 24549–24554.

Appendix B

UV Photo-dissociation of proline-containing peptide ions: Insights from molecular dynamics

RESEARCH ARTICLE

UV Photodissociation of Proline-containing Peptide Ions: Insights from Molecular Dynamics

Marion Girod,[1,2] Zeljka Sanader,[3] Marin Vojkovic,[1,4] Rodolphe Antoine,[1,4]
Luke MacAleese,[1,4] Jérôme Lemoine,[1,2] Vlasta Bonacic-Koutecky,[3,5] Philippe Dugourd[1,4]

[1]Université de Lyon, F-69622, Lyon, France
[2]Institut des Sciences Analytiques, CNRS et Université Lyon 1 UMR 5280, Lyon, France
[3]Interdisciplinary Center for Advanced Science and Technology (ICAST) at University of Split, Split, Croatia
[4]Institut Lumière Matière, Université Claude Bernard Lyon 1, CNRS UMR 5306, Lyon, France
[5]Institut fur Chemie, Humboldt-Universität Berlin, Berlin, Germany
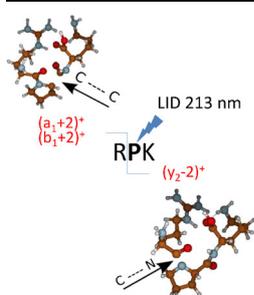
Abstract. UV photodissociation of proline-containing peptide ions leads to unusual product ions. In this paper, we report laser-induced dissociation of a series of proline-containing peptides at 213 nm. We observe specific fragmentation pathways corresponding to the formation of (y-2), (a + 2) and (b + 2) fragment ions. This was not observed at 266 nm or for peptides which do not contain proline residues. In order to obtain insights into the fragmentation dynamics at 213 nm, a small peptide (RPK for arginine-proline-lysine) was studied both theoretically and experimentally. Calculations of absorption spectra and non-adiabatic molecular dynamics (MD) were made. Second and third excited singlet states, S^2 and S^3, lie close to 213 nm. Non-adiabatic MD simulation starting from S^2 and S^3 shows that these transitions are followed by C-C and C-N bond activation close to the proline residue. After this first relaxation step, consecutive rearrangements and proton transfers are required to produce unusual (y-2), (a + 2) and (b + 2) fragment ions. These fragmentation mechanisms were confirmed by H/D exchange experiments.

Key words: Photodissociation, Proline-containing peptides, Fragmentation, Molecular dynamics, H/D exchange

Introduction

Tandem mass spectrometry (MS/MS) is a widely-used method to determine the amino acid sequence of peptides and proteins [1]. In addition, the use of CID (collision-induced dissociation) continues to be important in peptide sequencing and protein identification. In solution, the most basic site on a peptide devoid of histidine, lysine, and arginine residues is the nitrogen atom of the N-terminal amino group [2]. However, once the protonated peptide ion is desorbed into the gas phase, e.g. via electrospray, there is competitive transfer of the "ionizing" proton to amidic functional groups, the carbonyl oxygen and amidic nitrogen atoms on the backbone [3–8]. The peptide

then fragments at the protonated peptide bond [9, 10]. A non-terminal residue has two adjacent peptide linkages, one to the N-terminal and the other to the C-terminal. At low (<100 eV) energy CID, the protonated peptides fragment along the backbone at the amide bonds, and the mass spectrum typically consists of a series of *b*, *a*, and *y* fragment ions. These fragments give valuable information [9, 10] concerning peptide sequence, number and location of disulfide bridges, identification and sometimes characterization of post-translational modifications. However, fragmentation pathways of protonated peptides are difficult to understand and known only at the phenomenological level.

It is apparent from the diverse CID patterns observed that the fragmentation routes of protonated peptides depend significantly on the identity and positions of the amino acids constituting the peptides. It was found that proline (Pro) and to a smaller extent glycine and serine residues tend to fragment at their N-terminal peptide bonds, whereas residues such as valine and isoleucine tend to fragment toward their C-terminal peptide bonds [11]. Other published work using tandem MS on

peptides, e.g., ubiquitin, have often indicated unusually abundant product ions resulting from cleavage of peptide linkages on the N-terminal side of Pro residues [12]. This propensity for selective fragmentation has also been reported for singly-protonated peptides [13–18] and multiply-charged protein ions [19]. This phenomenon is sometimes known as the proline effect and was first attributed to the relatively high proton affinity of Pro [20]. Vaisar and Urban investigated a number of peptides that contained a modified amino acid residue of relatively high proton affinity, most notably one that contained a six-membered piperidine ring as opposed to Pro's five-membered pyrolidine ring, and concluded that proton affinity does not explain the proline effect [17]. They attributed the preferred N-terminal (as opposed to C-terminal) cleavage to Pro in terms of increased ring strain in forming a bicyclic b ion when the C-terminal peptide bond is cleaved. The conformation of the Pro residue may also play an important role in fragmentation. Wysocki and co-workers studied this with a database of low-energy CID tandem mass spectra of doubly-charged peptides [21]. They found that the residue (Xxx) adjacent to Pro affects the extent of fragmentation at the Xxx-Pro bond. Particularly enhanced Xxx-Pro bond cleavage when Xxx is Val, Ile, and Leu was ascribed to the steric hindrance of their bulky side chains, since it causes Pro to take a 'reactive' *trans* form that leads to product ions. However, they did not elucidate the 'reactive' conformation of Pro or the fragmentation mechanism. Infrared multiphoton dissociation (IRMPD) of peptides results in few backbone (b- and y-type) cleavages but increased side-chain fragmentation. In addition, IRMPD showed an increased selectivity toward N-terminal backbone cleavages to Pro [22].

In addition and complementary to CID, reactions of polypeptide ions with electrons and small radical ions, such as electron capture dissociation (ECD) [23, 24] and electron-transfer dissociation (ETD) [25–27], have become very useful tools for peptide structural analysis. The ion–electron and ion–ion reactions are different from slow heating methods, such as CID, by the fact that the intermediate fragmenting species are odd-electron ions. In fact, the presence of a radical site diminishes the strength of nearby bonds. In particular, for peptide polyanions, preferential backbone cleavage of C–C bonds yielding a and x ions as well as side chain fragmentation were demonstrated [28–32]. Specific cleavage of peptide linkages on the N-terminal of Pro residues was also observed in ECD [30, 33, 34].

Vacuum ultraviolet photodissociation (VUVPD) is an elegant, high-energy method for inducing fragmentation in peptides [35]. Following electronic transition, direct dissociation in the excited state competes with radiative relaxation and internal conversion to the electronic ground state. VUVPD of Pro-containing peptide ions was reported with the production of unusual product ions [36]. In particular, unusual $b_n + 2$ and $a_n + 2$ ions were observed. Their formation was explained by homolytic cleavage of the C_α-C bond in conjunction with a rearrangement between electrons and an amide hydrogen. Formation of these abnormal ions has been compared to the effect of Pro on gas-phase conformation of peptides. UVPD of peptides at 193 nm was achieved with production of $a, b, c, x, y,$ and z sequence ions, in addition to immonium ions and v and w side-chain loss ions [37]. However, the unusual fragment ions were not reported for the studied sequences.

Herein, we investigate the UVPD of Pro-containing peptides at 213 nm. This wavelength corresponds to the emergence of the lowest-lying electronic excited states of the molecules and thus allows the investigation of the relation between the nature of excited states and the observed fragmentation patterns. The calculation of the electronic excited states and molecular dynamics for the model RPK peptide (arginine-proline-lysine) are reported here in order to gain insight into the first steps of UV photodissociation of Pro-containing peptides. Our complementary theoretical and experimental investigations open a new route for identification of the photofragmentation pathways allowing identification of the link between the nature of electronic excited states and the observed fragmentation pathways.

Material and Methods

Chemicals

Methanol (MeOH) was obtained from Fisher Scientific (Strasbourg, France) and milli-Q water (18.2 MΩ.cm) was used. Deuterated methanol (CH$_3$OD), deuterium oxide (D$_2$O), Bradykinin and Substance P acetate salts were purchased from Sigma–Aldrich (St Quentin-Fallavier, France). LGPLVEQGR, LGADMEDVR and EANYIGSDK peptides were synthesized by Millegen (Labège, France). RPK peptide was synthesized by GeneCust (Dudelange, Luxembourg).

Instrumentation

Experiments were performed on a hybrid quadrupole-orbitrap Q-Exactive® mass spectrometer (Thermo Fisher Scientific, San Jose, CA, USA) equipped with a HESI ion source. The instrument was modified to allow UV laser irradiation of ions. A schematic of the photodissociation set-up is given in Figure 1 quartz window was fitted on the rear of the HCD (High Collision Dissociation) cell to permit introduction of a laser beam. The detector plate, initially positioned at the exit of the HCD cell and on the laser beam trajectory, was removed. The laser is a BrillantB Nd:YAG (from Quantel, Les Ulis, France). The 5th harmonic at λ=213 nm was used with a repetition rate of 20 Hz. This harmonic is generated by combination of the fundamental and 4th harmonic. For experiments at 266 nm, the 4th harmonic was used. The laser beam passes through lenses, diaphragms and is injected in the HCD cell using two dichroic mirrors. The laser beam energy irradiating the ions was ~1 mJ/ pulse. The laser is slightly off axis in order to avoid photofragmentation in the C-trap.
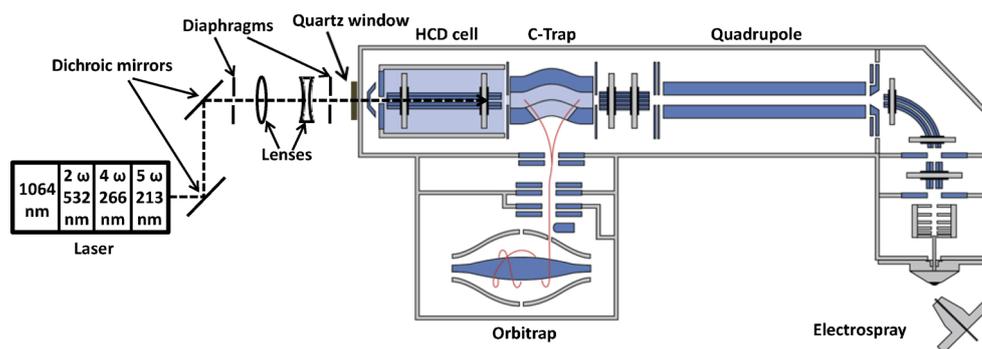
Figure 1. Schematic of the photodissociation experimental set-up in the Q-Exactive mass spectrometer

Mass Spectrometry Operating Conditions

Ionization was achieved using an electrospray in positive ionization mode with an ion spray voltage of 4 500 V. The sheath gas and auxiliary gas (nitrogen) flow rates were set at 20 and 15 (arbitrary unit), respectively, with a HESI vaporizer temperature of 250°C. The ion transfer capillary temperature was 250°C. The S-lens RF was set at 90 (arbitrary unit). The orbitrap resolution was 140 000. The Automatic Gain Control (AGC) target was 3e6 and the maximum injection time was set at 250 ms. For photodissociation experiments, the HCD parameters were optimized in order to avoid CID and were set at 2 eV for the collision energy and 1000 ms for the activation time. CID experiments were performed using a normalized collision energy of 25% and 3 ms activation time. An m/z window of 2.0 Th was applied for precursor isolation. Peptides were dissolved in 50/50 MeOH/water (vol/vol) at a

concentration of 100 μM and directly electrosprayed at a flow rate of 5 μL/min.

Computation

Investigation of the structures of the RPK model system (arginine + proline + lysine) was done using the simulated annealing method coupled to molecular dynamic simulations using the semi-empirical AM1 method [38]. The structures found were then re-optimized using the semi-empirical OM2 (orthogonalization model 2) method [39]. To calculate the absorption spectra, the OM2 method combined with the graphical unitary group approach (GUGA) multi-reference configuration interaction (MR-CI) [40, 41] within the MNDO program [42] was used. The active space which consists of five occupied and five virtual orbitals was chosen, and all single, double, and
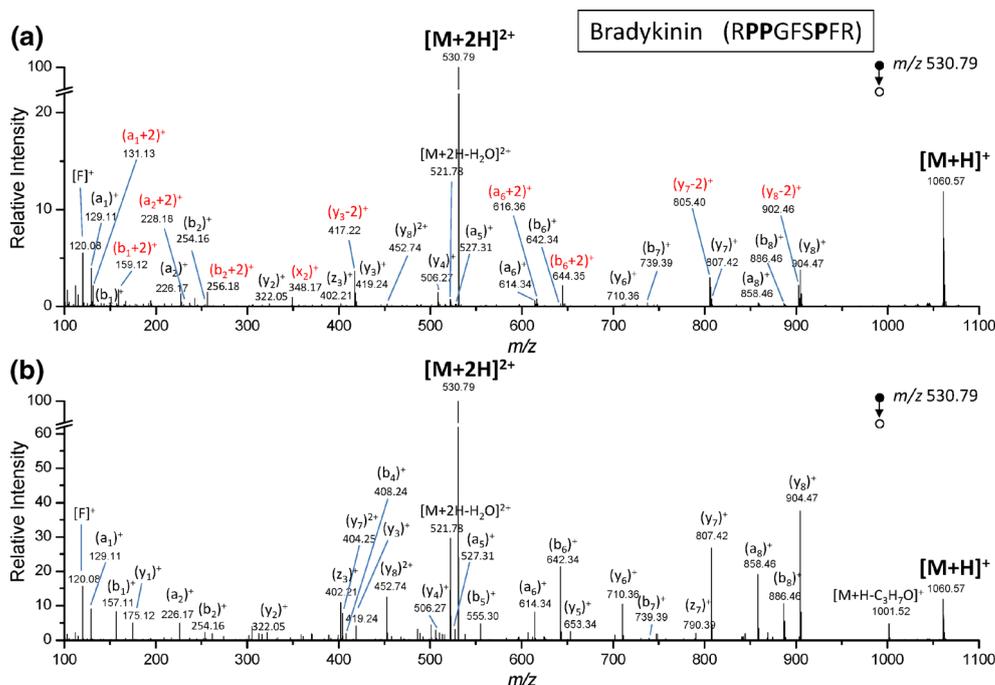

Figure 2. (a) Photodissociation spectrum of the doubly-protonated Bradykinin [M + 2H]$^{2+}$ ion (m/z 530.79) at 213 nm for 1000 ms (Collision energy 2 eV). (b) CID spectrum of doubly-protonated Bradykinin [M + 2H]$^{2+}$ ion (m/z 530.79) under a normalized CID collision energy of 25% for 3 ms

triple excitations out of the self-consistent field reference configurations were included in the calculations.

Since the experiments were done at a temperature close to 300 K, we simulated the thermally-broadened absorption spectra. The configurations were sampled from a long molecular dynamic trajectory run at a constant temperature of 300 K using the semi-empirical OM2 method. To simulate the temperature broadening of the spectrum, the absorption spectrum for each configuration was calculated and these spectra were superimposed. The non-adiabatic dynamics "on the fly" in electronic excited states were determined using Tully's surface-hopping algorithm with non-adiabatic couplings [43]. The initial conditions for non-adiabatic dynamics were obtained by sampling 100 coordinates and momenta along a 30 ps ground-state trajectory at a constant temperature of 300 K using the OM2 method. The nuclear trajectories were propagated by numerical solution of Newton's equations of motion using the Verlet velocity algorithm [44] with a time step of 0.1 fs. The non-adiabatic dynamics were determined starting from S_2 or S_3 state matching experimental conditions.

Results and Discussion

The Photodissociation of Pro-containing Peptides

The 213 nm photodissociation spectrum of the doubly-protonated $[M + 2H]^{2+}$ (m/z 530.79) of Bradykinin (RPPGFSPFR) is shown in Figure 2a. A series of singly-charged $(y_n)^+$, $(b_n)^+$ and $(a_n)^+$ ions are mainly observed with a 10% relative intensity. $(y_n)^+$ ions are detected for n =2 to 4 and 6 to 8. $(b_n)^+$ ions are detected for n =1, 2 and 6 to 8, while $(a_n)^+$ ions are detected for n =1, 2, 5, 6 and 8. The $(z_3)^+$ ion is also detected at m/z 402.21 as well as doubly-charged $(y_8)^{2+}$ at m/z 452.74. The peptide sequence can be confirmed with these backbone fragment ions. The immonium ion of the phenylalanine residue $[F]^+$ is detected at m/z 120.08. Loss of a water

Table 1. Exact masses and assignments of fragment ions detected in the photodissociation and CID spectra of doubly-protonated Bradykinin $[M + 2H]^{2+}$ (Figure 2). Error=(m/z theoretical – m/z experimental)/(m/z theoretical)

| Assignment	Elemental composition	Theoretical m/z	Photodissociation		CID	
			Experimental m/z	Error (ppm)	Experimental m/z	Error (ppm)
$[M + H]^+$	$C_{50}H_{74}O_{11}N_{15}$	1060.5687	1060.5693	0.566	1060.5694	0.660
$[M + H-C_3H_7O]^+$	$C_{47}H_{67}O_{10}N_{15}$	1001.5190	ND	NA	1001.5197	0.699
$(y_8)^+$	$C_{44}H_{62}O_{10}N_{11}$	904.4676	904.4673	−0.332	904.4680	0.442
$(y_8-2)^+$	$C_{44}H_{60}O_{10}N_{11}$	902.4550	902.4553	0.377	ND	NA
$(b_8)^+$	$C_{44}H_{60}O_9N_{11}$	886.4570	886.4573	0.338	886.4575	0.564
$(a_8)^+$	$C_{43}H_{60}O_8N_{11}$	858.4621	858.4628	0.815	858.4625	0.466
$(y_7)^+$	$C_{39}H_{55}O_9N_{10}$	807.4148	807.4153	0.619	807.4152	0.495
$(y_7-2)^+$	$C_{39}H_{53}O_9N_{10}$	805.3991	805.3995	0.497	ND	NA
$(z_7)^+$	$C_{39}H_{52}O_9N_9$	790.3883	ND	NA	790.3880	−0.380
$(b_7)^+$	$C_{35}H_{51}O_8N_{10}$	739.3886	739.3892	0.811	739.3889	0.406
$(y_6)^+$	$C_{34}H_{48}O_8N_9$	710.3620	710.3616	−0.563	710.3624	0.563
$(y_5)^+$	$C_{32}H_{45}O_7N_8$	653.3406	ND	NA	653.3409	0.459
$(b_6 + 2)^+$	$C_{30}H_{46}O_7N_9$	644.3515	644.3518	0.466	ND	NA
$(b_6)^+$	$C_{30}H_{44}O_7N_9$	642.3358	642.3360	0.311	642.3361	0.467
$(a_6 + 2)^+$	$C_{29}H_{46}O_6N_9$	616.3566	616.3563	−0.487	ND	NA
$(a_6)^+$	$C_{29}H_{44}O_6N_9$	614.3409	614.3406	−0.488	614.3412	0.488
$(b_5)^+$	$C_{27}H_{39}O_5N_8$	555.3038	ND	NA	555.3040	0.342
$[M + 2H]^{2+}$	$C_{50}H_{75}O_{11}N_{15}$	530.7880	530.7877	−0.565	530.7883	0.565
$(a_5)^+$	$C_{26}H_{39}O_4N_8$	527.3089	527.3093	0.759	527.3092	0.569
$[M + 2H-H_2O]^{2+}$	$C_{50}H_{73}O_{10}N_{15}$	521.7827	521.7824	−0.575	521.7831	0.767
$(y_4)^+$	$C_{23}H_{36}O_6N_7$	506.2722	506.2718	−0.790	506.2724	0.395
$(y_8)^{2+}$	$C_{44}H_{63}O_{10}N_{11}$	452.7374	452.7371	−0.663	452.7371	−0.663
$(y_3)^+$	$C_{20}H_{31}O_4N_6$	419.2401	419.2399	−0.477	419.2397	−0.954
$(y_3-2)^+$	$C_{20}H_{29}O_4N_6$	417.2245	417.2242	−0.719	ND	NA
$(b_4)^+$	$C_{18}H_{30}O_4N_7$	408.2354	ND	NA	408.2350	−0.980
$(y_7)^{2+}$	$C_{39}H_{56}O_9N_{10}$	404.2110	ND	NA	404.2108	−0.495
$(z_3)^+$	$C_{20}H_{28}O_4N_5$	402.2136	402.2131	−1.243	402.2134	−0.497
$(\times_2)^+$	$C_{16}H_{22}O_4N_5$	348.1666	348.1668	0.574	ND	NA
$(y_2)^+$	$C_{15}H_{24}O_3N_5$	322.1874	322.1873	−0.310	322.1870	−1.242
$(b_2 + 2)^+$	$C_{11}H_{22}O_2N_5$	256.1768	256.1767	−0.390	ND	NA
$(b_2)^+$	$C_{11}H_{20}O_2N_5$	254.1612	254.1609	−1.180	254.1610	−0.787
$(a_2 + 2)^+$	$C_{10}H_{22}ON_5$	228.1819	228.1820	0.438	ND	NA
$(a_2)^+$	$C_{10}H_{20}ON_5$	226.1662	226.1663	0.442	226.1664	0.884
$(y_1)^+$	$C_6H_{15}O_2N_4$	175.1190	ND	NA	175.1191	0.571
$(b_1 + 2)^+$	$C_6H_{15}ON_4$	159.1240	159.1239	−0.628	ND	NA
$(b_1)^+$	$C_6H_{13}ON_4$	157.1084	157.1082	−1.273	157.1081	−1.910
$(a_1 + 2)^+$	$C_5H_{15}N_4$	131.1291	131.1290	−0.991	ND	NA
$(a_1)^+$	$C_5H_{13}N_4$	129.1135	129.1133	−1.549	129.1133	−1.549
$[F]^+$	$C_8H_{10}N$	120.0808	120.0809	1.166	120.0807	−1.249
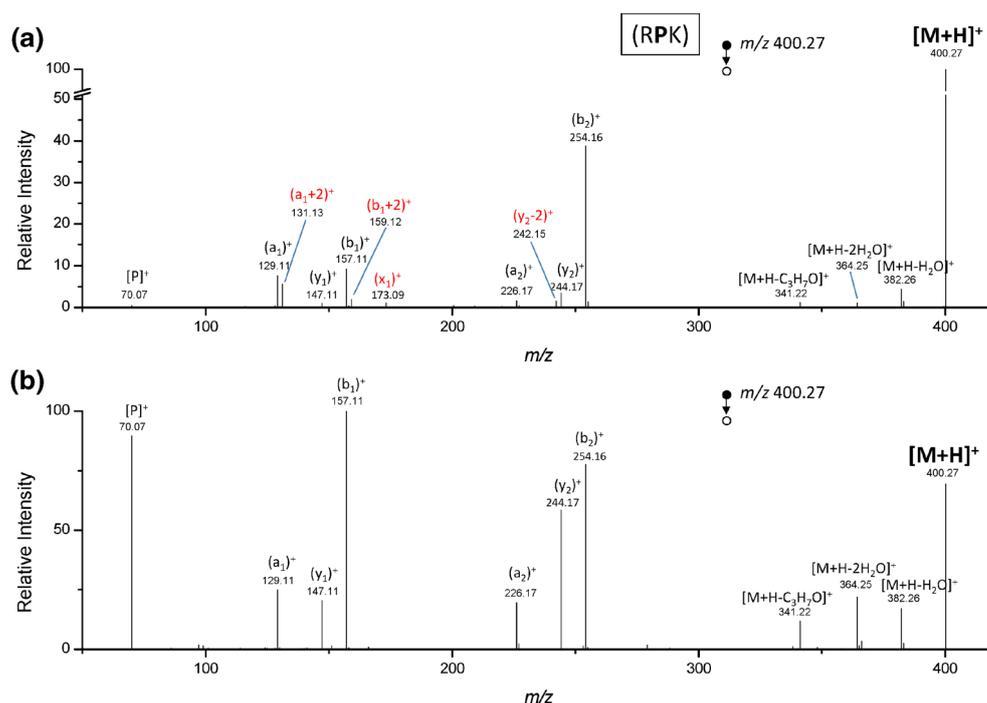
Figure 3. (a) Photodissociation spectrum of protonated RPK [M + H]$^+$ ion (*m/z* 400.27) at 213 nm for 1000 ms (Collision energy 2 eV). (b) CID spectrum of protonated RPK [M + H]$^+$ ion (*m/z* 400.27) under a normalized CID collision energy of 25% for 3 ms

molecule from the doubly-charged ion precursor is also observed yielding the [M + 2H-H$_2$O]$^{2+}$ ion (*m/z* 521.78). Charge reduced [M + H]$^+$ is detected at *m/z* 1060.57. We assigned these fragment ions and confirmed them by the exact masses reported in Table 1. The errors were all less than 2 ppm. For comparison, the CID spectrum of doubly-protonated [M + 2H]$^{2+}$ (*m/z* 530.79) of Bradykinin is shown in Figure 2b. Backbone fragment ions are also observed as well as water elimination and the [M + H]$^+$ ion (Table 1).

More interestingly, photodissociation at 213 nm generates new fragments that are not observed in the CID spectrum. The assignment of these ions was confirmed by the exact masses

(Table 1). Fragment ions detected at *m/z* 902.46, *m/z* 805.40 and *m/z* 417.22 correspond to the elemental composition of y ions minus 2 hydrogens and have been labeled in Figure 2a (y$_8$-2)$^+$, (y$_7$-2)$^+$ and (y$_3$-2)$^+$, respectively. These y$_n$-2 ions are not observed along the whole peptide sequence. This fragmentation pathway occurs only with a Pro residue. In fact, Bradykinin contains 3 Pro residues Pro2, Pro3 and Pro7 among a total of 9 amino acid residues giving rise to (y$_8$-2)$^+$, (y$_7$-2)$^+$ and (y$_3$-2)$^+$ ions. These ions are more intense compared to their homologue y$_n$ ions. The relative intensities of (y$_8$-2)$^+$, (y$_7$-2)$^+$ and (y$_3$-2)$^+$ ions correspond to 50%, 150% and 300% of the relative intensities of (y$_8$)$^+$, (y$_7$)$^+$ and (y$_3$)$^+$, respectively.

Table 2. Exact masses and assignments of fragment ions detected in the photodissociation and CID spectra of protonated RPK [M + H]$^+$ (Figure 3). Error=(*m/z* theoretical – *m/z* experimental)/(*m/z* theoretical)

Assignment	Elemental composition	Theoretical *m/z*	Photodissociation		CID	
			Experimental *m/z*	Error (ppm)	Experimental *m/z*	Error (ppm)
[M + H]$^+$	C$_{17}$H$_{34}$O$_4$N$_7$	400.2667	400.2665	−0.500	400.2663	−0.999
[M + H-H$_2$O]$^+$	C$_{17}$H$_{32}$O$_3$N$_7$	382.2561	382.2564	0.785	382.256	−0.262
[M + H-2H$_2$O]$^+$	C$_{17}$H$_{30}$O$_2$N$_7$	364.2455	364.2457	0.549	364.2457	0.549
[M + H-C$_3$H$_7$O]$^+$	C$_{14}$H$_{27}$O$_3$N$_7$	341.2170	341.2168	−0.586	341.2173	0.879
(b$_2$)$^+$	C$_{11}$H$_{20}$O$_2$N$_5$	254.1612	254.1610	−0.787	254.1609	−1.180
(y$_2$)$^+$	C$_{11}$H$_{22}$O$_3$N$_3$	244.1656	244.1654	−0.819	244.1653	−1.229
(y$_2$-2)$^+$	C$_{11}$H$_{20}$O$_3$N$_3$	242.1499	242.1502	1.239	ND	NA
(a$_2$)$^+$	C$_{10}$H$_{20}$ON$_5$	226.1662	226.1660	−0.884	226.1660	−0.884
(×$_1$)$^+$	C$_6$H$_{13}$O$_2$N$_4$	173.0921	173.0924	1.733	ND	NA
(b$_1$ + 2)$^+$	C$_6$H$_{15}$ON$_4$	159.1240	159.1238	−1.257	ND	NA
(b$_1$)$^+$	C$_6$H$_{13}$ON$_4$	157.1084	157.1082	−1.273	157.1081	−1.910
(y$_1$)$^+$	C$_6$H$_{15}$O$_2$N$_2$	147.1128	147.1129	0.680	147.1130	1.360
(a$_1$ + 2)$^+$	C$_5$H$_{15}$N$_4$	131.1291	131.1293	1.525	ND	NA
(a$_1$)$^+$	C$_5$H$_{13}$N$_4$	129.1135	129.1133	−1.549	129.1133	−1.549
[P]$^+$	C$_4$H$_8$N	70.0651	70.0652	1.427	70.0650	−1.427

Fragment ions detected at m/z 159.12, m/z 256.18 and m/z 644.35 have the elemental composition of b ions plus 2 hydrogens and, in Figure 2a, have been labeled $(b_1 + 2)^+$, $(b_2 + 2)^+$ and $(b_6 + 2)^+$, respectively. This fragmentation reaction is very efficient compared to the classical mechanism as the relative intensities of $(b_1 + 2)^+$, $(b_2 + 2)^+$ and $(b_6 + 2)^+$ ions represent 400, 500 and 700% of the relative intensities of their b_n homologues. The same behavior is observed for the fragment ions detected at m/z 131.13, m/z 228.18 and m/z 616.36 which correspond to a_n ions plus 2 hydrogens and, in Figure 2a, have been labeled $(a_1 + 2)^+$, $(a_2 + 2)^+$ and $(a_6 + 2)^+$, respectively. Furthermore, these ions are only observed in the neighborhood of the Pro residues. The $(\times_3)^+$ ion is detected at m/z 348.17 in the photodissociation spectrum. Kim et al. [36] also observed these unusual fragment ions in the UVPD of singly-charged Pro-containing peptides at 157 nm.

The same photodissociation experiment was done for the doubly-protonated $[M + 2H]^{2+}$ of Substance P (RPKPQQFFGLM) (m/z 674.86) and LGPLVEQGR (m/z 484.77) peptides. The spectra are shown in Figures S1 and S2 in the Supporting material. Besides the backbone fragments y_n, b_n and a_n observed in photodissociation and CID, UVPD spectra show y_n-2, $b_n + 2$ and $a_n + 2$ fragment ions. For the doubly-protonated Substance P peptide which contains 2 Pro residues Pro2 and Pro4, $(y_{10}$-2$)^+$ and $(y_8$-2$)^+$ ions are detected at m/z 1190.60 and m/z 965.45 corresponding to y ions minus 2 hydrogens (according to exact masses). b and a fragment ions plus 2 hydrogens $(a_1 + 2)^+$, $(b_1 + 2)^+$, $(a_3 + 2)^+$ and $(b_3 + 2)^+$ are detected at m/z 131.12, m/z 159.12, m/z 356.19 and m/z 384.26, respectively. The $(\times_7)^+$ ion is detected at m/z 640.28 in the photodissociation spectrum. All assignment errors were less than 1.3 ppm. In the photodissociation spectrum of doubly-protonated LGPLVEQGR, which has a Pro3 residue among a total of 9 amino acid (AA) residues, $(y_7$-2$)^+$, $(a_2 + 2)^+$ and $(b_2 + 2)^+$ are detected at m/z 796.43, m/z 173.13 and m/z 145.13, respectively (Figure S2). From these 3 examples, we can conclude that $(y_n$-2$)^+$ ions are only observed in photodissociation for n=(total number of AA - #Pro +1). These ions still contain the Pro residue. On the other hand, $(b_n + 2)^+$ and $(a_n + 2)^+$ ions are only observed in photodissociation for n=(#Pro - 1), and they do not contain the Pro residue. These fragmentation pathways are observed only with cleavage of bonds between the amino acid N-terminal to Pro and the Pro residue. In order to confirm the contribution of the Pro residue in these fragmentation pathways, photodissociation experiments were done at 213 nm for doubly-protonated ions of LGADMEDVR (m/z 503.24) and EANYIGSDK (m/z 498.74) peptides that do not contain Pro. The UVPD spectra are presented in Figures S3 and S4, respectively. In these cases, photodissociation and CID spectra are similar. No $(y_n$-2$)^+$, $(b_n + 2)^+$ or $(a_n + 2)^+$ ions are detected in photodissociation. Therefore, the effect of the excited Pro residue is clearly evident in these new mechanisms. Note that photodissociation experiments were also done at 266 nm for the Pro-containing peptides and new fragment ions were not observed (data not shown). The fact that no unusual fragments close to the Pro were observed means that a higher energy UV excitation (below 266 nm) is required to induce these specific photo-fragments.

Photodissociation and Optical Properties of the Protonated RPK Model Peptide

In order to understand the proline effect, the specificity of VUV excitation and the mechanisms involved in the formation of the unusual fragment ions, a model RPK peptide was used for photodissociation experiments at 213 nm. The optical properties were calculated in parallel to the experiments. Figure 3a shows the 213 nm photodissociation mass spectrum of the singly-
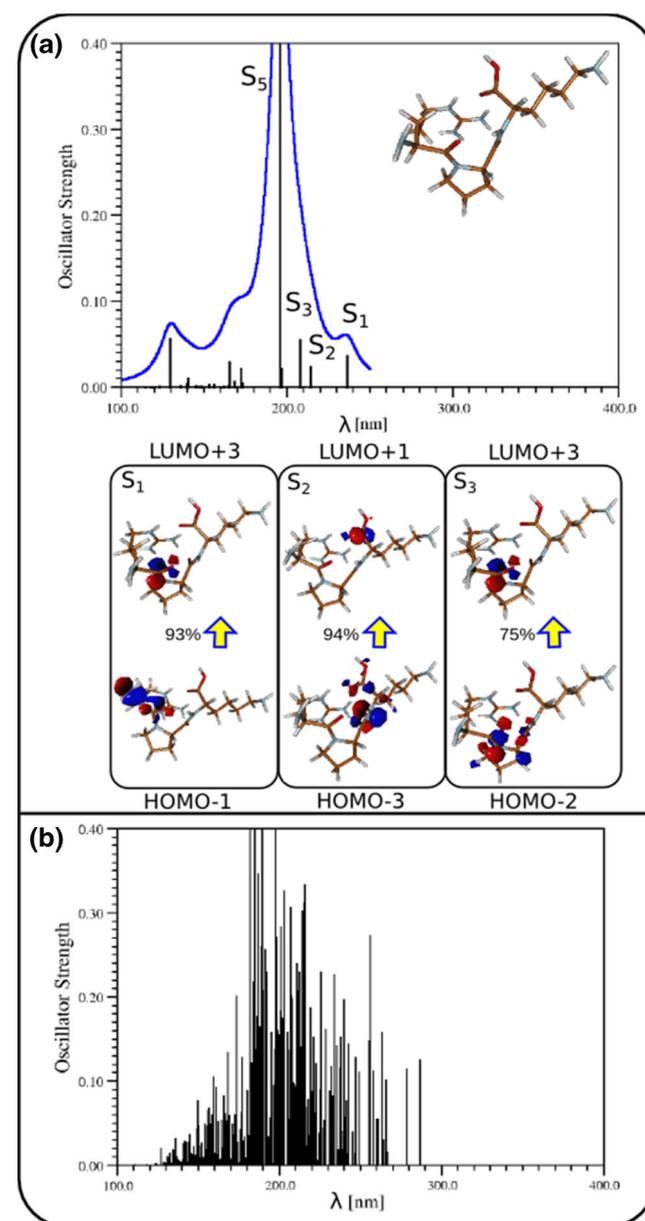

Figure 4. (a) Calculated spectrum for the lowest energy structure of protonated RPK $[M + H]^+$ ion, using the semi-empirical OM2 method at T=0 K. Analysis of leading electronic excitations in first three excited states S_1, S_2 and S_3. (b) Calculated thermally-broadened absorption spectrum at 300 K

protonated $[M + H]^+$ (m/z 400.27) of RPK peptide. Singly-charged $(y_1-2)^+$, $(b_1-2)^+$ and $(a_1-2)^+$ ions are mainly observed with a 20% relative intensity. The immonium ion of the Pro residue $[P]^+$ is detected at m/z 70.07. We observed that one and two water molecules were lost from the precursor ion yielding the $[M + H-H_2O]^+$ ion (m/z 382.26) and $[M + H-2H_2O]^+$ ion (m/z 364.25). The fragment ion detected at m/z 341.22 arises from the loss of C_3H_7O from the precursor ion. The errors were all less than 1.7 ppm. The CID spectrum of the protonated $[M + H]^+$ (m/z 400.27) of RPK is used as a reference in Figure 3b. Intense backbone fragment ions are also observed as well as water eliminations and $[P]^+$ (Table 2). The photodissociation of the protonated RPK peptide ion also shows the unusual $(y_2-2)^+$, $(\times_1)^+$, $(b_1 + 2)^+$ and $(a_1 + 2)^+$ ions detected at m/z 242.15, m/z 173.06, m/z 159.12 and m/z 131.13, respectively (Figure 3a), in contrast to the CID spectrum. All the assignments were confirmed by exact masses (Table 2).

The structural properties of $[M + H]^+$ of the RPK model system were determined via semi-empirical calculations (OM2) as described in the computational section. A number of structures with different binding sites for protons were explored and the lowest energy one has a proton bound to the Arginine side chain NH group (pKa value=12). The calculated OM2 spectrum at T=0 K for the lowest energy structure is shown in Figure 4a. The absorption features are characterized by a dominant transition to the S_5 excited state at 195 nm. Transition to S_2 and S_3 excited states with weaker intensity at 214 nm and 207 nm are close to the wavelength used for photodissociation experiments (213 nm). Figure 4a also shows analysis of excitations for the three lowest transitions of the protonated RPK model system in the gas phase. Although, single, double and triple electron excitations were included in calculations, only single excitations have significant contributions in the transitions. Excitations around 200 nm correspond to those of the Pro residue and from the C- and N-terminus of the RPK model system. The lowest excited state S_1 at 236 nm is characterized by a transition from the p orbital of the C atom to the p orbital of the N atom in the Arginine backbone, while the excitation from the p orbital of the N atom to the p orbital of the C atom of the Lysine backbone is characteristic of the transition to the S_2 excited state. The most intense transition to S_5 is dominated by excitation from the p orbital on the N atom in the Lysine backbone to the p orbital on the C atom in Pro.
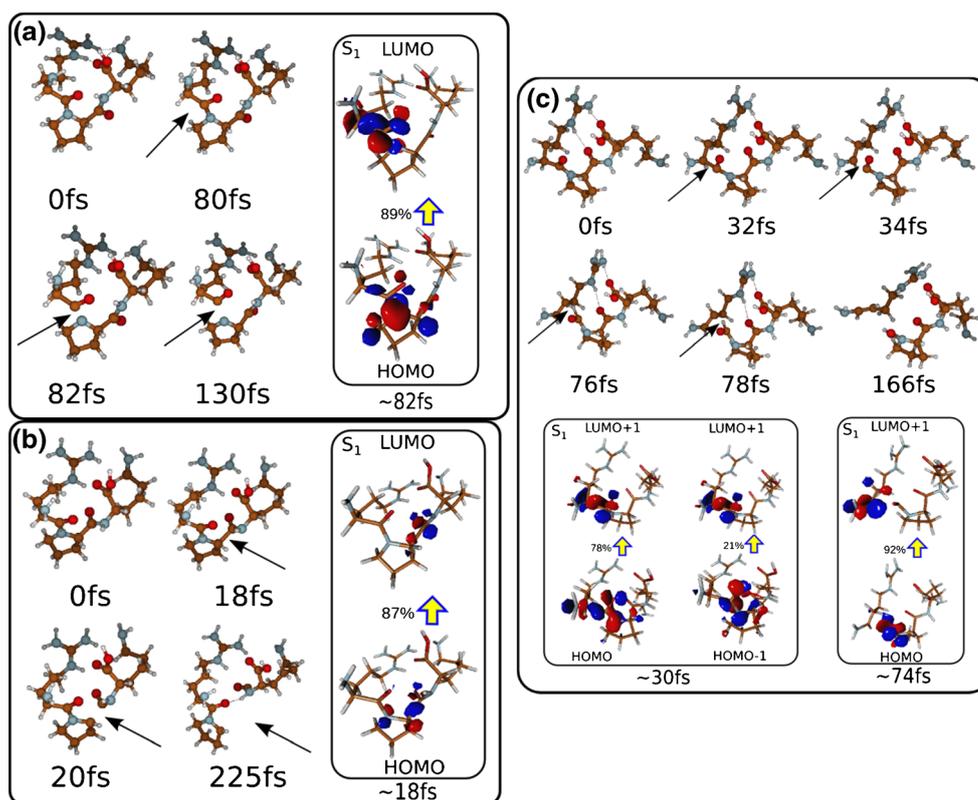

Figure 5. Snapshots of the non-adiabatic MD "on the fly" using OM2 starting in the second electronic excited state S_2 from the selected trajectory at 300 K of protonated RPK $[M + H]^+$ ion (carbon is labelled by *brown* color, nitrogen by *blue* and oxygen by *red*). Evidence of (**a**) C-N, (**b**) C-C in proline, and (**c**) C-C in Arginine bond breaking (indicated by arrows) and proton transfer in the first excited state (S_1) during the fragmentation process. Dominant excitations of molecular orbitals in the S_1 state at the time of bond breaking are also shown. (**a**) Fragmentation of C-N bond at 82 fs is characterized by excitation from non-bonding HOMO to non-bonding LUMO localized at C and N atoms, respectively. (**b**) At 18 fs, the C-C bond in proline is breaking, which is characterized by excitation from bonding HOMO to non-bonding LUMO. Trajectory (**c**) shows C-C bond breaking in Arginine at 30 fs and subsequent proton transfer at 74 fs. C-C bond breaking is characterized by excitation to two antibonding MOs

Since the experiment is performed at a temperature close to 300 K, we calculated the thermally-broadened spectrum at 300 K, shown in Figure 4b, and found that the highest density of transitions occurred around 213 nm due to S_2 and S_3 excited

(a)

(b)

(c)
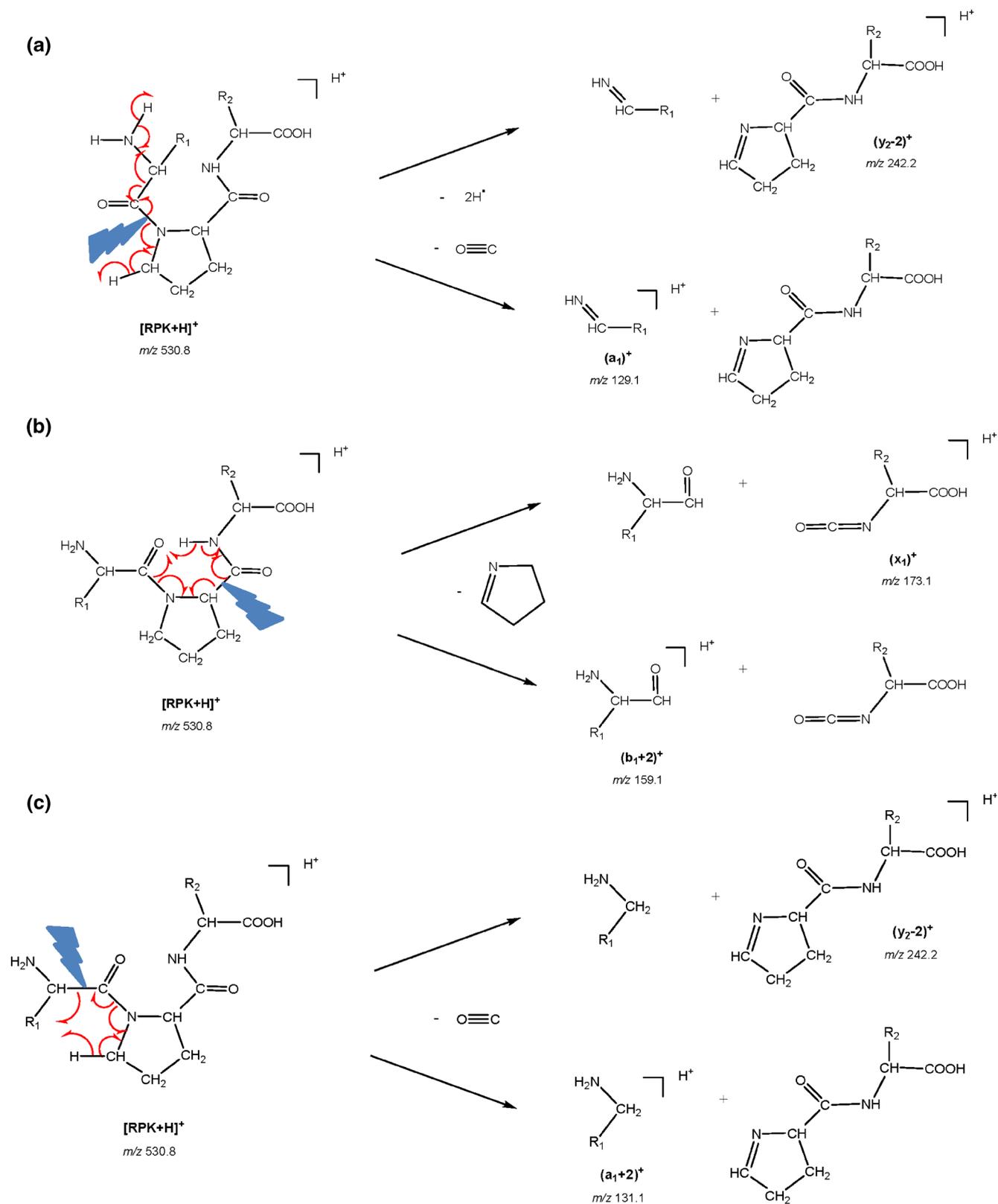
Scheme 1. Proposed mechanisms for the formation of (a) (y −2) and (a, b, x), and (b +2), and (c) (y −2) and (a +2) ions from [RPK + H] ions
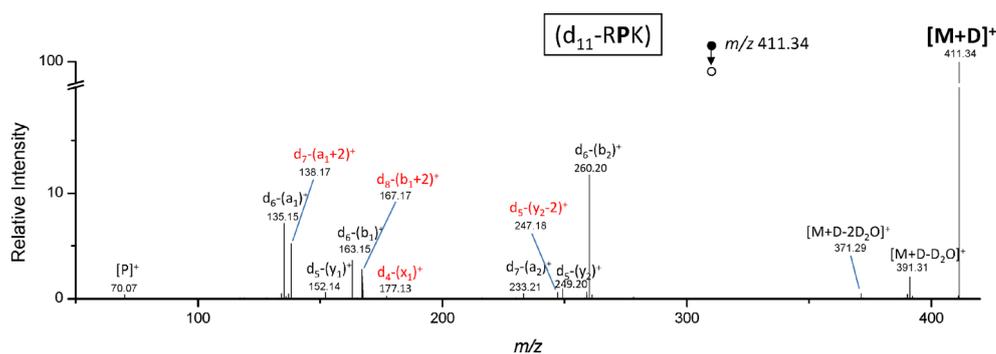
Figure 6. Photodissociation spectrum of singly-charged d_{11}-RPK [M + D]$^+$ ion (m/z 411.34) at 213 nm for 1000 ms (Collision energy 2 eV) after H/D exchange

states. Therefore, in order to follow fragmentation pathways, the non-adiabatic dynamics were studied starting from the S_2 and S_3 states. However, as they both proceed through similar pathways, the equivalent fragmentation pathways were observed. Therefore, we present results obtained starting from the S_2 state only.

### Non-adiabatic Molecular Dynamics for the Fragmentation of Protonated RPK Peptide

The non-adiabatic dynamics at 300 K starting from the second excited state S_2 lead to major fragmentation pathways which take place in the S_1 state, after non-adiabatic transitions from higher excited states, as illustrated in Figure 5. The pathways include C-N bond (Arg-Pro) breaking, and breaking of C-C bonds in the Arginine and Pro backbones. Snapshots at different times along selected trajectories illustrating bond breaking are shown in Figure 5. The dominant excitations among molecular orbitals in the S_1 state at the time of bond breaking are also presented, illustrating the nature of the fragmentation pathways. C-N bond breaking (Figure 5a, at 82 fs) is characterized by excitation from the nonbonding HOMO to the antibonding LUMO localized at N and C atoms. The breaking of the C-C bond in Pro occurs at 18 fs (Figure 5b) and is characterized by excitations from the nonbonding HOMO to the LUMO localized at the C_α atom and C atom from the carbonyl group of Pro, respectively. The trajectory showing C-C bond breaking in Arginine which is followed by proton transfer is presented in Figure 5c. After proton transfer, the Arginine fragment is unstable, and rearrangement of protons can be expected. At 30 fs, the C-C bond in Arginine breaks (see Figure 5c) and so the S_1 state for this structure is characterized by excitations from orbitals localized on the Arginine and Pro backbone to the antibonding (C-C in Arginine backbone) molecular orbital (see the bottom of Figure 5c). At ~75 fs, proton transfer as well as return to the ground state occur. The above analysis explains that different fragmentation pathways involving specific bond breaking in the S_1 state occur due to non-adiabatic transitions between different electronic excited states. To summarize, the excitations to S_2 and S_3 states result in fast non-adiabatic transitions to the S_1 state followed by activation of C-C and C-N bonds close to the Pro residues.

Fragmentation Mechanisms of the Protonated RPK Peptide

Interestingly, the above activations are the first steps in the formation of the fragment ions observed experimentally (i.e. (y-2), (a + 2) and (b + 2)). Trajectories shown in Figure 5a correspond to the homolytic cleavage of the C-N peptide bond close to Pro which is the first step in generating (y-2) type fragments. In fact, simultaneous rearrangement and elimination of CO and two H radicals, from the N-terminus and CH_2 group of the Pro ring, would yield the $(y_2-2)^+$ fragment ion at m/z 242.15 when the charge is on the lysine side chain at the time of the dissociation, as proposed in Scheme 1a. The complementary $(a_1)^+$ ion at m/z 129.11 would be produced via the same mechanism if the charge was located on the arginine (Arg) residue (Scheme 1a).

The $(b_2 + 2)^+$ fragment ion, detected at m/z 159.12, would be formed when the Arg side chain bears the charge. The mechanism involves first C-C bond activation then breaking in the Pro residue (shown in Figure 5b) and finally, proton transfer from the amine of the lysine (Lys) residue to the carbonyl group of the Arg, according to Scheme 1b. The $(\times_1)^+$ ion at m/z 173.06 is generated with the same mechanism if the charge is located on the Lys residue rather than the N-terminus.

In the same way, trajectories reported in Figure 5c lead to the C_α-C bond breaking on the N-terminal side of Pro which is a prerequisite for generating (a + 2) type fragments. Additional proton transfer from the CH_2 of the Pro ring to the alkyl group
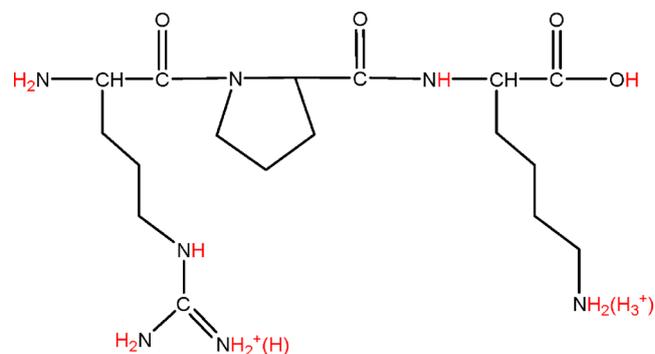
Scheme 2. Structure of [RPK + H] ions. Exchangeable hydrogens are highlighted in red

Table 3. Exact masses and assignments of fragment ions detected in the photodissociation spectrum of singly-charged deuterated RPK [M + D]$^+$ (Figure 6). Error=(m/z theoretical – m/z experimental)/(m/z theoretical)

Assignment	Elemental composition	Theoretical m/z	Experimental m/z	Error (ppm)
[M + D]$^+$	$C_{17}H_{23}D_{11}O_4N_7$	411.3357	411.3356	−0.244
[M + D-D$_2$O]$^+$	$C_{17}H_{23}D_9O_3N_7$	391.3126	391.3123	−0.769
[M + D-2D$_2$O]$^+$	$C_{17}H_{23}D_7O_2N_7$	371.2895	371.2892	−0.810
d$_6$-(b$_2$)$^+$	$C_{11}H_{14}D_6O_2N_5$	260.1988	260.1986	−0.769
d$_5$-(y$_2$)$^+$	$C_{11}H_{17}D_5O_3N_3$	249.1969	249.1965	−1.612
d$_5$-(y$_2$-2)$^+$	$C_{11}H_{15}D_5O_3N_3$	247.1813	247.1812	−0.406
d$_7$-(a$_2$)$^+$	$C_{10}H_{13}D_7ON_5$	233.2102	233.2098	−1.723
d$_4$-($\times_1$)$^+$	$C_6H_9D_4O_2N_4$	177.1284	177.1287	1.703
d$_8$-(b$_1$ + 2)$^+$	$C_6H_7D_8ON_4$	167.1743	167.1741	−1.204
d$_6$-(b$_1$)$^+$	$C_6H_7D_6ON_4$	163.146	163.1458	−1.226
d$_5$-(y$_1$)$^+$	$C_6H_{10}D_5O_2N_2$	152.1442	152.1439	−1.985
d$_7$-(a$_1$ + 2)$^+$	$C_5H_8D_7N_4$	138.1731	138.1729	−1.447
d$_6$-(a$_1$)$^+$	$C_5H_7D_6N_4$	135.1511	135.1509	−1.491
[P]$^+$	C_4H_8N	70.0651	70.0652	1.427

of the Arg and elimination of a CO molecule (presented in Scheme 1c) would produce the (a$_1$ + 2)$^+$ ion detected at m/z 131.13 when the Arg side chain bears the charge. This fragmentation pathway would also lead to the (y$_2$-2)$^+$ fragment ion if the charge is located on the Lys residue at the time of the dissociation.

Since the above mechanisms involve exchangeable hydrogen atoms, they could be tested by performing H/D exchange experiments. The UVPD-MS/MS spectrum of the singly-charged RPK peptide detected at m/z 411.34 after ESI of the CH$_3$OD/D$_2$O 50:50 (%v/v) solution of the RPK peptide is shown in Figure 6. In this case, all 11 mobile hydrogens have been exchanged, as highlighted in red in Scheme 2. The single charge is located either on=NH$_2$$^+$ of the Arg or on the NH$_3$$^+$ of the Lys residue (Scheme 2). The singly-charged d$_{11}$-RPK precursor ion was then detected with an 11 Da mass increase. Similarly, a, b and y ions as well as deuterium oxide losses (see assignments in Table 3) are observed in the photodissociation from this precursor. The photodissociation at 213 nm of the singly-charged d$_{11}$-RPK also shows (Figure 6) the unusual d$_5$-(y$_2$-2)$^+$, d$_4$-($\times_1$)$^+$, d$_8$-(b$_1$ + 2)$^+$ and d$_7$-(a$_1$ + 2)$^+$ ions detected at m/z 247.18, m/z 177.12, m/z 167.17 and m/z 138.17, respectively (exact masses in Table 3). Comparison of fragmentation patterns in Figures 3a and 6 confirms the proposed mechanism. First, fragment (y$_2$-2)$^+$ presents a 5 Da mass increase in agreement with structures proposed in Scheme 1a and c i.e. one deuterium on the Lys amine, three deuterium on the Lys side chain bearing the charge, and one deuterium on the C-terminus group. Moreover, the (a$_1$)$^+$ fragment is detected with a 6 Da mass increase (Figure 6) after H/D exchange as expected from the structure in Scheme 1a i.e. five deuterium on the Arg side chain bearing the charge and one on the N-terminus. In fact, the precursor ion has eliminated a deuterium from the initial ND$_2$ terminus group which confirms the mechanism in Scheme 1a. In addition, according to the mechanism proposed in Scheme 1b, ($\times_1$)$^+$ should have three deuterium on the Lys side chain bearing the charge and one at the C-terminus group, i.e. a 4 Da mass increase, which is observed (Figure 6). Again following Scheme 1b, fragment (b$_1$ + 2)$^+$ should contain five deuterium on the Arg side chain bearing the charge, two at the

N-terminus group and one on the Arg carbonyl group where it has been transferred from the Lys amine group, i.e. an 8 Da mass increase, which is also observed on the fragmentation pattern (Figure 6). Therefore, up to this point, all examined fragmentation pathways are in agreement with the mechanisms previously proposed by Kim *et al.* [36].

Finally, the (a$_1$ + 2)$^+$ fragment is detected with a 7 Da mass increase (Figure 6) which is inconsistent with a proton transfer from the Lys amine as proposed by Kim *et al.* [36] which would have led to an 8 Da mass increase. Alternatively, a proton transfer from a CH$_2$ group of the Pro ring, as proposed in Scheme 1c, would explain the observed 7 Da mass increase, i.e. five deuterium on the Arg side chain bearing the charge and two deuterium at the N-terminal. Moreover, we can note that the relative intensity between the (a$_1$-2)$^+$ and (a$_1$)$^+$ ions is the same (73%) before and after H/D exchange (Figures 3a and 6). This confirms the proposed mechanism where D transfer is not required. In fact, hydrogen migration is favored over deuterium transfer.

Conclusions

To conclude, we observed the formation of unusual (y-2), (a + 2) and (b + 2) fragment ions upon photodissociation of proline-containing peptides at 213 nm. The formation of these ions was not observed at 266 nm, or for non-proline-containing peptides. The RPK peptide was the smallest peptide for which we were able to observe these fragmentation pathways experimentally. Calculation of the electronic excited states for this peptide showed that S$_2$ and S$_3$ states could be excited at the experimental wavelength. Non-adiabatic molecular dynamic simulation (MD) starting from S$_2$ and S$_3$ excited states showed that this excitation was followed by C-C and C-N bond activation close to the proline residue. The MD revealed early relaxation mechanisms leading to the observed fragmentation pathways.

Our complementary theoretical and experimental investigations open new routes for identification of photofragmentation

pathways. They enable the identification of the link between the nature of electronically-excited states and the observed fragmentation pathways. The MD simulations on the fly provide the foundation for a molecular understanding of the photochemistry of peptides under UV excitation. These trajectories revealed specific breaking of C-C and C-N bonds close to the proline residue. Consecutive rearrangements and proton transfers are required to produce the above unusual fragment ions and the fragmentation mechanisms were confirmed by H/D exchange experiments.

Acknowledgments

References

1. Paizs, B., Suhai, S.: Fragmentation pathways of protonated peptides. Mass Spectrom. Rev. 24(4), 508–548 (2005)
2. Smith, R.D., Loo, J.A., Loo, R.R.O., Busman, M., Udseth, H.R.: Principles and Practice of Electrospray Ionization - Mass-Spectrometry for Large Polypeptides and Proteins. Mass Spectrom. Rev. 10(5), 359–451 (1991)
3. Cox, K.A., Gaskell, S.J., Morris, M., Whiting, A.: Role of the site of protonation in the low-energy decompositions of gas-phase peptide ions. J. Am. Soc. Mass Spectrom. 7(6), 522–531 (1996)
4. Dongre, A.R., Jones, J.L., Somogyi, A., Wysocki, V.H.: Influence of peptide composition, gas-phase basicity, and chemical modification on fragmentation efficiency: Evidence for the mobile proton model. J. Am. Chem. Soc. 118(35), 8365–8374 (1996)
5. Dongre, A.R., Somogyi, A., Wysocki, V.H.: Surface-induced dissociation: An effective tool to probe structure, energetics and fragmentation mechanisms of protonated peptides. J. Mass Spectrom. 31(4), 339–350 (1996)
6. Jones, J.L., Dongre, A.R., Somogyi, A., Wysocki, V.H.: Sequence Dependence of Peptide Fragmentation Efficiency Curves Determined by Electrospray-Ionization Surface-Induced Dissociation Mass-Spectrometry. J. Am. Chem. Soc. 116(18), 8368–8369 (1994)
7. Summerfield, S.G., Bolgar, M.S., Gaskell, S.J.: Promotion and stabilization of b(1) ions in peptide phenylthiocarbamoyl derivatives: Analogies with condensed-phase chemistry. J. Mass Spectrom. 32(2), 225–231 (1997)
8. Summerfield, S.G., Whiting, A., Gaskell, S.J.: Intra-ionic interactions in electrosprayed peptide ions. Int. J. Mass Spectrom. Ion Process 162(1–3), 149–161 (1997)
9. Hunt, D.F., Yates, J.R., Shabanowitz, J., Winston, S., Hauer, C.R.: Protein Sequencing by Tandem Mass-Spectrometry. Proc. Natl. Acad. Sci. U. S. A. 83(17), 6233–6237 (1986)
10. Johnson, R.S., Martin, S.A., Biemann, K.: Collision-Induced Fragmentation of (M + H) + Ions of Peptides - Side-Chain Specific Sequence Ions. Int. J. Mass Spectrom. Ion. Process. 86, 137–154 (1988)
11. Tabb, D.L., Smith, L.L., Breci, L.A., Wysocki, V.H., Lin, D., Yates, J.R.: Statistical characterization of ion trap tandem mass spectra from doubly charged tryptic peptides. Anal. Chem. 75(5), 1155–1163 (2003)
12. Reid, G.E., Wu, J., Chrisman, P.A., Wells, J.M., McLuckey, S.A.: Charge-state-dependent sequence analysis of protonated ubiquitin ions via ion trap tandem mass spectrometry. Anal. Chem. 73(14), 3274–3281 (2001)
13. Counterman, A.E., Clemmer, D.E.: Cis-trans signatures of proline-containing tryptic peptides in the gas phase. Anal. Chem. 74(9), 1946–1951 (2002)

14. Harrison, A.G., Young, A.B...: Fragmentation reactions of deprotonated peptides containing proline. The proline effect. J. Mass Spectrom. 40(9), 1173–1186 (2005)
15. Hayakawa, S., Hashimoto, M., Matsubara, H., Turecek, F.: Dissecting the proline effect: Dissociations of proline radicals formed by electron transfer to protonated pro-gly and gly-pro dipeptides in the gas phase. J. Am. Chem. Soc. 129(25), 7936–7949 (2007)
16. Ramek, M., Kelterer, A.M., Teppen, B.J., Schafer, L.: Theoretical Structure Investigations of N-Acetyl-L-Proline Amide. J. Mol. Struct. 352, 59–70 (1995)
17. Vaisar, T., Urban, J.: Probing the proline effect in CID of protonated peptides. J. Mass Spectrom. 31(10), 1185–1187 (1996)
18. Vanhoof, G., Goossens, F., Demeester, I., Hendriks, D., Scharpe, S.: Proline Motifs in Peptides and Their Biological Processing. FASEB J. 9(9), 736–744 (1995)
19. Loo, J.A., Edmonds, C.G., Smith, R.D.: Tandem Mass-Spectrometry of Very Large Molecules .2. Dissociation of Multiply Charged Proline-Containing Proteins from Electrospray Ionization. Anal. Chem. 65(4), 425–438 (1993)
20. Schwartz, B.L., Bursey, M.M.: Some Proline Substituent Effects in the Tandem Mass-Spectrum of Protonated Pentaalanine. Biol. Mass Spectrom. 21(2), 92–96 (1992)
21. Breci, L.A., Tabb, D.L., Yates, J.R., Wysocki, V.H.: Cleavage N-terminal to proline: Analysis of a database of peptide tandem mass spectra. Anal. Chem. 75(9), 1963–1971 (2003)
22. Madsen, J.A., Gardner, M.W., Smith, S.I., Ledvina, A.R., Coon, J.J., Schwartz, J.C., Stafford Jr., G.C., Brodbelt, J.S.: Top-Down Protein Fragmentation by Infrared Multiphoton Dissociation in a Dual Pressure Linear Ion Trap. Anal. Chem. 81(21), 8677–8686 (2009)
23. Zubarev, R.A.: Reactions of polypeptide ions with electrons in the gas phase. Mass Spectrom. Rev. 22(1), 57–77 (2003)
24. Zubarev, R.A., Kelleher, N.L., McLafferty, F.W.: Electron capture dissociation of multiply charged protein cations. A nonergodic process. J. Am. Chem. Soc. 120(13), 3265–3266 (1998)
25. Coon, J.J., Shabanowitz, J., Hunt, D.F., Syka, J.E.P.: Electron transfer dissociation of peptide anions. J. Am. Soc. Mass Spectrom. 16(6), 880–882 (2005)
26. Mikesh, L.M., Ueberheide, B., Chi, A., Coon, J.J., Syka, J.E.P., Shabanowitz, J., Hunt, D.F.: The utility of ETD mass spectrometry in proteomic analysis. Biochim. Biophys. Acta 1764(12), 1811–1822 (2006)
27. Syka, J.E.P., Coon, J.J., Schroeder, M.J., Shabanowitz, J., Hunt, D.F.: Peptide and protein sequence analysis by electron transfer dissociation mass spectrometry. Proc. Natl. Acad. Sci. U. S. A. 101(26), 9528–9533 (2004)
28. Antoine, R., Joly, L., Tabarin, T., Broyer, M., Dugourd, P., Lemoine, J.: Photo-induced formation of radical anion peptides. Electron photodetachment dissociation experiments. Rapid Commun. Mass Spectrom. 21(2), 265–268 (2007)
29. Anusiewicz, I., Jasionowski, M., Skurski, P., Simons, J.: Backbone and side-chain cleavages in electron detachment dissociation (EDD). J. Phys. Chem. A 109(49), 11332–11337 (2005)
30. Kjeldsen, F., Silivra, O.A., Ivonin, I.A., Haselmann, K.F., Gorshkov, M., Zubarev, R.A.: C-alpha-C backbone fragmentation dominates in electron detachment dissociation of gas-phase polypeptide polyanions. Chem. Eur. J. 11(6), 1803–1812 (2005)
31. Larraillet, V., Antoine, R., Dugourd, P., Lemoine, J.: Activated-Electron Photodetachment Dissociation for the Structural Characterization of Protein Polyanions. Anal. Chem. 81(20), 8410–8416 (2009)
32. Larraillet, V., Vorobyev, A., Brunet, C., Lemoine, J., Tsybin, Y.O., Antoine, R., Dugourd, P.: Comparative Dissociation of Peptide Polyanions by Electron Impact and Photo-Induced Electron Detachment. J. Am. Soc. Mass Spectrom. 21(4), 670–680 (2010)
33. Cook, S.L., Collin, O.L., Jackson, G.P.: Metastable atom-activated dissociation mass spectrometry: leucine/isoleucine differentiation and ring cleavage of proline residues. J. Mass Spectrom. 44(8), 1211–1223 (2009)
34. Cooper, H.J., Hudgins, R.R., Hakansson, K., Marshall, A.G.: Secondary fragmentation of linear peptides in electron capture dissociation. Int. J. Mass Spectrom. 228(2–3), 723–728 (2003)
35. Reilly, J.P.: Ultraviolet Photofragmentation of Biomolecular Ions. Mass Spectrom. Rev. 28(3), 425–447 (2009)

36. Kim, T.-Y., Valentine, S.J., Clemmer, D.E., Reilly, J.P.: Gas-Phase Conformation-Specific Photofragmentation of Proline-Containing Peptide Ions. J. Am. Soc. Mass Spectrom. **21**(8), 1455–1465 (2010)

37. Madsen, J.A., Boutz, D.R., Brodbelt, J.S.: Ultrafast Ultraviolet Photodissociation at 193 nm and its Applicability to Proteomic Workflows. J. Proteome Res. **9**(8), 4205–4214 (2010)

38. Dewar, M.J.S., Zoebisch, E.G., Healy, E.F., Stewart, J.J.P.: The Development and Use of Quantum-Mechanical Molecular-Models .76. Am1 - a New General-Purpose Quantum-Mechanical Molecular-Model. J. Am. Chem. Soc. **107**(13), 3902–3909 (1985)

39. Weber, W., Thiel, W.: Orthogonalization corrections for semiempirical methods. Theor. Chem Acc. **103**(6), 495–506 (2000)

40. Patchkovskii, S., Koslowski, A., Thiel, W.: Generic implementation of semi-analytical CI gradients for NDDO-type methods. Theor. Chem Acc. **114**(1–3), 84–89 (2005)

41. Koslowski, A., Beck, M.E., Thiel, W.: Implementation of a general multireference configuration interaction procedure with analytic gradients in a semiempirical context using the graphical unitary group approach. J. Comput. Chem. **24**(6), 714–726 (2003)

42. Thiel, W. *MNDO program.*, Max-Planck-Institut für Kohlenforschung: Muhlheim, Germany: 2007

43. Tully, J.C.: Molecular-Dynamics with Electronic-Transitions. J. Chem. Phys. **93**(2), 1061–1071 (1990)

44. Verlet, L.: Computer Experiments on Classical Fluids .I. Thermodynamical Properties of Lennard-Jones Molecules. Phys. Rev. **159**(1), 98 (1967)

CURRICULUM VITAE

ŽELJKA SANADER

Date of birth:	19.03.1988.
Place of birth:	Split, Croatia
Nationality:	Croatian

EMPLOYMENT

- **2013- present** Teaching assistant, Faculty of Science, University of Split

- **2011-2013.** Junior researcher, Interdisciplinary Center for Advanced Science and Technology, University of Split

EDUCATION

- **2011-2016.** Doctoral program in Biophysics, Faculty of Science, University of Split

- **2009-2011.** Magister of physics, Faculty of Science, University of Split

- **2006-2009.** Bachelor of mathematics and physics, Faculty of Science, University of Split

Publication list

ŽELJKA SANADER

1. I. Russier-Antoine, F. Bertorelle, Ž. Sanader, M. Krstić, C. Comby-Zerbino, Ph. Dugourd, P. F. Brevet, V.Bonačić-Koutecký, R. Antoine, "Ligand-Core NLO-phores: a combined experimental and theoretical approach of the two-photon absorption and two-photon excited emission properties of small ligated silver nanoclusters", *Nanoscale*, **2016**, Submitted

2. Ž. Sanader, M. Krstić, I. Russier-Antoine, F. Bertorelle, Ph. Dugourd, P. F. Brevet, R. Antoine, V. Bonačić-Koutecký, "Two-photon absorption of ligand-protected Ag_{15} nanoclusters. Towards a new class of nonlinear optics nanomaterials", *Physical Chemistry Chemical Physics*, **2016**, 18, 12404

3. I. Russier-Antoine, F. Bertorelle, R. Hamouda, D. Rayane, Ph. Dugourd, Ž. Sanader, V. Bonačić-Koutecký, P.F. Brevet, R. Antoine, "Tuning Ag_{29} nanocluster light emission from red to blue with one and two-photon excitation" , *Nanoscale*, **2016**, 8, 2892

4. M. Girod, Ž. Sanader, M. Vojković, R. Antoine, L. MacAleese, J. Lemoine, V. Bonačić-Koutecký, Ph. Dugourd, "UV Photo-dissociation of proline-containing peptide ions: Insights from molecular dynamics", *J Am Soc Mass Spectrom.*, **2015**, 26, 432

5. Ž. Sanader, R. Mitrić, V. Bonačić-Koutecký, B. Bellina, R. Antoine, Ph. Dugourd, "The nature of electronic excitations at the metal–bioorganic interface illustrated on histidine–silver hybrids", *Phys. Chem. Chem. Phys.*, **2014**, 16, 1257

6. B. Bellina, R. Antoine, M. Broyer, L. Gell, Ž. Sanader, R. Mitrić, V. Bonačić-Koutecký, Ph. Dugourd, "Formation and characterization of thioglycolic acid-silver cluster complexes", *Dalton Trans.*, **2013**, 42, 8328

7. Ž. Sanader, C. Brunet, M. Broyer, R. Antoine, Ph. Dugourd, R. Mitric, V. Bonačić-Koutecký, "Cation induced electrochromism in 2,4-dinitrophenylhydrazine (DNPH): Tuning optical properties of aromatic rings", *Chemical Physics Letters*, **2013**, 570, 22